NTNU – Trondheim
Norwegian University of
Science and Technology

Finite Element Modeling and Structural State Estimation of a Bottom Fixed Offshore Wind Turbine

Henrik Sogn Paust

Marine Technology
Submission date: July 2015
Supervisor: Asgeir Johan Sørensen, IMT

Norwegian University of Science and Technology
Department of Marine Technology

NTNU – Trondheim
Norwegian University of
Science and Technology

Finite Element Modeling and Structural State Estimation of a Bottom Fixed Offshore Wind Turbine

Henrik Paust

June 2015

MASTER THESIS
Department of Marine Technology
Norwegian University of Science and Technology

Supervisor: Professor - Asgeir J. Sørensen, IMT
Co-supervisor: 1. Amanuensis II - Anne Marthine Rustad, IMT

NTNU Trondheim
Norwegian University of Science and Technology
Department of Marine Technology

MASTER THESIS IN MARINE CYBERNETICS

SPRING 2015

Name of the candidate:	Henrik Paust.
Field of study:	Marine control engineering.
Thesis title (English):	Finite element modeling and structural state estimation of a bottom fixed offshore wind turbine.
Thesis title (Norwegian):	Elementmodellering og strukturell tilstandsestimering av en bunnfast offshore vind turbin.

Background:
In the path to meet the world's growing energy demand, and fight the climate changes due to large emissions of greenhouse gases, new and greener energy alternatives are necessary. One of the proposed solutions to meet these goals is through increased use of wind turbines. Deploying wind farms offshore comes with opportunities of greater and more reliable energy capture, as the wind blows more steadily offshore, and are generally stronger in the afternoon when electricity demand is high. However, because of the remote nature of offshore wind farms, the corresponding cost of operations and maintenance are today high, and constitute about 25% of the total kWh costs over the entire life of a turbine. To decrease the costs for offshore wind turbines, prognosis and health-monitoring systems will become much more necessary. This will enable better maintenance monitoring and planning, as well a deeper understanding of the turbine behavior. Monitoring of structural response can also be of great aid in designing better offshore wind turbine structures, and eventually more sophisticated wind turbine control systems incorporating the structural response.

Work Description:
This thesis will design a low fidelity element model of the 10 MW DTU reference turbine on a monopile substructure. The model will be used for investigating possibilities for implementing real time estimation of the structural response.

Scope of work
- Investigate methods to design a finite element model for an offshore wind turbine.
- Generate a low fidelity finite element (FEM) model of the wind turbine structure in Matlab.
- Implement different realistic loading scenarios for the modeled structure.
- Design two structural state estimators on the modeled wind turbine model.
- Simulate the structural response and compare the performance of the state estimators when subjected to the modeled loading scenarios.
- Document each step in the process.

NTNU Trondheim
Norwegian University of Science and Technology
Department of Marine Technology

The thesis shall be submitted with two printed and electronic copies, to 1) the main supervisor and 2) the external examiner, each copy signed by the candidate. The final revised version of this thesis description must be included. The report must appear in a bound volume or a binder according to the NTNU standard template. Computer code and a PDF version of the report shall be included electronically.

Start date: January 14, 2015 **Due date:** July 28, 2015

Supervisor: Professor Asgeir J. Sørensen
Asgeir.sorensen@ntnu.no
+47 918 97 457

Co-supervisor: Anne Marthine Rustad
Anne.marthine.rustad@akersolutions.com

Acknowledgment

This thesis was written at the department of marine technology, NTNU during the spring of 2015.
I would like to thank Post doc. Lene Eliassen for providing me with necessary data for the modeled structure, and for always having an open door to discuss any questions I might had. I would also like to thank Emil Smilden for our conversations on the process of the work and problems we both encountered.

Last but not least I would like to thank my supervisor Professor Asgeir J. Sørensen and co. supervisor Anne Marthine Rustad. You guys have been both motivational and helpful in times of adversity and in discussing how to outline the thesis.

To my office mates at C.1072, thank you for all the good times we spent together during our final year. With out you, this thesis would have been done much sooner.

Henrik Paust
Trondheim, July 2015

Abstract

As a path to combine the world's growing energy demand with renewable green energy, increased use of offshore wind turbines has been seen as a viable solution. Unfortunately, the remote location and rough environment for offshore wind turbines lead to limited availability and high maintenance costs. Increased use of turbine health monitoring will enable better understanding of the turbine behavior, opening up to perform more intelligent maintenance planning and thus reducing maintenance costs. This thesis has designed a simplified element model together with two structural state estimators, such that better monitoring of wind turbine structures can be made possible.

The work has been performed in two parts. The first part considered the design of a simplified finite element model of the turbine structure, including the monopile, transition piece and tower section. The turbine structure model parameters have been based on the 10MW DTU reference turbine. The soil-structure interaction was included through $p-y$ curves and Winkler foundation theory. To test the turbine behavior and response, environmental loadings was accounted for by applying an equivalent wind thrust force on the tower top using wind turbine momentum theory. Wave interaction was modeled by first order wave loads using potential theory and Morison's equation. Other loading effects from tower-rotor interaction and water current was also considered.

The second part of the work involved the design of two structural state estimators with the goal to estimate unknown nodal values of the designed finite element model. The first estimator was designed as a dual input-state estimator. The $input\text{-}state$ estimator used an unbiased force estimate of the unknown applied environmental forces together with a Kalman-like filter to obtain excellent results of the nodal value estimates. The second estimator design was a $bias$-based estimator using a Kalman filter together with a first order Markov parameter model added to the observer model. The $bias$ term acted as an integrator, which removed any steady state error in the estimates. The $bias$-based estimator showed that in its simplicity it was able to estimate nodal displacements in a good manner, although with some limitations on estimates on nodes located far away from nearest measured value. Simulations showed that the $input\text{-}state$ estimator outperformed the $bias$-based estimator in displacement and bending moment estimates. For velocity estimates, the $bias$-based estimate showed better behavior. Overall both estimators showed satisfactory results. The findings of this thesis suggest that a structural state estimator can be combined with a finite element model of an offshore wind turbine to perform real-time monitoring on the response and eventually fatigue damage estimation. By having an estimator model of the structural response of the turbine, it is possible to perform smarter and better decisions on maintenance work as well as obtaining better knowledge on the true response picture of an offshore wind turbine.

Sammendrag

I et ledd for å kombinere verdens økende energietterspørsel med fornybar energi, har økende bruk av offshore vindkraft blitt sett på som en mulig løsning. Uheldigvis gjør den strategiske plasseringen av offshore vindparker og de harde påkjenningene fra vær og vind redusert tilgjengelighet samt høye vedlikeholdskostnader. Økt bruk av tilstandsestimering av turbinen vil gi bedre forståelse over påkjenninger og respons, hvilket kan åpne opp for mer intelligent vedlikeholdsplanlegging og dermed redusere vedlikeholdskostnader. Denne oppgaven har designet en forenklet element modell sammen med to strukturelle tilstandsestimatorer, slik at bedre monitorering av strukturen muliggjøres.

Arbeidet er blitt utført i to deler. Den første delen tok for seg designet av en forenklet elementmodell av turbinstrukturen, bestående av monopile, overgangsdel og tårnseksjon. Turbinmodellen er basert på 10 MW DTU referanse turbinen designet ved Danmarks Tekniske Universitet. Jord-struktur interaksjon er modellert gjennom $p-y$ kurver og Winkler teori. For å teste turbinens oppførsel og respons, er laster fra bølger og vind modellert. Påkjenninger fra vind ble modellert gjennom vindturbin momentum teori og påsatt som en ekvivalent last ved tårntoppen. Bølgeinteraksjon ble modellert som 1.ordens bølger med potensialteori og bølgelastene gjennom Morisons ligning. Andre last effekter fra tårn-rotor interaksjon og strøm i vannet ble også betraktet.

Den andre delen av arbeidet involverte design av to strukturelle tilstandsestimatorer med mål om å estimere ukjente nodeverdier på den designede elementmodellen. Den første estimatoren ble designet som en dual $input-tilstands$ estimator. $input-tilstands$ estimatoren brukte et objektivt kraftestimat av de ukjente miljølastene sammen med et Kalman lignende filter til å oppnå gode estimater for nodeverdier i modellen. Den andre estimatoren ble designet som en $bias$-estimator, hvor en 1. ordens Markov parameter modell ble lagt til estimatormodellen i kombinasjon med et Kalman filter. Bias leddet fungerte som en integrator, hvilket fjernet stasjonær avvik i estimatene. $bias$-estimatoren viste i sin enkelthet gode resultater, men med noe redusert nøyaktighet for noder plassert langt unna målte verdier. Simuleringer viste at $input-tilstands$ estimatoren ga bedre resultater enn $bias$-estimatoren i forskyvning og bøyemoment estimater. For hastighetsestimater ble det vist at $bias$-estimatoren ga bedre resultater. Totalt sett viste begge estimatorene tilfredsstillende resultater. Resultatet av dette arbeidet konkluderer med at strukturelle tilstandsestimatorer kan kombineres med en element metode modell for en offshore vindturbin til å oppnå sanntidsmonitorering av respons og eventuelt utmattelsesestimering. Ved å ha en estimatormodell for den strukturelle responsen av turbinen er det mulig å oppnå smartere og bedre beslutninger angående vedlikeholdsarbeid samt få bedre oversikt over det sanne responsbildet til en offshore vindturbin.

Nomenclature

Table 1: Constants and definitions

Constants	Definition
D_b	Diameter of turbine blades [m]
$\bar{U}$	Mean wind speed [m/s]
C_T	Thrust coefficient [-]
C_{da}	Drag coefficient in air [-]
C_{dw}	Drag coefficient in water [-]
ρ_a	Density of air [kg/m^3]
ρ_s	Density of steel [kg/m^3]
ρ_w	Density of water [kg/m^3]
$\tau_{\bar{U}}$	Static wind load [N]
τ_a	Axial loading [N]
σ	Standard deviation in fluctuating wind speed [-]
l	Lengthscale in Kaimal Spectrum [m]
H_{m0}	Significant wave height [m]
Tp	Peak period [s]
Δt	Discrete time step [s]
T	Total simulation time [s]
R_b	Blade radius [m]
V_c	Current velocity [m/s]
N	Number of samples in a realization [-]
ϕ	Random phase angle [rad]
δ_1	Inertia matrix offset factor [-]
δ_2	Stiffness matrix offset factor [-]
δ_3	Damping matrix offset factor[-]
α	Mass damping coefficient [-]
β	Stiffness damping coefficient [-]
μ	Wind speed scaling factor [-]
M_{top}	Total top mass, nacelle, blades etc. [kg]
h	Water depth [m]
ξ_{soil}	Soil damping ratio [-]
ξ_{str}	Structural damping ratio [-]
$\mathbf{d}_b^e$	Nodal displacements bar element [m]
$\mathbf{d}^e$	Nodal displacements beam element [m]
$\mathbf{N}_{bar}^e(\xi)$	Shape functions for bar element [-]
$\mathbf{N}_{bm}^e(\xi)$	Shape function for beam element [-]
$\mathbf{M}_{bar}^e$	Inertia matrix bar element
$\mathbf{K}_{bar}^e$	Stiffness matrix bar element
$\mathbf{K}_{bm}^e$	Stiffness matrix beam element
$\mathbf{K}_{\sigma}^e$	Geometric stiffness matrix

Continued on next page

Table 1 – Continued from previous page

Constants	Definition
$\mathbf{K}^e_{soil}$	Soil stiffness matrix
$\mathbf{M}^e_{bm}$	Inertia matrix beam element
$\mathbf{M}^e_a$	Elemental added mass matrix
$\mathbf{M^e}_T$	Total model inertia matrix
$\mathbf{K^e}_T$	Total model stiffness matrix
$\mathbf{D_d}$	Total model damping matrix
$\mathbf{A}$	Plant system model
$\mathbf{G}$	Disturbance input gain matrix
Ω	Eigenvector matrix
Λ	Modal damping matrix
Φ	State transition matrix
Γ	Input matrix
$\bar{\mathbf{G}}$	Observer disturbance gain matrix
$\mathbf{C}$	Output matrix
n_p	Number of input forces
n_y	Number of measurements
n_m	Number of modes in reduced order model
Δt	Simulation time increment
$\bar{\mathbf{M}}$	Estimator inertia matrix
$\bar{\mathbf{K}}$	Estimator stiffness matrix
$\bar{\mathbf{D}}_\mathbf{b}$	Estimator damping matrix
$\mathbf{V}$	Eigenvectors of system model
$\hat{\mathbf{V}}$	Mass normalized eigenvectors

Table 2: Variables and definitions

Variables	Definition
ω_w	Frequency of fluctuating wind component [rad/s]
ω_r	Rotational frequency of turbine rotor [rad/s]
ω	Frequency of wave component [rad/s]
$S(\omega_w)_{kk}$	Kaimal Spectrum
$H_H(\omega)$	Hydrodynamic transfer function
$H_W(\omega_w)$	Turbulent wind load transfer function
$D_t(z)$	Diameter of structure [m]
$u(t)$	fluctuating windspeed [m/s]
$U(t)$	Total wind speed [m/s]
ξ	Natural coordinate
$a(x)$	Elemental axial displacement [m]
$v(x)$	Elemental transversal displacement [m]

Continued on next page

Table 2 – Continued from previous page

Variables	Definition
$M_b^e(x)$	Elemental bending moment [Nm]
$\sigma^e(x)$	Elemental stress [Pa]
τ_{gust}	Dynamic wind load [N]
τ_{waves}	Wave loads [N]
τ_{3P}	3P loading [N]
ξ_A	Wave amplitude [m]
$\mathbf{q}$	State vector
$\mathbf{u}$	Modal state vector

Acronyms	Definition
LCOE	Levelized cost of electricity
O&M	Operations and Maintenance
OWT	Offshore wind turbine
FE	Finite element
BEM	Blade element momentum
DOF	Degree of freedoms

Table 3: Acronyms

Contents

Chapter 1

Introduction

In this chapter a motivation for the work behind the thesis is presented. Previous work on similar topics and contributions to the field is pointed out. Section 1.4 outlines the organization of the thesis.

1.1 Motivation

In a path to meet the world's growing energy demand, and fight the climate changes due to large emissions of greenhouse gases, new and greener energy alternatives are necessary. One of the proposed solutions to meet these goals is through increased use of wind turbines. There are today many wind farms located around the world, where most of them are located onshore. Today much research is driven towards increasing the amount of offshore wind farms. Deploying wind farms offshore comes with opportunities of greater and more reliable energy capture, as the wind blows more steadily offshore, and are generally stronger in the afternoon when electricity demand is high. However, because of the remote nature of offshore wind farms, the corresponding cost of Operations and Maintenance (O&M) are today high, and constitute about 25% of the total kWh costs over the entire life of a turbine (Hassan, 2013).
Offshore wind energy is today the most expensive form of energy capture which is commercially focused on, with almost twice the levelized cost of electricity (LCOE) compared to onshore wind (Kost and Mayer, 2013).

Fatigue damage prevention is one of the main design drivers for offshore wind turbines (OWTs). Fatigue damage estimation in wind turbine design is inflicted with high degree of uncertainty, as an OWT is subjected to a large number of different loading scenarios. Studies done by Versteijlen et al. (2014) and Versteijlen et al. (2011) addressed the problem on deviation between estimated and measured natural frequencies for OWT's. They showed that the complex connection between soil and structure makes it very difficult to estimate the correct natural frequencies of structure, as soil-structure interaction in terms of added stiffness and damping is not sufficiently understood. In addition to the varying loading scenarios and complex soil-structure interaction, marine growth, scour development, icing and corrosion can with time significantly alter the behavior of the turbine, which can be difficult to predict.

The uncertainty in loading scenarios and discrepancies in modeled and measured natural frequencies leads to safety factors when designing the structure. The use of safety factors often lead to overly conservative designs or underestimation of the structure's operational lifetime.

To decrease the costs for OWTs, prognosis and health-monitoring systems will become much more necessary. This will enable better understanding of the turbine behavior and maintenance monitoring, opening up to perform more intelligent maintenance planning and thus reducing maintenance costs. It could be possibly to continually monitor strain and motion and various critical locations, however, prior knowledge of these locations may be difficult for many structures such as a jacket structure. By designing a robust integrated model of the structure fed with motion measurements from limited locations on the structure a more robust tool for damage and fatigue estimation can be made possible anywhere on the structure.

The motivation for this thesis is to design a simplified FEM model of the 10 MW DTU reference turbine (Bak, F Zahle, and T Kim, 2014)and implement a real time state estimator for the structural response of the turbine. The possibility of monitoring the response of the turbine can aid in getting a better understanding of the true nature of the turbine response, and fatigue damage on the turbine. As of today wind turbine control systems are controlling with respect to maintaining a maximum energy capture with out taken into account the structural response. By adding the structural state estimates into the control loop, a new control scheme is possible, where a trade off between energy capture and limiting material stress inflicted from motion can be achieved.

This thesis will also serve as a work in collaboration with PhD. student Emil Smilden, where his work on designing a speed exclusion turbine control system will make use of the designed FE model and state estimator designed in this thesis.

1.2 Previous Work

Due to the high cost of O&M in offshore wind, there is ongoing extensive research in the field to reduce these costs, and increasing OWT's reliability. Figure 1.1 show some of the different subsystem which together build up the whole turbine. As can be seen, all these components build up to be a complex system where all subsystems are critical for the turbine to operate properly. To monitor the behavior of these components, various structural health monitoring (SHM) systems utilizing different principals have been investigated. Regarding the health monitoring of gearbox, drivetrain, motors etc., they can be constantly monitored through vibrations and strain monitoring. Other methods as in performed in Joosse et al. (2002) investigated the use of acoustic emission monitoring to identify cracks and deformations on small turbine blades. The acoustic emission methods may also be used for investigating behavior of parts inside the nacelle section. However, using acoustic emission detection for real time monitoring have shown to be difficult due to difficulties locating an eventual damage. Regarding blade, tower and foundation monitoring a widely used method as done in Hau (2006), has been to instrument the structure with various strain gauges at areas exposed to large stress concentration. Newer methods including fiber bragg sensors have been investigated in e.g. Bang, Ko, Jang, and

Kim (2012), where fiber bragg sensors was located along the tower structure to perform real time shape estimation and strain calculations. Work done by Papadimitriou, Fritzen, Kraemer, and Ntotsios (2011) proposed a method for estimating damage accumulation in metallic structures using output-only vibration measurements from a sensor network installed at a limited number of structural locations.

Many physical phenomena within engineering and science can be described by partial differential equation. Generally, solving these equations by analytical methods for arbitrary shapes is almost impossible. The finite element method (FEM) is a numerical method where the solution to these partial differential equations can be approximated. FE modeling is today viewed as a fundamental practice within the engineering industry for investigating approximate solutions to the behavior of complex physical models where analytical solutions do not exists. The FEM method subdivide a complex geometry over a domain into smaller simpler elements over many subdomains. By having a known solution method for the elements over the subdomains an approximation of the complex geometry over the larger domain is possible.
In the wind energy sector, FE modeling is widely used in both structural response simulations and for examining the turbine blade behavior. In addition the complex relation from soil-structure interaction of the offshore structure is often investigated using FEM.
The use of FEM models in observer design is to the authors knowledge not to well explored, Lourens, Papadimitriou, and Gillijns (2012) performed a state estimation experiment on a real footbridge with a FEM model and a limited number of acceleration measurements on the bridge, the estimator performed well even when using a modally reduced representation of the FEM model. Fritzen, Kraemer, and Klinkov (2011) considered integrated structural health monitoring of an OWT using acceleration measurements and a FE model. Their work however focused on damage detection, sensor fault detection and load identification more than the structural response of the structure.

A recently published study on the response estimation for offshore wind turbines on a jacket structure based on a FEM model was performed by Van der Male and Lourens (2015). Their results showed that the state estimate was able to track the true response of the structure with a high degree of precision.

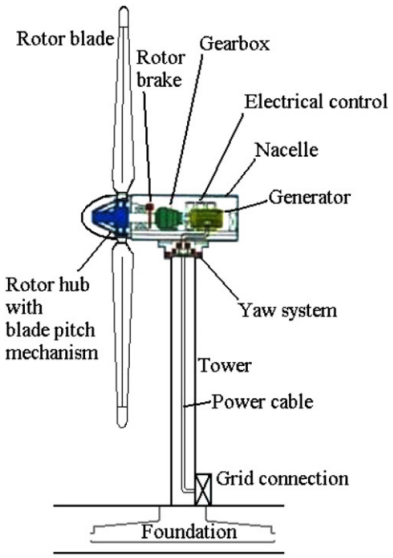

Figure 1.1: Typical configuration of a horizontal axis wind turbine (Source:(Ciang et al., 2008))

1.3 Main Contribution

This thesis will be a foundation for further control system design work by PhD. student Emil Smilden, and contribute with two different estimator designs which can be used for FE represented systems. The bias based estimator is inspired from estimator design used in Dynamic Positioning (DP) for vessels, and the $Input\text{-}state$ estimator is based on work done by Gillijns and De Moor (2007) but applied to a FE model.
To summarize, the following contributions are worked out in this thesis;

- A simplified FEM design based on the 10 MW DTU reference turbine on a monopile substructure is designed in chapter 3, and tested when exposed to varying environmental loading scenarios.

- An Input and state estimation for the 10 MW DTU FEM model is designed in chapter 4 and subjected to the modeled environmental loadings. The simulation results of the estimator are found in chapter 5, Section 5.8.

- A bias estimator for the 10 MW DTU FEM model is also designed in chapter 4 and subjected to the modeled environmental loadings. The simulation results of the estimator are found in chapter 5, Section 5.8.

Both estimators are simulated together and compared, regarding their strengths and weaknesses.

1.4 Organization of the Thesis

Chapter 2: Offshore Wind Energy

Section 2.1 gives a short presentation on the history of wind energy and the present status for offshore wind energy systems are given. In Section 2.3 the two different concepts of floating and bottom fixed turbines are addressed and discussed regarding present and future potential.

Chapter 3: Mathematical Modeling

The mathematical tools for designing the FE structural model is presented in this chapter. The model is based on the Euler Bernoulli beam elements with varying material properties. The soil structure interaction and effect of geometric stiffness is addressed in Section 3.3. Section 3.7 address modeling of some of the most dominant environmental loadings acting on a structure, including waves, wind, current and 3P loadings.

Chapter 4: Observer Design

This chapter presents two different state estimator designs for the FE model, with goal to estimate unmeasured nodal values. A dual input and state estimator is presented in Section 4.2. The proposed estimator is based on work done by Gillijns and De Moor (2007) where a corrective force estimate is obtained and used as an input to the observer model for obtaining a full state estimate. Section 4.3 presents an Kalman filter estimator where the observer model is designed with a bias force accounting for the unmodeled environmental forces, and potential modeling errors.

Chapter 5: Simulation Results

Verification and simulation of the designed FE model subjected to the varying modeled environmental loadings is addressed in Section 5.3-5.7. Multiple simulations regarding the designed estimators performances subjected to different loading scenarios will be addressed and discussed in Section 5.8.

Chapter 6: Concluding Remarks

General conclusions of the research work carried out in this thesis are discussed with suggestions for outlines on further work.

Chapter 2

Offshore Wind Energy

An introduction to the field of offshore wind energy is presented in this chapter. The chapter gives a shorthand summary of the history for harvesting energy from the wind and details about the two different concepts for offshore wind energy systems.

2.1 History of Wind Energy

Mankind has harnessed the energy in the wind for thousands of years, where the most important usage up till the invention of the steam engine was as propulsion for sail ships. For more than two thousand years, wind mills have been used for grounding grain and pumping water. The first usage of wind mills for generating electricity was introduced in 1887 by the Scottish professor James Blyth (Price, 2005). At the beginning of the 20^{th} century electricity came into use and windmills gradually became wind turbines as the rotor was connected to an electric generator. However, the interest in using wind power to generate electricity did not flourish until the oil crisis in 1973, when countries saw the importance of being less dependent on oil import, and national research programs were initiated to investigate the possibilities of utilizing wind energy. Today the growing awareness of the threat from climate changes caused by increased emission of CO_2, has increased the interest for wind energy more than ever. By 2014, over 240,000 commercial-sized wind turbines were operating in the world, producing 4% of the world's electricity (WWEA, 2014). The expected us of wind power as an important contribution to overall energy production is expected to grow, and the European Union is targeting that within 2020, 20 % of all energy consumption should come from renewable energy sources, where 12-14 % should come from wind energy (Change, 2007) . In addition to reducing CO_2 emissions wind power is relatively labor intensive and is also aiding in creating jobs. The size of wind turbines installed are gradually increasing, and more and more wind farms are designed for deployment offshore. Placing wind turbines offshore makes them applicable to harvesting more energy at more reliable rates, as wind blowing offshore is both stronger and more frequent. Placing wind turbines offshore also eliminates the visual and audial impact compared to placing a wind farm onshore. On the other hand, offshore wind farms are exposed to a much more volatile environment, where the combination of waves and wind can cause great damage to the structure, thus the cost of construction and maintenance are considerably higher.

Figure 2.1: Sheringham Shoal Offshore Wind Park, photo: Harald Pettersen/Statoil

2.2 State of the Art

In order to harvest more energy more cost effective and with higher efficiency the size of wind turbines has largely increased over the years. Over the past generation the size of wind turbines has more than quadrupled in size and effect, where a typical wind turbine built in 1980's was rated at 50 kW, there are today built turbines at 5 MW and beyond. Studies done in amongst other Caduff, Huijbregts, Althaus, Koehler, and Hellweg (2012) have shown that increasing the size of wind turbines in addition to higher energy capture also seems to be a greener and more economic feasible alternative to generating green energy at competitive prices. Figure 2.2 below shows an illustration of the trend towards building larger and larger turbines. Political legislations regarding placement and maximum size of onshore wind turbines together with limited size of road infrastructure prohibits the size of onshore wind turbines to be built much larger than they are today. On the other hand for offshore deployment, the size and transportation limitations are less significant such that the trend for larger turbines built in the future is seemed more suited for offshore deployment.

As of 2012 there were 55 offshore wind farms installed throughout Europe, generating enough electricity to power more than five million households. As of today offshore wind farms are dependent on governmental incentives to be able to generate power at a competitive price. There is much ongoing research aiming at reducing the total cost of offshore wind energy.

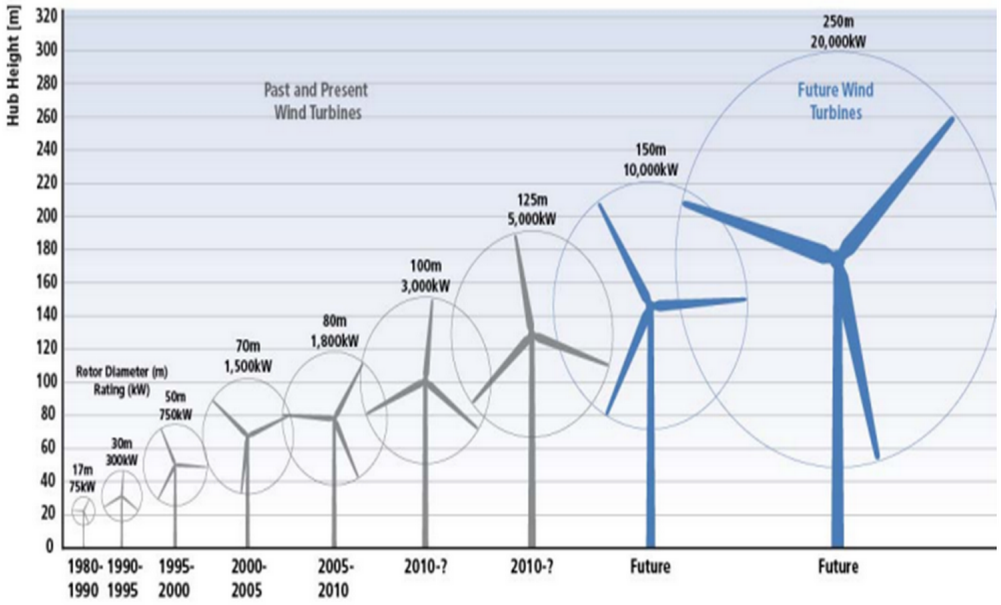

Figure 2.2: Historic and future trends in size and effect of commercial wind turbines. (Source: National Renewable Energy Laboratory)

2.3 Offshore Wind Energy Systems

There are two typical designs for wind energy systems present today. The horizontal axis wind turbine (HAWT) and the vertical axis wind turbine (VAWT). Figure 2.3 shows an illustration of the two different design concepts. The two designs utilize the same concept of a rotating shaft connected to a generator to generate electricity. As can be seen from Figure 2.3b the generator of the the VAWT is placed on ground level, which is a advantage in installation and maintenance costs. In addition, a VAWT does not need to be aligned with the wind to extract the wind energy, as opposed to a HAWT. Unfortunately the lower height of the VAWT will not let them utilize the higher and steadier wind flows which occurs at higher altitudes. The efficiency rate of a HAWT is also generally higher due to the fact that when the wind blows aligned with the HAWT turbine shown in Figur 2.3a, all the blades are able to contribute to the energy extraction of a full rotation. For a VAWT however, only a part of the blades are generating torque at any time, making them less efficient than the HAWT design.
All though the installation and maintenance cost for a HAWT is higher due to the generator placement at the tower top, the HAWT design is by far the most dominant design concept for commercial use of wind farms. This thesis will focus on the applications for a horizontal axis turbine.

When it comes to offshore wind deployment, there are two different opportunities present, bottom fixed, and floating turbines. Bottom fixed wind turbines are seen as a more mature and economically viable solution to the offshore wind segment in present time. However, a lot of research is today aimed at designing and developing floating wind turbine systems which can be deployed at deeper water, where bottom fixed turbines is not seen as a viable solution.

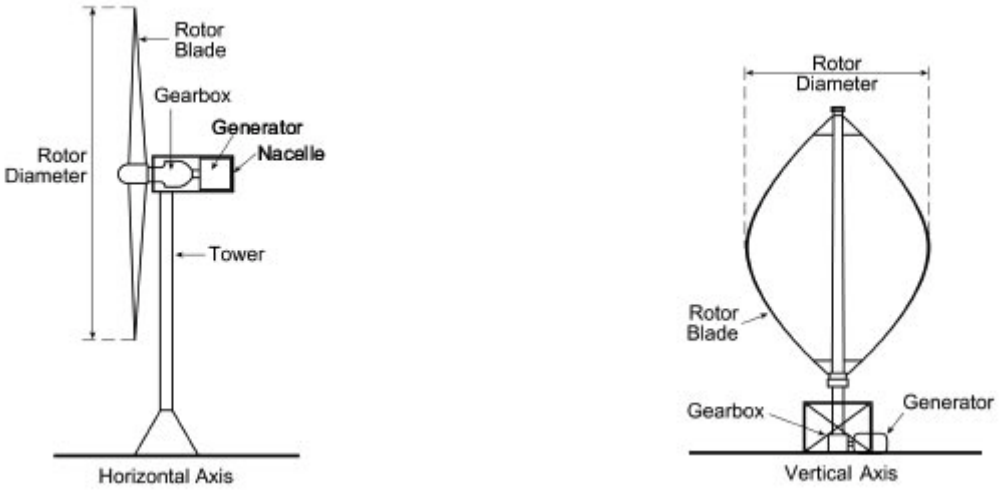

(a) HAWT (b) VAWT

Figure 2.3: The two concepts of horizontal axis wind turbine (HAWT) and vertical axis wind turbine (VAWT)

2.3.1 Floating Wind Turbines

Floating wind turbine concepts are still at an early stage, where as of today there are no existing floating offshore wind farms. Several countries in the world have a steep incline in water depths close to their coastline, making bottom fixed turbines unsuited. This applies to e.g. the two developing countries India and China, where both are consuming large amounts of the world's total energy consumption. Figure 2.4 show the average wind speed in January 2008 around the world. If taken as a general indication of the wind conditions in the world it is seen that for some countries it is necessary to deploy wind farms far from shore to be able to obtain wind conditions with sufficient energy. Water depths far from shore tends to be deeper such that bottom fixed solution may not be seen as an alternative. Today, Japan, a country with deep water surroundings are currently planning to build a pilot floating wind farm, with six 2-megawatt turbines, off the Fukushima coast of northeast Japan [1]. The advantage of floating wind turbine systems besides water depth restrictions are the possibility of assembling the turbine at shore before towing it out to designated site. Removing the need for jackup rigs and other installation vessels, has potential to greatly decrease the overall installation cost.
Through the offshore oil and gas industry a lot of experience has been obtained by designing floating marine structures which can be utilized in designing floating wind turbines. Figure 2.5 one can observe three different concepts for floating wind. Another advantage with floating wind turbines are for earthquake exposed countries, where having floating systems will make them less vulnerable to devastating earthquakes. Unfortunately, as of today there are no clear design winner in when it comes to mass deployment and the industry is still facing many years of research before a economically competitive floating wind farm is probable (Butterfield et al., 2007).

[1] http://www.japantimes.co.jp/life/2013/04/04/environment/project-tests-viability-of-offshore-floating-wind-turbines/#.VW3422TtlBe

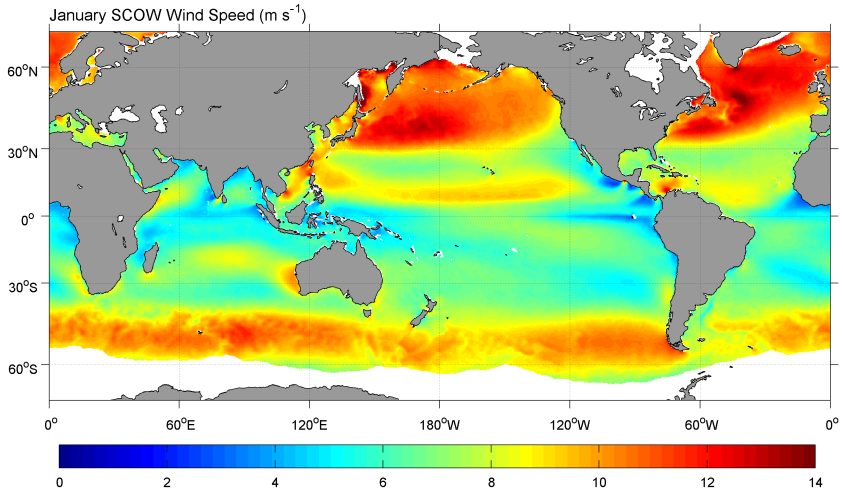

Figure 2.4: Figure showing average wind speed in the world in Januray 2008 Source:(Risien and Chelton, 2008)

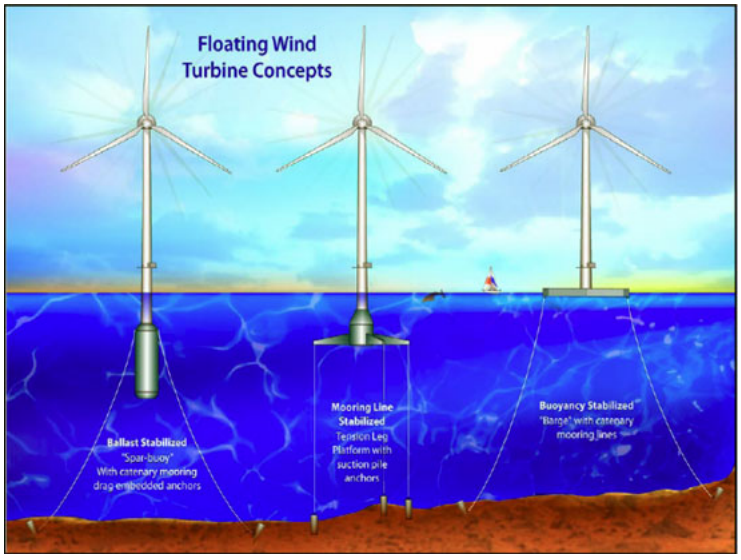

Figure 2.5: Three different floating wind turbine concepts (Courtesy of the U.S. Department of Energy)

2.3.2 Bottom Fixed

The most significant difference between a onshore and offshore wind turbine is the need of a foundation design for the turbine to operate on. The experience achieved through the oil and gas industry has led to good knowledge about design requirements for offshore structures, which can be utilized for offshore wind turbines. However, due to the complex nature of the loading conditions for an offshore wind turbine, there are still many challenges in making the structure design smarter and cheaper.

The vast majority of offshore wind turbine systems consist of monopile substructures, followed by gravity based structures. The different foundation concepts are suitable for varying water depths and soil properties. In general the monopile structure is chosen for water depths up to 30 m, while the remanning foundation designs are deployed for water depths $30-80$ m. The different foundation designs all have their pros and cons when it comes to installation, cost, and durability. The monopile foundation is often selected due to its simplicity and low cost. Figure 2.6 show different foundation structures typically used in offshore wind turbine foundations. A monopile foundation design will be used as substructure in this thesis. The whole substructure is generally called a monopile, however, as Figure 2.7 shows, it is only the soil piercing part of the structure which is named the monopile. The whole substructure consists of the monopile and a transitional piece. The monopile is a single column base which is pounded into the seabed before the transitional piece is mounted on to the monopile. The free spacing between the monopile and the transitional piece is grouted to inhibit relative motion between the two pieces.

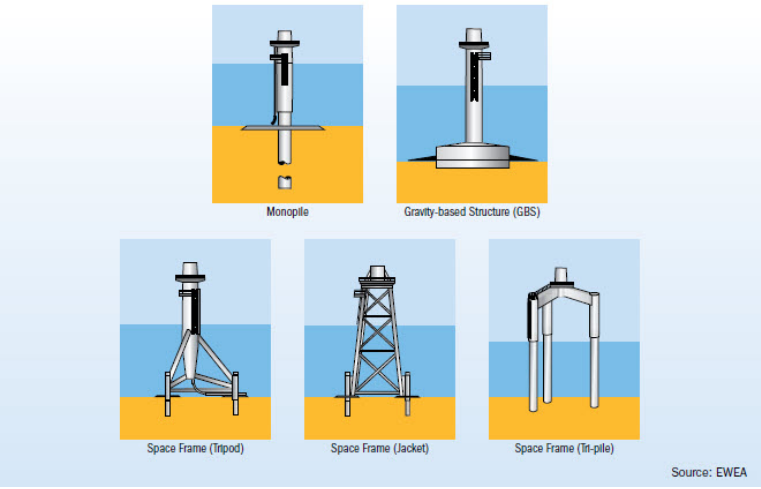

Figure 2.6: Typical fixed offshore foundations (Source: EWEA)

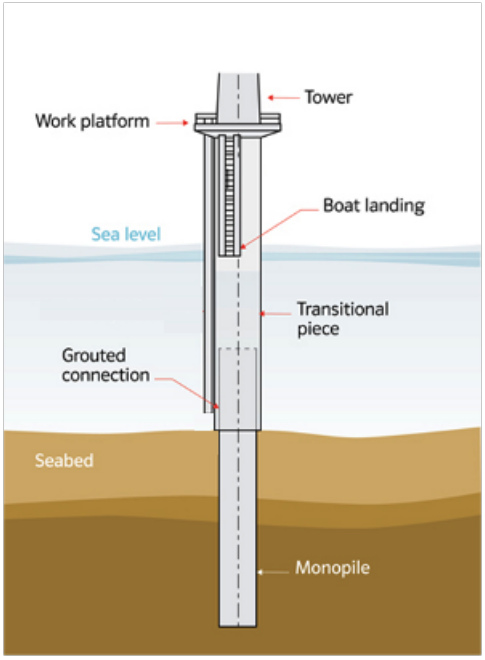

Figure 2.7: Structure of a monopile foundation used for offshore wind applications (Source: Garrad Hassan and Partners Ltd.)

Chapter 3

Mathematical Modeling

In this chapter the necessary theory for modeling the finite element model for the structure is presented. The modeled turbine structure will consist of a monopile section, a foundation (transition piece) section and a tower section. The structure is modeled with 3 degrees of freedom in each node,transversal, rotational and axial. The transversal and rotational degrees of freedom (DOF) will be modeled by beam elements, and the DOF is modeled from bar elements. The turbine is located at 30 m water depth. An illustration of the model and its different sections can be seen in Figure 3.1. Environmental disturbances from waves, wind and rotor interaction will also be modeled. Instead of explicitly modeling the turbine blades, an equivalent wind thrust force from wind turbine momentum theory with the give blade radius will be modeled and applied to the turbine structure top. The weight of the tower top nacelle, will be modeled as a point load, with weight equal to the sum of the blades, rotor, hub etc.

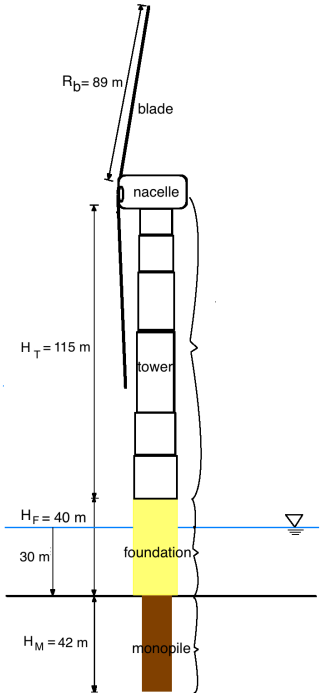

Figure 3.1: The considered wind turbine model used in FE model design

3.1 Finite Element Formulation

As the mechanical properties of the turbine structure change over the length it is modeled over, an analytical solution for the displacement, strain, stress etc. is not possible to obtain. An approximated solution through finite element formulation can therefore be used, by dividing the structure into smaller, simpler segments with constant mechanical properties over each segment. Each segment will be connected to another through their common node. By calculating the nodal values, it is possible through interpolation functions to approximate a solution for the displacement, strain, stress etc. anywhere along the modeled structure.
The structure will be divided into N 2-noded elements, where each node will have 3 degrees of freedom (DOF). An illustration of an element can be seen in Figure 3.2. Each element will have a total of six nodal values which has to be determined from solution of the FE problem. The six nodal values for each element can be grouped into a nodal vector $\mathbf{d}^e$, written as,

$$\mathbf{d}^e = \begin{bmatrix} u_1 \\ v_1 \\ \theta_1 \\ u_2 \\ v_2 \\ \theta_2 \end{bmatrix}, \tag{3.1}$$

where the u_i, v_i, θ_i, $i = [1,2]$, represents the axial, transversal and rotational degree of freedom respectively. The formulation of equations and matrices necessary to perform a FE solution of the modeled structure will be divided into two parts, the first will be formulating the procedure for the transversal and rotational DOF's, using Euler-Bernoulli beam elements. The second part will model the axial DOF as bar elements. At last the the modeled DOF's will be grouped together into the resulting system matrices.

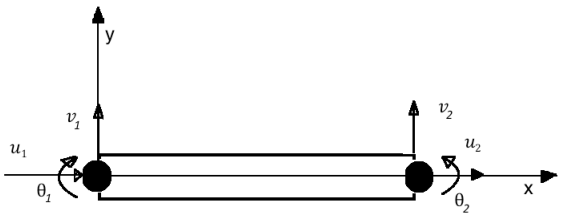

Figure 3.2: Degrees of freedom on a 2 node beam element

3.1.1 Transversal and Rotational Degree of Freedom

When applying Euler-Bernoulli beam elements to describe the transversal and rotational degree's of freedom, the following assumptions has to be governed for the beam element analysis to be valid.

Slender beam: It is assumed that the beam length L to its thickness h is large. By this assumption, shear stress from transversal loading will be neglected, and all stress contribution is assumed from bending stress.

Orthogonal Planes Remain Orthogonal: By neglecting shear forces originally orthogonal planes remains orthogonal after an applied load.

Small Deformations: An originally straight and narrow beam remains straight and narrow when loaded.

Linear Elastic Material: The beam element displaces as a linear function relative to the applied load, i.e. Hooke's law applies. In addition the material is assumed isotropic and homogenous.

Plane Stress: It is assumed that beam only experience plane stress, and that the value increases linearly from zero at the neutral axis, to maximum at the top and bottom surface.

The governing equation for the beam elements is the fourth order differential equation for a beam, given as,

$$EI\frac{d^4v(x)}{dx^4} - p = 0, \tag{3.2}$$

where p is an externally applied force, E is young's modulus, I is the moment of inertia and $v(x)$ is the transversal displacement of the beam element's midline. In the derivation of the the beam's governing differential equation it is assumed that $\frac{d^2v(x)}{dx^2}$ express the curvature of the beam. From this, the expression for axial strain in the beam element at a distance y from the neutral line can be expressed as $\epsilon = -y\frac{d^2v(x)}{dx^2}$. Details on the full derivation of the beam's differential equation can be found in many engineering text books, e.g. (Fish and Belytschko, 2007).

To develop a finite element formulation for a beam element it is necessary to transform the governing differential equation (3.2) from its strong form representation to a weak form representation. The weak form formulation is an equivalent representation but written on an integral form. Combining the weak form representation with weight and trial functions are necessary to develop the discrete finite element equations. Derivation of the weak form representation is beyond the scope of this work, but can be found in Fish and Belytschko (2007).

To describe the behavior along the element length, interpolation functions are needed. It is necessary to obtain continuity in both displacement and slope between elements, which means

that the approximation functions have to be C^1 continuous. A C^1 continuous function is a function where both the function f and its derivative f' are continuous.
The widely used shape functions for approximating the displacement and rotation along a beam element, are known as *Hermitian cubic* shape functions. They satisfy the C^1 continuity requirement and are given as;

$$\begin{aligned} N_{v1} &= \frac{1}{4}(1-\xi)^2(2+\xi), \\ N_{\theta 1} &= \frac{l^e}{8}(1-\xi)^2(1+\xi), \\ N_{v2} &= \frac{1}{4}(1+\xi)^2(2-\xi), \\ N_{\theta 2} &= \frac{l^e}{8}(1+\xi)^2(\xi-1). \end{aligned} \tag{3.3}$$

The shape functions in (3.3) are expressed in terms of a natural coordinate ξ, given as,

$$\xi = \frac{2x}{l^e} - 1, \qquad 0 \leq x \leq l^e \tag{3.4}$$

where l^e represents the element length. As can be seen from expression (3.4), the variable linearly varies from -1 and 1. The interpolated value for a transverse displacement $v(x)$ anywhere along the beam element is the linear combination of nodal displacements and rotations, which can be written as,

$$v(x) = \sum_{i=1}^{4} N_i^e d_i^e = \begin{bmatrix} N_{v1} & N_{\theta 1} & N_{v2} & N_{\theta 2} \end{bmatrix} \begin{bmatrix} v_1 \\ \theta_1 \\ v_2 \\ \theta_2 \end{bmatrix} = \mathbf{N}^e \mathbf{d}^e. \tag{3.5}$$

Stiffness Matrix and Elemental Force Vector

To develop the stiffness matrix and force vector for the beam element one can utilize the theorem of minimum potential energy. The minimum potential energy theorem states that the structure of a body shall displace to a position which minimizes its total potential energy. On equation form the total potential energy Π is given as,

$$\Pi = W_{int} - W_{ext}, \tag{3.6}$$

where W_{int} and W_{ext} represents the internal and external potential energy, respectively. As stated earlier, Euler-Bernoulli theory only take into account the bending energy, such that the internal potential energy can be expressed as

$$W_{int} = \frac{1}{2}\int_{\Omega} E\epsilon^2 d\Omega = \frac{1}{2}\int_0^{l^e}\int_A E\epsilon^2 dA dx = \frac{1}{2}\int_0^{l^e} EI(\frac{d^2 v(x)}{dx^2})^2 dx. \tag{3.7}$$

In (3.7) the assumption $\epsilon = -y\frac{d^2v(x)}{dx^2}$ is used. The moment of inertia I is derived from $I = \int y^2 dA$. The external work accounts for the transverse applied forces, and can be given as,

$$W_{ext} = \int_0^{l^e} p(x)v(x)dx, \tag{3.8}$$

where $p(x)$ represents the applied forces. To obtain an approximated expression for $\frac{d^2v(x)}{dx^2}$, one can use the double derivative of (3.5) with respect to x, such that $\frac{d^2v(x)}{dx^2}$ can be given as,

$$\frac{d^2v(x)}{dx^2} = \mathbf{B}^e\mathbf{d}^e. \tag{3.9}$$

$\mathbf{B}^e$ is given by

$$\mathbf{B}^e = \frac{d^2\mathbf{N}^e}{dx^2} = \frac{1}{l^e}\left[\frac{6\xi}{l^e} \quad 3\xi - 1 \quad -\frac{6\xi}{l^e} \quad 3\xi + 1\right]. \tag{3.10}$$

When taking the derivative of the expression in (3.5), with respect to x, the relation $\frac{d}{dx} = \frac{l^e}{2}\frac{d}{d\xi}$ has been used. Inserting the approximated expressions for $\frac{d^2v(x)}{dx^2}$, and transverse displacements into (3.6), gives the quadratic form of nodal displacements. This gives that,

$$\Pi = \frac{1}{2}\mathbf{d}^T\left(\int_{l^e} EI\mathbf{B}^{eT}\mathbf{B}^e dx\right)\mathbf{d} - \mathbf{d}^T\int_{l^e}\mathbf{N}^{eT}p(x)dx, \tag{3.11}$$

which can be rewritten as,

$$\Pi = \frac{1}{2}\mathbf{d}^{eT}\mathbf{K}^e\mathbf{d}^e - \mathbf{d}^{eT}\mathbf{f}. \tag{3.12}$$

From this the element stiffness matrix $\mathbf{K}^e$ is obtained as,

$$\mathbf{K}^e_{bm} = \int_{l^e} EI\mathbf{B}^{eT}\mathbf{B}^e dx = \int_{-1}^{1} EI\mathbf{B}^{eT}\mathbf{B}^e\frac{1}{2}l^e d\xi. \tag{3.13}$$

For a beam element with constant cross section and elastic modulus across the element this gives an element stiffness matrix;

$$\mathbf{K}^e_{bm} = \frac{EI^e}{l^{e3}}\begin{bmatrix} 12 & 6l^e & -12 & 6l^e \\ 6l^e & 4l^{e2} & -6l^e & 2l^{e2} \\ -12 & -6l^e & 12 & -6l^e \\ 6l^e & 2l^{e2} & -6l^e & 4l^{e2} \end{bmatrix}. \tag{3.14}$$

The vector $\mathbf{f}^e$ in (3.12) represents the elemental nodal forces, and is given as,

$$\mathbf{f}^e = \int_{l^e}\mathbf{N}^{eT}p(x)dx = \int_{-1}^{1}\mathbf{N}^{eT}p(\xi)\frac{1}{2}l^e d\xi. \tag{3.15}$$

As can be seen from (3.15), the nodal force vector is dependent on the variation of the load vector $p(x)$ along the element length. If approximated as an evenly distributed load over the element length, the force vector becomes

$$\mathbf{f}^e = \begin{bmatrix} F_1 \\ M_1 \\ F_2 \\ M_2 \end{bmatrix} = \frac{1}{2} p l^e \begin{bmatrix} 1 \\ \frac{1}{6} l^e \\ 1 \\ -\frac{1}{6} l^e \end{bmatrix}, \tag{3.16}$$

where p is the amplitude of the load. F_i,M_i for $i = [1,2]$ is the transversal nodal force, and nodal moment, respectively.

Inertia Matrix

To construct the inertia matrix for the beam element we look at the kinetic energy of the beam due to lateral motion. The kinetic energy T^e of a beam element with density ρ in a velocity field $\dot{\tilde{\mathbf{v}}}$ is given by,

$$T^e = \frac{1}{2} \int_{\Omega^e} \rho (\dot{\tilde{\mathbf{v}}})^T \dot{\tilde{\mathbf{v}}} d\Omega^e. \tag{3.17}$$

By the assumption that one can use the shape functions to interpolate the velocity anywhere in the beam element, $\dot{\tilde{\mathbf{v}}}$ can be written as, $\dot{\tilde{\mathbf{v}}} = \mathbf{N}^e \dot{\mathbf{d}}^e$. The kinetic energy equation can then be given by

$$T^e = \frac{1}{2} \int_{\Omega^e} \rho (\dot{\tilde{\mathbf{v}}})^T \dot{\tilde{\mathbf{v}}} d\Omega^e = \frac{1}{2} (\dot{\mathbf{d}}^e)^T \left(A \int_0^{l^e} \rho (\mathbf{N}^e)^T \mathbf{N}^e \frac{1}{2} l^e d\xi \right) \dot{\mathbf{d}}^e := \frac{1}{2} (\dot{\mathbf{d}}^e)^T \mathbf{M}^e \dot{\mathbf{d}}^e. \tag{3.18}$$

From (3.18) it is easily seen that the inertia matrix will be given by,

$$\mathbf{M}^e_{bm} = A \int_0^{l^e} \rho (\mathbf{N}^e)^T \mathbf{N}^e \frac{1}{2} l^e d\xi. \tag{3.19}$$

Integrating the expression above over its element length, the element inertia matrix for a beam element ends up as,

$$\mathbf{M}^e_{bm} = \frac{\rho A}{420} \begin{bmatrix} 156 & 22l^e & 54 & -13l^e \\ 22l^e & 4l^{e2} & 13L_{el} & -2l^{e2} \\ 54 & 13l^e & 156 & -22l^e \\ -13l^e & -3l^{e2} & -22l^e & 4l^{e2} \end{bmatrix}. \tag{3.20}$$

Added Mass

Due to the presence of water, the water covered part of the structure will have an added hydrodynamic inertia known as added mass. In a physical sense, this added mass is the weight added to a system due to the fact that an accelerating or decelerating body must displace some volume of surrounding fluid with it as it moves. The added mass force opposes the motion and for a cylinder shaped structure using potential theory, the added mass per element length is equal to

the volume of the displaced water multiplied by the water density, $M_a = \pi \frac{D^2}{4} \rho_w$ [kg/m] (Faltinsen, 1993). The total inertia matrix for the water covered part of the structure will then add up as

$$\mathbf{M}_a^e = \left(\frac{\rho A}{420} + \pi \frac{D^2}{4} \rho_w \right) \begin{bmatrix} 156 & 22l^e & 54 & -13l^e \\ 22l^e & 4l^{e2} & 13L_{el} & -2l^{e2} \\ 54 & 13l^e & 156 & -22l^e \\ -13l^e & -3l^{e2} & -22l^e & 4l^{e2} \end{bmatrix}. \tag{3.21}$$

3.1.2 Axial Degree of Freedom

The axial displacement of the nodes will be described as done for an axially loaded bar. The technical definition of a bar is that it is only subjected to axial loads. The fundamental assumption is that the displacements are within the linear region, i.e. Hooke's law apply.

Stiffness Matrix

The elongation δ^e of an element can be expressed in terms of nodal displacements, $\delta^e = u_2^e - u_1^e$. Because of this assumption one can treat the force relation similar as to a spring, such that the elemental force is given as

$$F^e = k^e(u_2 - u_1), \tag{3.22}$$

where k^e is the elemental stiffness, and given as

$$k^e = \frac{A^e E}{l^e}. \tag{3.23}$$

From force equilibrium of a bar elements as in Figure 3.3 it is easily seen that

$$F_1^e = -F_2^e = k^e(u_2 - u_1). \tag{3.24}$$

The equation above can on matrix form be written as,

$$\begin{bmatrix} F_1^e \\ F_2^e \end{bmatrix} = \frac{A^e E}{l^e} \begin{bmatrix} 1 & -1 \\ -1 & 1 \end{bmatrix} \begin{bmatrix} u_1^e \\ u_2^e \end{bmatrix} \tag{3.25}$$

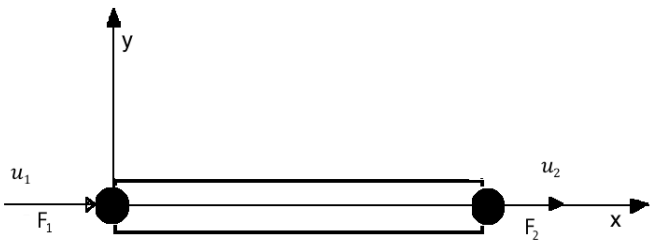

Figure 3.3: Bar element

which on short form notation translates to

$$\mathbf{F}^e = \mathbf{K}_b^e \mathbf{d}_b^e. \tag{3.26}$$

Using the linear interpolation functions for a bar element

$$\mathbf{N}_b^e = \begin{bmatrix} 1-\xi \\ \xi \end{bmatrix}, \quad \xi \in [0,1], \tag{3.27}$$

one can obtain a expression for the axial displacement $a(\xi)$ along the bar element by a linear combination of the nodal displacements in $\mathbf{d}_b^e$, such that

$$a(\xi) = \mathbf{N}_b^e \mathbf{d}_b^e. \tag{3.28}$$

Inertia Matrix

The inertia matrix of the bar element can be derived in the same manner as for the beam element, where the kinetic energy of the particles in the beam was integrated. Using the shape functions given in (3.27) the elemental inertia matrix $\mathbf{M}_b^e$ is obtained by

$$\begin{aligned} \mathbf{M}_b^e &= \int_\Omega \rho (\mathbf{N}_{bar}^e)^T \mathbf{N}_{bar}^e d\Omega \\ &= \rho A \int_0^1 \begin{bmatrix} 1-\xi \\ \xi \end{bmatrix} \begin{bmatrix} 1-\xi & \xi \end{bmatrix} l^e d\xi \\ &= \frac{1}{6} \rho A l^e \begin{bmatrix} 2 & 1 \\ 1 & 2 \end{bmatrix}. \end{aligned} \tag{3.29}$$

Here the transformation $dx = l^e d\xi$ have been used to convert between element coordinates and the natural coordinate.

3.2 Geometric Stiffness

The large weight of the turbine top nacelle and blades will yield a large compressive force on the structure. This compressive force will decrease the effective stiffness of the structure. This effect can be accounted for by introducing a *geometric stiffness matrix*. The change in stiffness due to the top weight is implemented based on energy concepts. As before, small lateral deflections along the turbine tower are assumed. As done in (Cook et al., 2007) one start by assuming that the lateral displacement $v(x)$ takes place without any axial displacement $u(x)$. By applying a compressive force P, each differential length dx becomes a new differential length ds. Due to the compressive force one assume $ds < dx$. Using Figure 3.4 and the small angle approximation $(tan(\theta) \approx \theta)$ one can approximate the new line segment ds as,

$$\begin{aligned} ds &= \sqrt{1 + v_x^2} \cdot dx, \\ ds &\approx (1 + \frac{1}{2} v_x^2) \cdot dx. \end{aligned} \tag{3.30}$$

The last approximation in equation (3.30) above is obtained by using Taylor expansion on the square root expression and only keeping the two first terms. $v_x = \frac{dv(x)}{dx}$ represents the slope of the beam displacement. The axial strain in the beam is then given by

$$\epsilon_a = \frac{ds - dx}{dx} = \frac{ds}{dx} - 1. \tag{3.31}$$

This expression can by using the argument in (3.30) be approximated as

$$\epsilon_a \approx \left(1 + \frac{1}{2}v_x^2\right) - 1 = \frac{1}{2}v_x^2. \tag{3.32}$$

Due to the small displacements assumption, one can assume that the compressive force from the tower top weight to remains constant. The compression of a line segment dx will perform work on the beam element, which will be stored as potential energy. A differential part of this potential energy equals $P \cdot \epsilon dx$. This implies that the total internal potential energy due to axial compression equals

$$\begin{aligned} W_{int} &= \int_0^{l^e} P\epsilon_a \cdot dx, \\ W_{int} &= \frac{1}{2}P\int_0^{l^e} v_x^2 \cdot dx. \end{aligned} \tag{3.33}$$

Using the expression for lateral displacement anywhere along the beam given in (3.5), and differentiating it, the slope of lateral displacement can be written as,

$$v_x = \mathbf{d}^e \frac{d\mathbf{N}^e}{dx}. \tag{3.34}$$

Inserting this into (3.33), the new expression for internal work can be rewritten as,

$$W_{int} = \frac{1}{2}\mathbf{d}^{eT}\left(P\int_0^{l^e}\left(\frac{d\mathbf{N}^e}{dx}\right)^T \frac{d\mathbf{N}^e}{dx}\frac{l^e}{2}dx\right)\mathbf{d}^e. \tag{3.35}$$

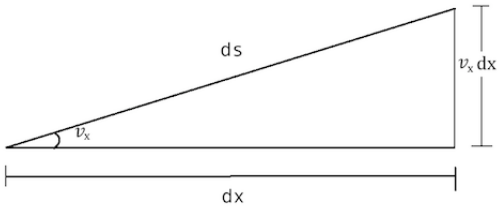

Figure 3.4: Geometric relation between line segment dx and compressed segment ds

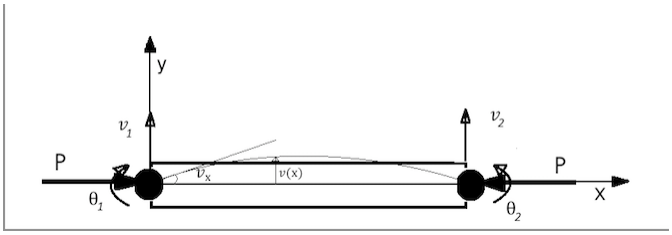

Figure 3.5: Beam element subjected to a compressive force P

By the assumption of constant compressive force P, the element geometric stiffness matrix becomes

$$\mathbf{K}_{\sigma}^{e} = P \int_{0}^{l^e} \left(\frac{d\mathbf{N}^e}{dx} \right)^T \frac{d\mathbf{N}^e}{dx} \frac{l^e}{2} dx. \tag{3.36}$$

After integration over the element length, this turns out to be

$$\mathbf{K}_{\sigma}^{e} = \frac{P}{30l^e} \begin{bmatrix} 36 & 3l^e & -36 & 3l^e \\ 3l^e & 4l^{e2} & -3l^e & -l^{e2} \\ -36 & -3l^e & 36 & -3l^e \\ 3l^e & -l^{e2} & -3l^e & 4l^{e2} \end{bmatrix}. \tag{3.37}$$

The compressive force P represents the total force front the weight of the tower top, including blades, rotor nacelle etc.

3.3 Soil Interaction

The monopile section of the structure will have an added stiffness due to the presence of soil. The true interaction between the soil and structure is a very complex and difficult problem to accurately model. In general, refined FE models are needed to get a good understanding of the coupled behavior between the structure and the soil. The type of soil is dependent on site location, and generally varying with the depth beneath ground, making the problem of accurate modeling soil structure interaction even more complex. The behavior of the soil tend to change with time from effects of turbine vibration and scouring. When a structure is placed offshore, the presence of the structure causes a local increase of current and wave motions. This increased water flow stir the seabed particles close to the structure and transport them away, creating a hole around the structure. This phenomena is known as scour (Van der Tempel, Zaaijer, and Subroto, 2004). A tall flexible structure with a large top mass as a wind turbine will have a relatively low first eigenfrequency, which for some sea states can lie close to the peak frequency of the sea state. If occurrence of a scour hole, the effective "length" of the structure will increase, and thus lowering the eigenfrequency further, making it more exposed to fatigue damage from wave interaction. Scour protection can be done by dumping large amount of rocks or protective mats around the structure. This is expensive and requires regular inspections and occasional maintenance (Van der Tempel et al., 2004).

As a simplified approach, a pressure-displacement model will be presented. The pressure-displacement method is based on *Winkler* foundation theory, a widely used method in civil and offshore engineering due to its simplicity and sufficient results for early design methods.

3.3.1 Winkler Theory

The Winkler model considers the interaction between the model and the soil as a finite amount of non-linear springs, where the spring stiffness depends on the type of soil the structure interacts with. Figure 3.6 shows how the soil interaction can be modeled as springs, giving added stiffness of the soil covered part of the structure. The added stiffness to each element is assumed

independent of each other, which results in a diagonal stiffness matrix consisting of the independent springs constants given as,

$$\mathbf{K}^{e}_{soil} = \begin{bmatrix} k(y)_1 & & & \\ & k(y)_2 & 0 & \\ & & \ddots & \\ & 0 & & k(y)_N \end{bmatrix}. \tag{3.38}$$

Because of its simplicity, the model also have some shortcomings on accuracy. The primary deficiency of the model is that one neglects the shear capacity in the soil (Caselunghe and Eriksson, 2012). By neglecting the shear stress, there is no spread in the displacements in the transverse direction, and discontinuities in the displacements between the loaded and the unloaded surfaces. In reality this is not the scenario, as there are no discontinuities in the displacement. Figure 3.7 gives an illustration of the effect of neglecting shear stress compared to a more realistic scenario.

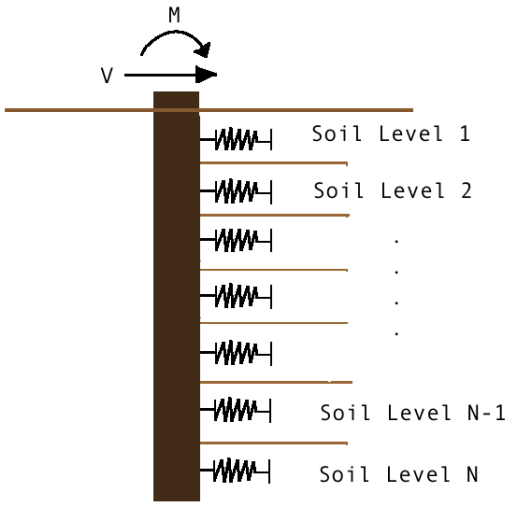

Figure 3.6: Winkler Model consisting of N independent springs

The monopile section is divided into N elements, where an added stiffness proportional to the soil stiffness is added to the nodes in transversal direction. To estimate the spring stiffness against lateral displacement for the varying soil depth, a method based on *pressure - displacement* curves (*P-Y curves)* is used.

3.3.2 The Pressure - Displacement Method

$P-y$ curves are empirically obtained for different kind of soil, and show the soil resistance (pr. unit length) per m displacement. The type of soil and its stiffness properties are typically varying with depth beneath ground. Figure 3.8a and 3.8b show the The $P-y$ curves used in modeling

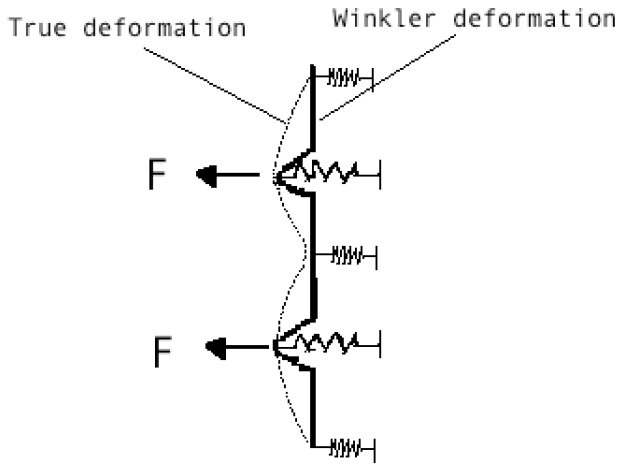

Figure 3.7: Deformed beam with and without the effects of shear deformation

the turbine structure. They consist of 26 levels, and are obtained from a soil combination which can be found at the offshore turbine site $Dogger\ bank$. The numerical data used can be found in Appendix B. The soil stiffness for a displacement y_i is obtained as,

$$k_i(y) = \frac{dP(y)}{dy} \cdot l^e \quad , \quad i = [1,2,...25,26], \tag{3.39}$$

where $k_i(y)$ is the differentiated numerical data given in the $P-y$ curves multiplied by the element length l^e. The varying stiffness added to each node along the monopile are represented in Figure 3.8c and 3.8d. As figure 3.8c and 3.8d show, the stiffness is higher for increased depth beneath the ground. As the figures, show, there number of data points are higher for the soil level located closest to the seabed, which gives a smoother transition and no discontinuities in the soil stiffness values. For the soil stiffness given in Figure 3.8d, the discontinuities has been catered for by assuming constant soil stiffness within a given displacement.

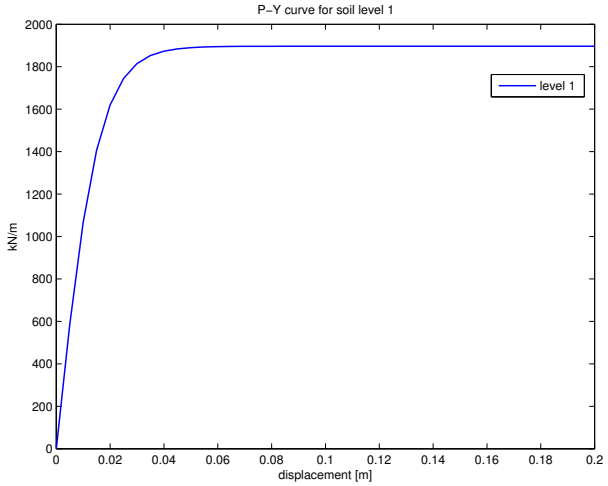

(a) $P-y$ curve for soil level 1

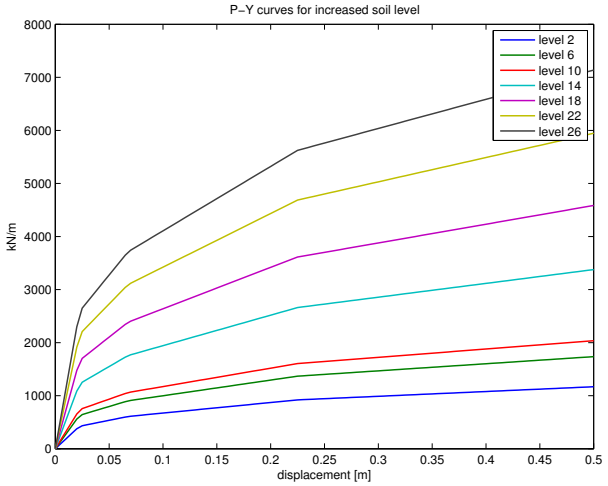

(b) $P-y$ curves for increasing soil depth

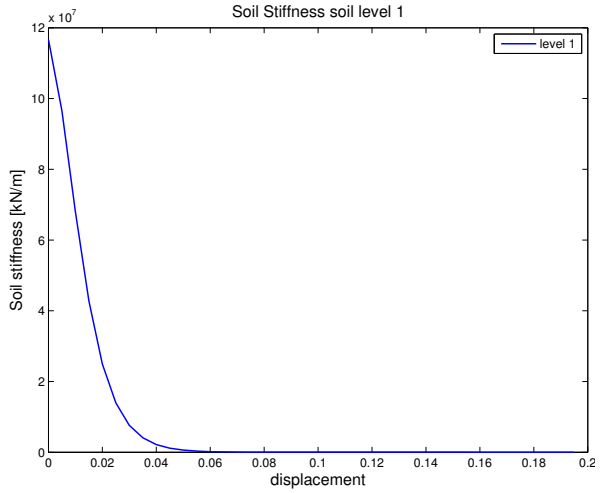

(c) Soil Stiffness for soil level 1

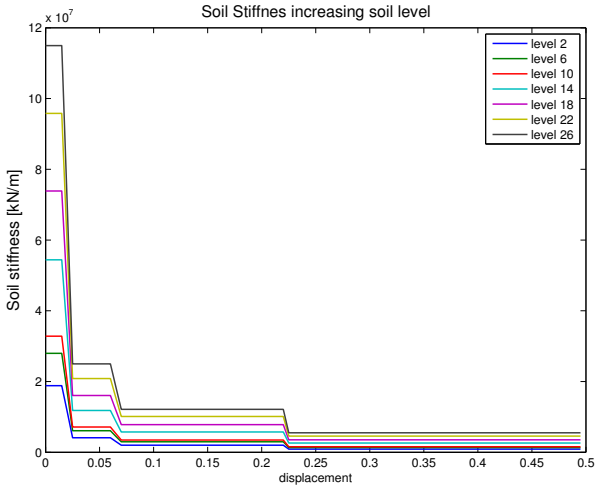

(d) Soil stiffness increasing soil depth

Figure 3.8: Varying Pressure-displacement curves and soil stiffness for increasing soil depth

3.4 Resulting Inertia and Stiffness Matrices

Having derived the necessary element matrices for inertia and stiffness, they can be combined to give the resulting element matrices used in assembling the total system. Effects of system damping will be considered in Section 3.8

Inertia Matrix

Combining the inertia matrix for the bar and beam element gives the resulting 6DOF inertia elemental matrix, $\mathbf{M^e}_T$,

$$\mathbf{M^e}_T = \mathbf{M^e}_{bm} + \mathbf{M^e}_{bar} = \frac{\rho A}{420}\begin{bmatrix} \frac{l^e}{3} & 0 & 0 & \frac{l^e}{6} & 0 & 0 \\ 0 & 156 & 22l^e & 0 & 54 & -13l^e \\ 0 & 22l^e & 4l^{e2} & 0 & 13l^e & -2l^{e2} \\ \frac{l^e}{6} & 0 & 0 & \frac{l^e}{3} & 0 & 0 \\ 0 & 54 & 13l^e & 0 & 156 & -22l^e \\ 0 & -13l^e & -3l^{e2} & 0 & -22l^e & 4l^{e2} \end{bmatrix}. \tag{3.40}$$

For the water covered part of the structure, the addition of added mass has to be taken into account for the respective elemental matrices.

Stiffness Matrix

Combining the stiffness elements for the beam, bar and geometric stiffness yields the resulting 6DOF stiffness matrix, $\mathbf{K^e}_T$,

$$\mathbf{K^e}_T = \left(\mathbf{K^e}_{bm} + \mathbf{K^e}_b\right) + \mathbf{K^e_\sigma}$$

$$= \underbrace{\frac{EI^e}{l^{e3}}\begin{bmatrix} \frac{A^e l^{e2}}{I^e} & 0 & 0 & -\frac{A^e l^{e2}}{I^e} & 0 & 0 \\ 0 & 12 & 6l^e & 0 & -12 & 6l^e \\ 0 & 6l^e & 4l^{e2} & 0 & -6l^e & 2l^{e2} \\ -\frac{A^e l^{e2}}{I^e} & 0 & 0 & \frac{A^e l^{e2}}{I^e} & 0 & 0 \\ 0 & -12 & -6l^e & 0 & 12 & -6l^e \\ 0 & 6l^e & 2l^{e2} & 0 & -6l^e & 4l^{e2} \end{bmatrix}}_{\mathbf{K^e}_{beam} + \mathbf{K^e}_{bar}} + \underbrace{\frac{P}{30l^e}\begin{bmatrix} 0 & 0 & 0 & 0 & 0 & 0 \\ 0 & 36 & 3l^e & 0 & -36 & 3l^e \\ 0 & 3l^e & 4l^{e2} & 0 & -3l^e & -l^{e2} \\ 0 & 0 & 0 & 0 & 0 & 0 \\ 0 & -36 & -3l^e & 0 & 36 & -3l^e \\ 0 & 3l^e & -l^{e2} & 0 & -3l^e & 4l^{e2} \end{bmatrix}}_{\mathbf{K^e}_\sigma}. \tag{3.41}$$

For the monopile part of the element model, the added stiffness from soil interaction given by (3.38) is added to the elemental stiffness matrix in (3.41), such that the total element stiffness matrix for the monopile elements becomes

$$\mathbf{K^e}_{mono} = \mathbf{K^e}_T + \mathbf{K^e}_{soil}. \tag{3.42}$$

Element Load vector

The element load vector given in (3.15) is expanded to account for the possibility of axial loading. Since axial forces only attack through a node, no shape functions are necessary to represent them. The load vector is then given by,

$$\mathbf{f^e} = \frac{1}{2} l^e \int_{-1}^{1} \tau(\xi) \begin{bmatrix} 0 \\ N_{v1} \\ N_{\theta 1} \\ 0 \\ N_{v2} \\ N_{\theta 2} \end{bmatrix} d\xi + \begin{bmatrix} 1 \\ 0 \\ 0 \\ 1 \\ 0 \\ 0 \end{bmatrix} \tau_a, \tag{3.43}$$

where $\tau(\xi)$ is the transversal load, and τ_a is the axial load.

3.5 Element Sensitivity

When simulating the response of the structure subjected to different environmental loads the number of elements can be of importance. A transversal response for an element between two nodes is obtained by interpolating the nodal values using (3.5). An axial displacement is obtained by using (3.28). When any distributed load is present, acting along the element length, it will have to be transformed to an equivalent nodal load using (3.43). The equivalent nodal forces will produce exact displacements exactly at the nodes. An increase in number of elements will not produce a better approximation. On the other hand, when approximating displacements along the elements length with the interpolations functions, an increase in number of elements can produce a better approximation.

3.6 Bending Moment and Stress Calculations

Stress and bending moment calculation is of great importance when monitoring the behavior of a structural component. Monitoring the structural response in terms of stress and moment can for example be used for estimating accumulated fatigue damage of the structural component, or as input to the components control system, in terms of reducing moment and stress. By definition of the differential equation for a beam given in 3.2, the bending moment can be calculated as $M_b = -EI^e \frac{d^2 v(x)}{dx^2}$. As it is only the transversal v, and rotational θ nodes which contribute to the bending moment, the bending moment anywhere along an element can be approximated by writing $\frac{d^2 v(x)}{dx^2}$ as

$$\frac{d^2 u}{dx^2} = \frac{1}{l^e} \frac{d^2 \mathbf{N^e}}{d\xi^2} \mathbf{d^e} = \frac{1}{l^e} \begin{bmatrix} 0 & \frac{6\xi}{l^e} & 3\xi - 1 & 0 & -\frac{6\xi}{l^e} & 3\xi + 1 \end{bmatrix} \begin{bmatrix} a_1 \\ v_1 \\ \theta_1 \\ a_2 \\ v_2 \\ \theta_2 \end{bmatrix}, \tag{3.44}$$

and multiplying it with the young's modulus E and the elemental moment of inertia I^e. Stress calculations will include the effect of axial loading, and the general term for total elemental stress becomes

$$\sigma^e(x) = E\frac{(a_2 - a_1)}{l^e} + \frac{M_b(x)}{I^e}y, \tag{3.45}$$

where y is the distance from the neutral axis.

3.7 Enviromental Loadings

An OWT is exposed to a large variation of environmental forces throughout its lifetime. Modeling the true forces, and the response of the turbine is a highly complex task, making reliable design very difficult. Due to the complexity and coupling of many of the loading scenarios, not all of these forces can be modeled for this 2D model. For this simplified model, some of the most dominant forces will be modeled and can be summarized as;

- Wind Loads
- Wave Loads
- Rotor-tower interaction (3P loading)
- Gravitational loads from nacelle weight
- Water current

Other environmental forces which can be of importance when modeling the response of the turbine are

- Centrifugal forces from the rotating blades
- Torsional moments on turbine tower from uneven loading on the blades
- Loading from imperfections in weight of the blades, or different pitching of the blades. (1P loading)
- 2^{nd} order wave loads

The above mentioned loads are typically accounted for when simulating in advanced simulation programs, such as *SIMO/Riflex-Aerodyn* or *FAST*. In addition there are other important factors which needs to be considered if attempting to get a better understanding of all possible scenarios an OWT is subjected to. Some of these effects can be summarized as;

- Scouring
- Marine growth
- Soil-structure interaction
- Corrosion
- Sea ice and icing on turbine blades.

For further reading on different environmental loadings acting on a wind turbine, the reader is referred to Arany, Bhattacharya, Macdonald, and Hogan (2014) and Hansen (2013).

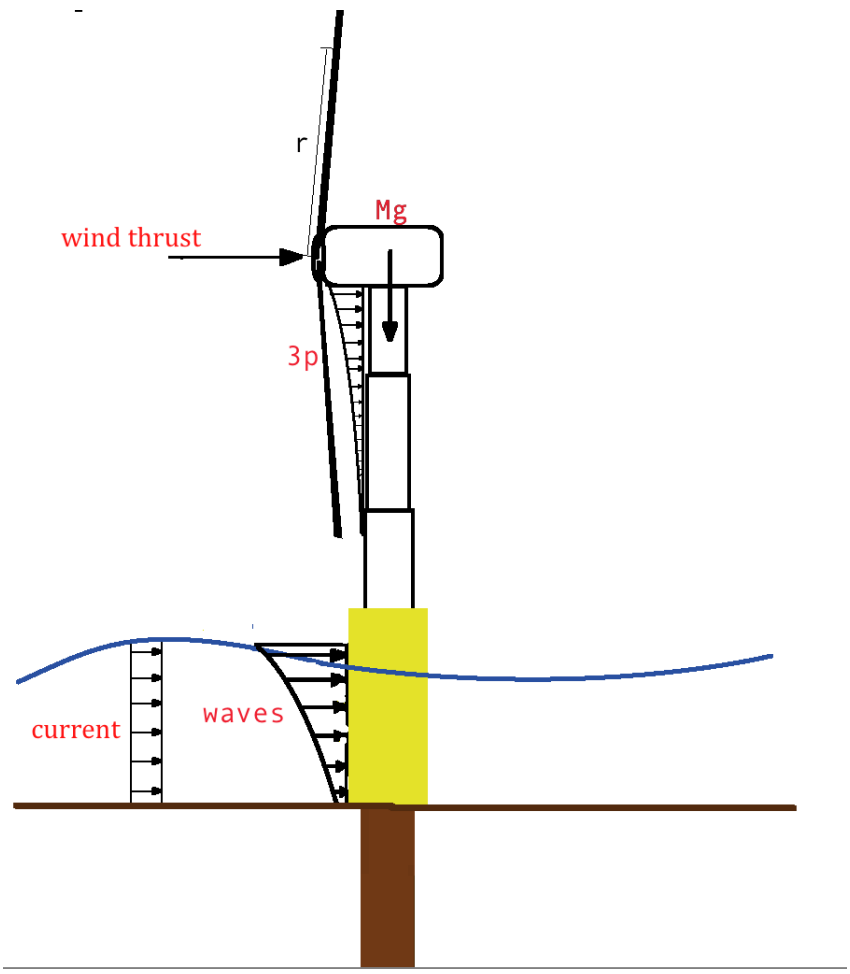

Figure 3.9: The modeled environmental loadings from wind thrust, wave loads, water current, 3P loads and nacelle weight

3.7.1 Wind loads

This section will model the effective wind load acting on the turbine tower from the wind loads transferred from the turbine blades to the rotor and to the tower. The considered model is assuming an ideal wind turbine where the thrust force is calculated with respect to conservation of momentum. The specific dynamics on how the wind causes loads on the turbine blades is well explained in Hansen (2013). Using quasi steady assumptions the thrust force on the rotor for a specific wind speed can be given by

$$\tau_w = \frac{1}{2}\rho_a \frac{\pi D_b^4}{4} C_T(\bar{U} + u(t))^2, \tag{3.46}$$

where D_b is the diameter of the swept rotor blades, ρ_a is the density of air, $\bar{U}$ is the mean wind speed, u is a fluctuating wind speed (turbulence) component. C_T is the aerodynamic thrust coefficient which depends on the pitched angles of the blades, rotational speed of the rotor and wind speed. A widely used method to calculate C_T is through blade element momentum (BEM) theory. The BEM method is based on the assumption that each turbine blade can be divided into a finite number of blade elements, where the load on each element is calculated using an iterative algorithm, and the total load is obtained by summing up the contribution from each element. Details behind the BEM method can be found in e.g. Hansen (2013). As it is an expression for the resulting thrust force on the tower structure which is of interest, the modeled wind thrust force will be assumed using a constant thrust coefficient which can be modeled as

$$C_T = \frac{3.5 \cdot \left(2\bar{U} - 3.5\right)}{\bar{U}^2} \approx \frac{7}{\bar{U}}. \tag{3.47}$$

This approximation was presented in Frohboese, Schmuck, and Hassan (2010) and showed to provide conservative and relatively accurate results for most offshore wind turbine's in the important wind speed range. Writing out the expression for the wind speed and assuming that the magnitude of $u(t)^2$ is small and can be neglected. The total wind load is then composed of a static force and a time varying dynamic force

$$\tau_w = \frac{1}{2}\rho_a \frac{\pi D_b^2}{4} C_T(\bar{U}^2 + 2\bar{U}u(t) + u^2(t)) \approx \underbrace{\frac{1}{2}\rho_a \frac{\pi D_b^2}{4} C_T \bar{U}^2}_{\tau_{\bar{U}}} + \underbrace{\rho_a \frac{\pi D_b^2}{4} C_T \bar{U} u(t)}_{\tau_{gust}}. \tag{3.48}$$

This thrust force expression will later (section 3.8) be modified to account for the relative velocity between the tower top and and the effective wind speed.
The height dependent average wind speed $\bar{U}(z)$ is scaled using the wind profile power law, given by

$$\bar{U}(z) = \bar{U}_r\left(\frac{z}{z_r}\right)^{\mu}, \tag{3.49}$$

where the wind speed at height z is given relative to a mean wind speed at a reference height z_r. According to Arany et al. (2014) a scaling parameter valid for offshore wind applications can be set to $\mu = 0.27$.

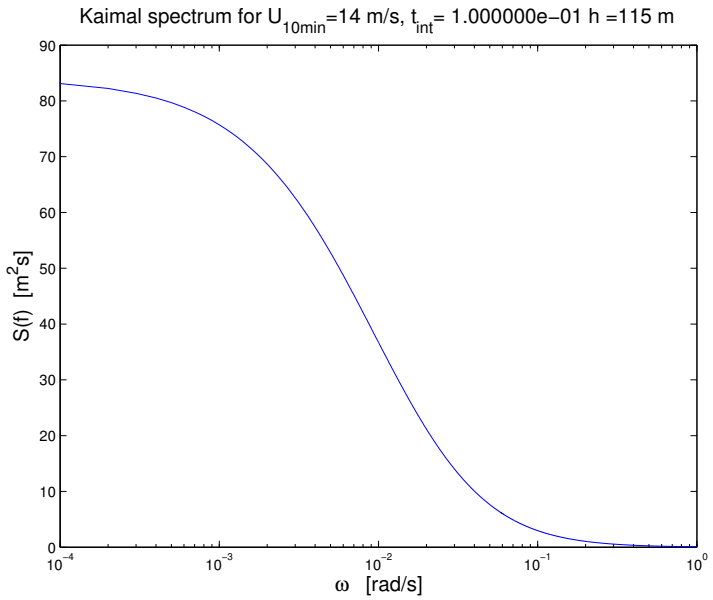

Figure 3.10: Kaimal spectral density plot for $\frac{\sigma}{\bar{U}} = 0.10$, $\bar{U} = 14[m/s]$

The fluctuating wind speed $u(t)$ is obtained from a realization of the spectral density for the fixed point $Kaimal\ Spectrum$, given as

$$S_{kk}(\omega) = \frac{\frac{\sigma^2}{\bar{U}} l}{(1 + \frac{3\pi l}{\bar{U}})^{\frac{5}{3}}}, \tag{3.50}$$

where σ is the standard deviation in wind speed, l is a length scale depending on the height above ground. For $h < 30$ [m] $l = 20h$. For $h > 30$ [m] $l = 600$ [m] (Hansen, 2013).
The fraction $\frac{\sigma^2}{\bar{U}}$ is given as the turbulence intensity, and vary with the mean wind speed, site location and surface roughness. The turbulence intensity will also be modified due to presence of the turbine.
As the wind spectrum is valid for one point in space, it will be necessary to formulate coherence functions for simulating wind at several points in space. It will for simplicity be assumed that the wind blowing through the rotor disc can be represented at one point, such that (3.50) is valid. A discrete realization of the Kaimal specter shown in Figure 3.10 can be obtained by using the inverse discrete Fourier transform (DFT),

$$u(t) = \bar{U} + \sum_{i=1}^{N/2} \sqrt{\frac{2S_{kk}(\omega_i)}{T} cos(\omega_i t - \phi_i)}, \tag{3.51}$$

where N is the number of samples and $T = \Delta t N$ is the total simulation time. Δt represents the time step between to measurements. ϕ_i represents a random phase angle between 0 and 2π.

The correct expression for an elemental load vector is obtained by using (3.15). However, since the wind load is applied as a point load at the top node in horizontal direction, the load expression simplifies to

$$\tau_w^e = \int_{-1}^{1} \mathbf{N}^{eT} \tau_w(\xi) \frac{1}{2} l^e d\xi = \mathbf{N}^{eT}(\xi) p_N \frac{1}{2} l^e \Big|^{\xi=1} = \frac{1}{2} l^e \begin{bmatrix} 0 \\ 0 \\ 0 \\ 0 \\ 1 \\ 0 \end{bmatrix} (\tau_{stat} + \tau(t)_{gust}). \tag{3.52}$$

3.7.2 Wave Loads

Wave loads are an important contribution to the loading specter for an OWT. Cyclic loading behavior and sea states with energy close to an OWT's lowest natural frequency, can make wave loadings important with respect to fatigue damage. It is therefore one of the main design drivers to avoid natural frequencies of the structure to lie in a region where there can be wave components with significant energy. The considered wave loads will consist of linear first order wave loads, modeled through Morison's equation. An infinitesimal horizontal force component on the turbine can be written as,

$$dF = \pi \rho_w \frac{D^2}{4} C_m a_1 + \frac{\rho}{2} C_{dw} |u_1| u_1 dz, \tag{3.53}$$

where D is the diameter of the water covered part of the structure. C_m is the mass coefficient representing the contribution from mass and added mass of the cylinder. Potential flow will be assumed hence $C_m = 2$ (Faltinsen, 1993). C_{dw} is the drag coefficient, a_1 and u_1 is the horizontal fluid particle acceleration and velocity respectively. ρ_w is the fluid density. The fluid acceleration and velocity will be derived through potential theory, where the velocity potential for a linear 1^{st} order wave component on finite water depth is written as,

$$\phi_i = \frac{g\, \xi_{Ai}}{\omega_i} \frac{cosh\ k_i(z+h)}{cosh\ k_i h} cos(\omega_i t - k_i x + \phi_i). \tag{3.54}$$

Here h is the water depth, z is the depth variable, ω_i is circular frequency of the wave component. ϕ_i is a random phase angle between 0 and 2π. k_i is the wave number, which can be found through iteration from the relation,

$$\frac{\omega_i^2}{g} = k_i\ tanh\ k_i h, \tag{3.55}$$

with g as the gravitational acceleration. Setting $x = 0$, the horizontal fluid velocity u_i, for wave component i is given as,

$$u_i = \frac{d\phi_i}{dx} = \omega_i \xi_{Ai} \frac{cosh\ k_i(z+h)}{sinh\ k_i h} sin(\omega_i t + \phi_i), \tag{3.56}$$

and horizontal fluid acceleration a_i,

$$a_i = \frac{d^2\phi_i}{dx\,dt} = \omega_i^2 \xi_{Ai} \frac{cosh\ k_i(z+h)}{sinh\ k_i h} cos(\omega_i t + \phi_i). \tag{3.57}$$

A given sea state is assumed to be consisting og N linear harmonic wave components. The energy pr. unit area for a wave component i can be written as,

$$E_i = \frac{1}{2}\rho_w g \xi_{Ai}^2. \tag{3.58}$$

As ρ_w and g are constants, $\frac{1}{2}\xi_{Ai}^2$ will be a measure for the amount of energy. The total amount of energy for the given sea state will be the sum of all N wave components,

$$\frac{E}{\rho_w g} = \sum_{i=1}^{N} \frac{1}{2}\xi_{Ai}^2(w_i), \tag{3.59}$$

where $\xi_{Ai}(w_i)$ is the wave amplitude for a wave component with frequency w_i. Using the energy specter for the surface elevation for a given sea state $S(\omega)$, one can then assume the energy within a small frequency interval Δw equals the energy of all wave components within this interval, such that,

$$\frac{1}{2}\xi_{Ai}^2 = S(\omega_i)\Delta\omega_i. \tag{3.60}$$

From this, one can express the wave amplitude for a wave component with frequency ω_i as,

$$\xi_{Ai} = \sqrt{2S(\omega_i)\Delta\omega_i}. \tag{3.61}$$

Having all the necessary quantities derived from a wave specter e.g. the JONSWAP specter, the total wave loading force on the structure will be the sum of all wave components integrated over the water covered part of the structure.

$$f(z,x,t)_{waves} = \sum_{i=1}^{N} \int_{-h}^{0} \pi\rho \frac{D^2}{4} C_m a_i + \frac{\rho}{2} C_{dw} |u_i| u_i dz. \tag{3.62}$$

The force term in (3.62) can be simplified by determining the dominant force term. The Keulegan Carpenter (KC) number, can be used as a measure of the ratio between drag and inertia forces. The KC number can be given as,

$$KC = \frac{u_{max} T}{D}, \tag{3.63}$$

where $T = \frac{\omega_i}{2\pi}$ is the period of the wave component i, D is the significant length, which for the turbine foundation is the diameter. In the design of the foundation it is assumed that the foundation diameter is constant at $D = 7$ m. u_{max} is the maximum horizontal fluid velocity. For KC $\leq \approx 5$ the loading is said to be inertia dominated, and drag forces can be neglected (Faltinsen, 1993). Figure 3.11 shows the KC number at the water surface ($z = 0$) for a sea state with significant wave height $H_{m0} = 7$ m and peak period $T_p = 11$ sec. From the figure it can be observed

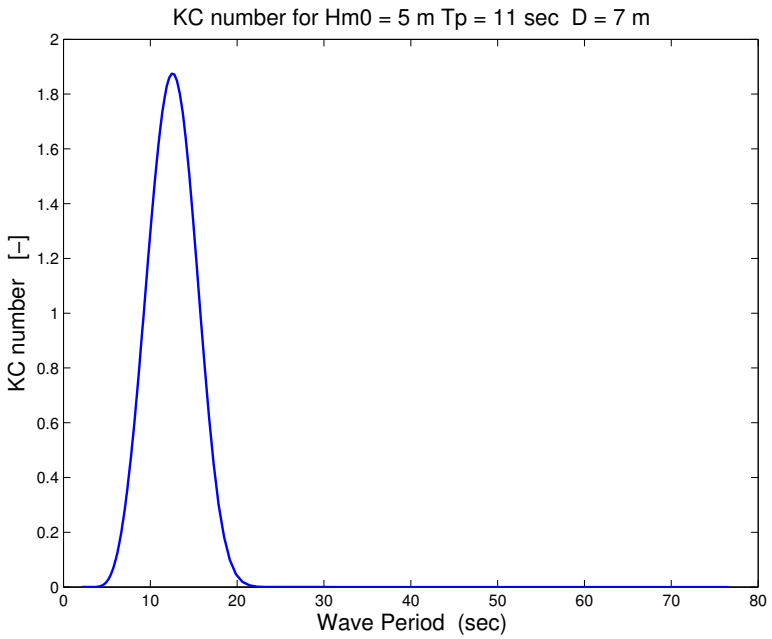

Figure 3.11: Keuglegan Carpenter number at sea surface for varying wave periods

that the KC number never approaches the limit $KC \approx 5$. The same results yields for other sea states which will be simulated. The drag forces will be therefore be neglected when modeling wave loads.

To transform the wave loads to elemental forces, acting at its corresponding nodes, the wave loads over each element length will be assumed evenly distributed, with a depth coordinate equal to the depth at the midpoint of each element. Figure 3.12 shows an illustration of this approximation. Using the result of (3.16), the resulting elemental force contribution will be written as,

$$\tau^e_{waves}(z^e,t) = \frac{1}{2} l^e \begin{bmatrix} 0 \\ 1 \\ \frac{1}{6} l^e \\ 0 \\ 1 \\ -\frac{1}{6} l^e \end{bmatrix} \sum_{i=1}^{N} C(\omega_i) \xi_{Ai} \cos(\omega_i t + \phi_i). \tag{3.64}$$

where $C_i(\omega_i)$ is given by,

$$C(\omega_i) = \pi \rho_w \frac{D^2}{4} C_m \frac{cosh\ k_i(z^e + h)}{sinh\ k_i h} \omega_i^2. \tag{3.65}$$

The coordinate z^e is the water depth at the middle of the current calculated element.

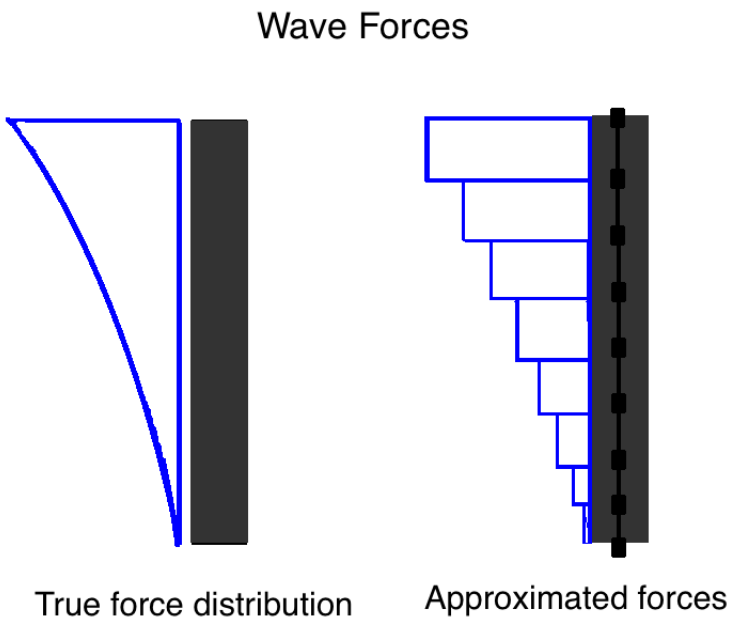

Figure 3.12: Approximation of wave forces being modeled

3.7.3 Rotor-Tower Interaction

The rotation of the turbine blades on the turbine induce harmonically varying loading patterns with frequency of loading equal to a multiple of the turbine rotor's rotational frequency. These loading patterns are known as, $1P$, $3P$, $6P$, $9P$ and so on. Where the number tells the frequency of loading.. The $1P$ and $3P$ loading patterns can be considered of most importance as, they lie closer to fundamental frequencies of the turbine, than the higher frequent loading patterns. This thesis will focus on the 3P loading pattern. The reader is referred to Arany et al. (2014) for more information on rotor-tower interaction loads.

3P Loading

As the wind flows past the turbine tower it will induce a drag force on the structure. By neglecting vortex induced vibrations the drag force experienced by the tower can be written as,

$$\tau_{drag}(t) = \frac{1}{2}\rho_a C_{da} \frac{\pi(D(z))^2}{4}(U(z,t))^2, \tag{3.66}$$

where $D(z)$ is the diameter of the structure at height z, C_{da} is the drag coefficient and $U(z,t)$ is the total wind speed at height z.

Every time a blade passes in front of the tower it will disturb the wind flow on the tower, resulting in a decrease of the drag force $\tau_{drag}(t)$ on the tower. The frequency of this oscillatory loading will be 3 times the rotational frequency of the rotor. To model this load cycle it is assumed that the drag force on the tower will act over a length equal to the blade radius R_b. Three assumptions will be made regarding the modeled drag force on the tower.

1. Constant drag force over tower height and wind velocity.

2. The wind gust will be modeled as an exponentially decaying function with respect to height z.

3. The drag force on the tower drops to zero whenever a blade is in front of the tower, and at a maximum whenever no blade is in front.

The drag coefficient is highly dependent on the flow velocity, and should for refined simulations include the effect of a velocity dependent drag coefficient. For the following simulation purposes it is assumed that a constant drag coefficient is valid. To simulate the time history of wind speed for multiple points in space, the time history of the points are not independent, but affected by generation of vortices. For a wind simulation considering the wind realization at different heights z, a coherence function should be used to calculate cross spectral density of the different points along the turbine tower. To avoid this complexity, an exponentially decaying effect of wind gust in the wind speed realization given in (3.51) is used. As it is of primary interest to show the fundamental effect of the rotor-tower interaction a fully correct expression for the wind realization is assumed to be of lesser importance.

The total wind speed is assumed constant over each element length and given by,

$$u_{3P}(z,t) = \bar{U}(z) + e^{-0.01n} \sum_{i=1}^{N/2} \sqrt{\frac{2S_{kk}(\omega_i)}{T} cos(\omega_i t - \phi_i)}, \tag{3.67}$$

where the height dependent average wind speed $\bar{U}(z)$ is calculated by the wind power law given in (3.49). The variable n in the exponent is giving the number of the elements which the wind speed is calculated over. n spans the range given by,

$$n = \left[0, 1...p-1\right],$$

where p is the total number of elements which the $3P$ load is acting over. The amplitude of the total drag force on the tower can be written as,

$$|\tau_{3P}(z,t)| = \int_{(H-R_b)}^{H} \underbrace{\frac{1}{2}\rho_{air} C_{da} D(z) u_{3P}^2(z,t)}_{\tau_{drag}} dz. \tag{3.68}$$

The integration limit H represent the tower height and R_b the radius of the turbine blade. The drag coefficient is assumed to be $C_{da} = 0.8$. The drag force on the tower will oscillate between zero whenever a turbine blade is in downright position, and maximum of $|\tau_{3P}|$ when no blade is in downright position. To model this, a impulse train equal to 3 times the rotational frequency is used.
As with the wave loads, a discretization of the continuous $3P$ load is necessary, before applying it to the FE model. The drag force is assumed evenly distributed over each element length, such that the elemental drag force on the tower structure can be written as,

$$\tau_{3P}^e(z,t) = \int_{nl^e}^{(n-1)l^e} \tau_{3P}(z,t)\mathbf{N}^{eT} dx = \frac{1}{2} l^e \tau_{3P}(z,t) \begin{bmatrix} 0 \\ 1 \\ \frac{1}{6}l^e \\ 0 \\ 1 \\ -\frac{1}{6}l^e \end{bmatrix} \delta(t). \tag{3.69}$$

The impulse function $\delta(t)$ can be expressed as,

$$\delta(t) = \begin{cases} 0 & \frac{3\omega_r t}{60} = \mathbb{N} \\ 1 & otherwise \end{cases}$$

where $\mathbb{N} \in [1,2,3...)$. This gives that whenever $\frac{3\omega_r t}{60}$ equals a positive integer, a blade is passing by the tower, and the $3P$ force drops to zero.

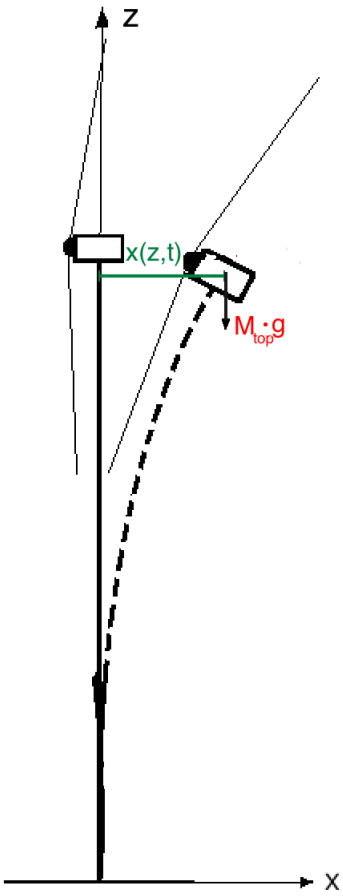

Figure 3.13: Displacement of tower top induces a bending moment on the structure

Tower Top Weight

The modeled tower top weight M_{top} is consisting of weight from nacelle and turbine blades. Values for the total tower top weight can be found in Appendix C. The static load is added as a compressive axial force acting through the top node. It is for simplicity assumed that the top mass is a point mass. Horizontal displacement of the tower will induce a bending moment on the structure. The top element load vector will then be written as,

$$\tau^e_{top}(t) = M_{top} \cdot g \begin{bmatrix} 0 \\ 0 \\ 0 \\ -1 \\ 0 \\ x(H,t) \end{bmatrix}, \tag{3.70}$$

where $x(z,t)$ is the time dependent horizontal tower displacement at tower top height H.

3.7.4 Water Current

The effect of water current on the structure will be modeled as an evenly distributed force acting over the water covered foundation section in the FE model. The effect of water current is not the most profound of the forces acting on a bottom fixed wind turbine, it should however be added to the total load pattern. Assuming a constant water current velocity, the drag coefficient will stay constant, and by neglecting any vortex generation, the total current drag force across an element transformed to nodal loads can be written as,

$$\tau_c^e = \int_{-1}^{1} \frac{1}{2} C_{dw} \rho_a \pi \frac{D^2}{4} V_c^2 \mathbf{N}^{eT} \frac{l^e}{2} d\xi = \frac{l^e}{4} C_{dw} \rho_a \pi \frac{D^2(z)}{4} V_c^2 \begin{bmatrix} 0 \\ 1 \\ \frac{1}{6} l^e \\ 0 \\ 1 \\ -\frac{1}{6} l^e \end{bmatrix}, \tag{3.71}$$

where V_c is the water current velocity and C_{dw} is the drag force coefficient. D is the structure diameter below sea surface.

3.8 Damping Effects

Close to a natural frequency of the structure, dynamic amplification increases the response of the structure. The magnitude of response is limited by the damping in the structure. There are many contribution to damping on an OWT, and are in some extent due to structural, hydrodynamic and soil interaction. The most important damping of the structure comes from the aerodynamic damping.

3.8.1 Aerodynamic Damping

The varying thrust force on the wind turbine from the wind, cause the turbine to sway back and forth. Figure 3.14 shows that as the turbine top moves towards the wind, the turbine blades will experience an increase in wind speed, totaling to V_T. This increase in experienced wind speed will then increase the aerodynamic thrust force on the turbine. The increase in thrust force will counteract the the tower top motion. When the turbine top moves in the same direction as the incoming wind, the experienced wind speed of the blades will be lower than nominal velocity, and the resulting thrust force will decrease, counteracting the motion. As the effect of blade dynamics is not included in the model, a simplified approach to include aerodynamic damping will be included. For a fully modeled wind turbine, the relative velocity between the tower and the wind will change the experienced velocity of the turbine blades. This will again change the angle of attack for the blades, and the thrust coefficient determining the thrust force. The effect of aerodynamic damping is added to the model by including the relative velocity between the wind and tower top when calculating thrust force given in (3.46). The new expression for the thrust force will by written as,

$$\tau_w = \frac{1}{2} \rho_a \frac{\pi D_b^4}{4} C_T (\bar{U} + u(t) - \dot{x}(H))^2, \tag{3.72}$$

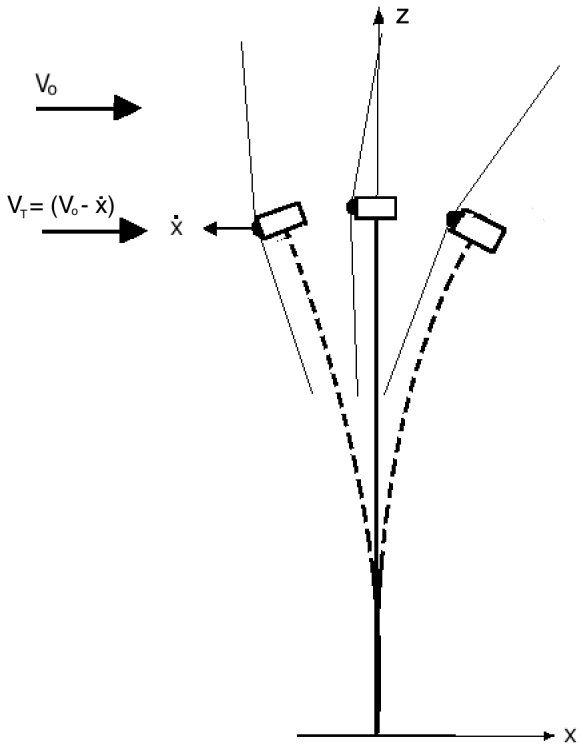

Figure 3.14: Nacelle motion changes the experienced wind speed for the wind turbine, contributing to aerodynamic damping.

where $\dot{x}(H)$ is the horizontal velocity of the tower top. Writing out the expression for the squared of the relative velocity,

$$(\bar{U} + u(t) - \dot{x}(H))^2 = \bar{U}^2 + 2\bar{U}(u(t) - \dot{x}(H)) - 2\dot{x}(H)u(t) + u(t)^2 + \dot{x}(H)^2, \tag{3.73}$$

and assuming that both tower top velocity and fluctuating wind velocity component is low. The effective wind velocity can be simplified to

$$(\bar{U} + u(t) - \dot{x}(H))^2 \approx \bar{U}^2 + 2\bar{U}(u(t) - \dot{x}(H)), \tag{3.74}$$

giving the effective wind thrust force as,

$$\tau_w = \frac{1}{2}\rho_a \frac{\pi D_b^4}{4} C_T(\bar{U}^2 + 2\bar{U}(u(t) - \dot{x}(H))). \tag{3.75}$$

3.8.2 Hydrodynamic Damping

Hydrodynamic damping essentially consists of two terms, radiation damping and viscous drag damping. The radiation damping is accounted for by the relative velocities between the waves and the structure in the drag force term of Morison's equation given in (3.53). An analysis performed by Damgaard, Andersen, Ibsen, and Andersen (2012) suggested that the radiation damping effect of a 4.7 [m] diameter monopile structure, was estimated to 0.13% of critical damping for the first bending mode. In Figure 3.15 one can observe the velocity of the structure subjected to wind and wave condition with significant wave height $H_{m0} = 5$ [m], peak period $T_p = 11$ [sec] and mean wind speed $\bar{U} = 11$ [m/s] . As the figure shows, the effective velocity of the water covered part of the structure is quite low, such that the effect of damping included if not neglecting the drag force term in Morison's equation is assumed negligible.
The viscous damping effect results from the square of the relative velocity between structure and fluid flow. According to Damgaard et al. (2012) and Tarp-Johansen et al. (2009) the effect of viscous damping on a OWT monopile structure is negligible and can be neglected. The statement of still neglecting the drag term in Morison's equation and thus hydrodynamic damping therefore seems valid.

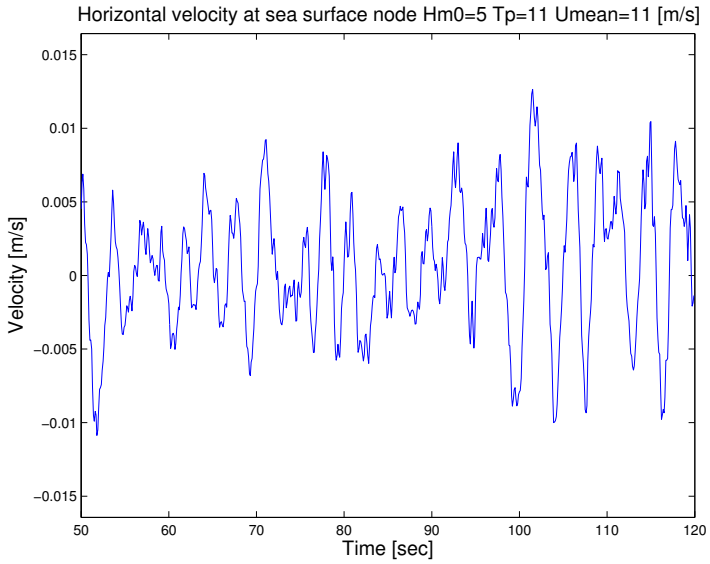

Figure 3.15: Translational velocity of structure foundation subjected to waves ($H_{m0} = 5$ [m], $T_p = 11$ [sec] and mean wind speed $\bar{U} = 11$ [m/s])

3.8.3 Structural Damping

Material damping of steel from internal friction is considered in the range 0.2% – 0.3% of critical damping. These are general values, common in the literature, and amongst other stated in (M.F Cook, 1982). From the reference turbine design guide for the DTU 10MW turbine given in Bak et al. (2014), it is advised to set the damping ratio $\xi = 0.1\%$ of critical damping for all eigenmodes.

3.8.4 Soil Damping

Damping effect on the wind turbine system due to there interaction between the soil and turbine monopile. The contribution can be of a significant size and (Arany et al., 2014) suggests the soil damping to lie in the region $0.5\% - 1.5\%$ of critical damping. However there are large uncertainties in this contribution due to the large differences between theoretical solutions and measurements (Lloyd, 2005). All though having uncertainties, a linear damping term consisting of a damping ratio $\xi = 0.05$ for all bending modes will be added to the the structure.

3.8.5 Damping Model

Assuming a linear damping model, modeled as *Rayleigh damping*, the total damping contribution from soil damping ξ_{soil} and structural damping ξ_{str} can be computed by a total damping ratio,

$$\xi = \xi_{soil} + \xi_{str}. \tag{3.76}$$

The damping matrix is computed as proportional to the system's mass and stiffness matrices and given by,

$$\mathbf{D_d} = \alpha\mathbf{M} + \beta\mathbf{K}, \tag{3.77}$$

where α and β is to be selected. Solving the generalized eigenvalue-problem given by,

$$\mathbf{M}^{-1}\mathbf{K}\Psi = \Omega^2\mathbf{V}, \tag{3.78}$$

where the columns of $\mathbf{V} = \begin{bmatrix} v_1 & v_2 & \dots & v_n \end{bmatrix}$ represents the eigenvectors of the undamped system and Ω is a diagonal matrix containing the natural frequencies ω_i. One can through mass normalizing the eigenvectors as,

$$\hat{v}_i = \frac{v_i}{\sqrt{v_i^T\mathbf{M}v_i}}, \tag{3.79}$$

and utilizing the orthogonality condition of the eigenvectors, rewrite the damping matrix $\mathbf{D_d}$ as,

$$\hat{\mathbf{V}}^T\mathbf{D}_d\hat{\mathbf{V}} = \begin{bmatrix} 2\xi_1\omega_1 & & \\ & \ddots & \\ & & 2\xi_N\omega_N \end{bmatrix} = \alpha \begin{bmatrix} 1 & & \\ & \ddots & \\ & & 1 \end{bmatrix} + \beta \begin{bmatrix} \omega_1^2 & & \\ & \ddots & \\ & & \omega_N^2 \end{bmatrix}. \tag{3.80}$$

The damping coefficients α and β are then determined by solving the following set of equations for two different frequencies,

$$\xi_i = \frac{\alpha}{2}\frac{1}{\omega_i} + \frac{\beta}{2}\omega_i, \tag{3.81}$$

$$\xi_j = \frac{\alpha}{2}\frac{1}{\omega_j} + \frac{\beta}{2}\omega_j, \tag{3.82}$$

which gives,

$$\alpha = \frac{2\left(\xi_j \omega_i^2 \omega_j^2 - \xi_j \omega_i \omega_j^2\right)}{\omega_i^2 - \omega_j^2}, \tag{3.83}$$

$$\beta = \frac{2\left(\xi_i \omega_i - \xi_j \omega_j\right)}{\omega_i^2 - \omega_j^2}. \tag{3.84}$$

Using the two lowest natural frequencies of the structure $\omega_{n1} = 0.23[Hz]$ and $\omega_{n2} = 1.34[Hz]$ and the damping coefficient $\xi_1 = \xi_2 = 0.015$ gives the damping coefficients $\alpha \approx 0.347$ and $\beta \approx 0.031$. A plot of (3.82) shown in Figure 3.16 depicts that the contribution to damping is highly dominated by the α value, i.e. mass dominated for low natural frequencies. At higher frequencies, the β value, proportional to the stiffness becomes increasingly dominant.

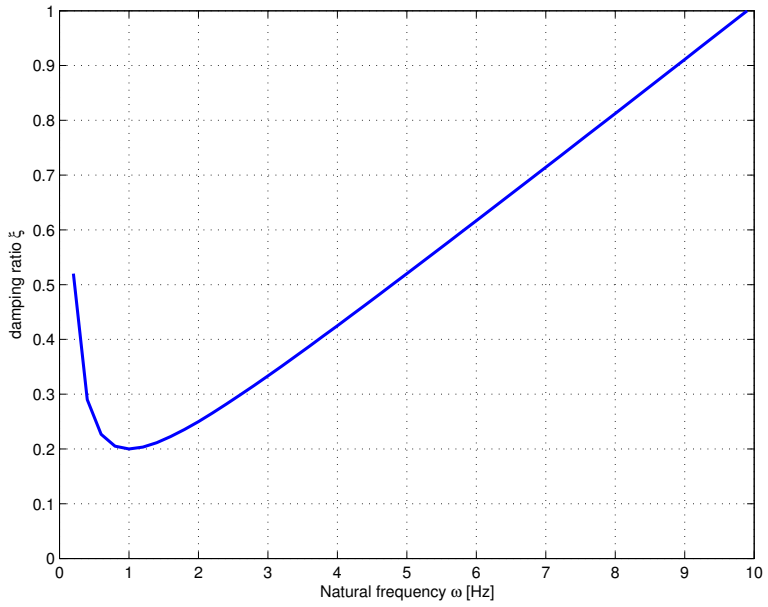

Figure 3.16: Typical variation of damping ratio with natural frequency for a system

3.9 Model Assembly

Figure 3.17 show the modeled structure. It is divided into three sections, monopile, foundation and tower. Material properties for the various sections can be found in Appendix A. The weight of tower top nacelle, blades etc is modeled as a point mass which is added to the end node. It is assumed that the model end is clamped, restraining any displacement or rotation at the fixed end. For simulation studies, the model will be represented on state space form.

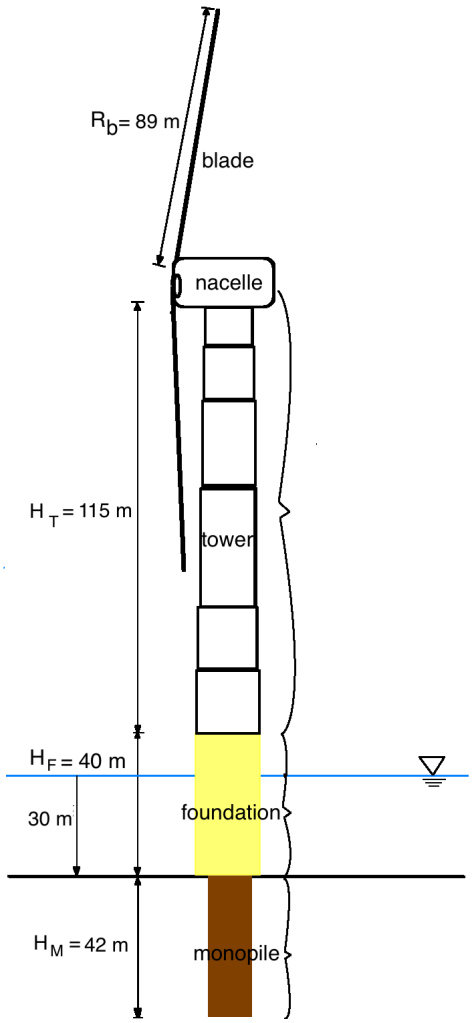

Figure 3.17: Wind turbine model divided into three sections, *monopile*, *foundation* and *tower*.

3.9.1 State Space Representation

The total assembled plant model with environmental disturbances can by Newton's second law of motion be given by,

$$\mathbf{M}\ddot{q} + \mathbf{D_d}\dot{q} + \mathbf{K}q = \tau_{waves} + \tau_{3P} + \tau_{top} + \tau_{\bar{U}} + \tau_{gust}, \tag{3.85}$$

where $\mathbf{M}, \mathbf{D_d}, \mathbf{K}$ are the mass, damping and stiffness matrices respectively. The different τ are the environmental disturbances from waves, wind and tower interaction. The total force input vector can be represented by a total input vector $\tau(t) \in \mathbb{R}^{n_p}$ and rewritten as,

$$\mathbf{M}\ddot{q} + \mathbf{D_d}\dot{q} + \mathbf{K}q = \mathbf{b}\tau(t), \tag{3.86}$$

where $\mathbf{b} \in \mathbb{R}^{n \times n_p}$ relates the different inputs from $\tau(t)$ to its corresponding node. By the assumption of linear behavior, the $n-dimensional\ 2^{nd}$ order system can be represented on first order state space form as,

$$\dot{\mathbf{q}} = \mathbf{A}\mathbf{q} + \mathbf{G}\tau(t), \tag{3.87}$$

$$\mathbf{y} = \mathbf{C}\mathbf{q} + \mathbf{J}\tau(t) + v(t). \tag{3.88}$$

Where the matrices $\mathbf{A} \in \mathbb{R}^{2n \times 2n}$ and $\mathbf{G} \in \mathbb{R}^{2n \times n_p}$ are given by

$$\mathbf{A} = \begin{bmatrix} \mathbf{0}_{n\times n} & \mathbf{I}_{n\times n} \\ -\mathbf{M}^{-1}\mathbf{K} & -\mathbf{M}^{-1}\mathbf{D_d} \end{bmatrix}, \quad \mathbf{G} = \begin{bmatrix} \mathbf{0}_{n\times q} \\ \mathbf{M}^{-1}\mathbf{b} \end{bmatrix},$$

and state vector $\mathbf{q}$ represented as,

$$\mathbf{q} = \begin{bmatrix} q \\ \dot{q} \end{bmatrix}. \tag{3.89}$$

$v(t) \in \mathbb{R}^{2n \times 1}$ represents continuous zero-mean white noise, with covariance

$$v(t) \sim N(0, \mathbf{R}) \tag{3.90}$$

$\mathbf{R} = \mathbb{E}\left[v_k v_k^T\right] > 0$ represents the white noise covariance matrix. For velocity or displacements measurements, the output matrix $\mathbf{C} \in \mathbb{R}^{2n \times 2n}$ will have the following structure, respectively,

$$\mathbf{C} = [\mathbf{0}_{m\times n} \quad \mathbf{c}],$$

$$\mathbf{C} = [\mathbf{c} \quad \mathbf{0}_{m\times n}],$$

with a feedthrough matrix $\mathbf{J} \in \mathbb{R}^{n_y \times n_p}$ equal to the zero matrix. $\mathbf{c} \in \mathbb{R}^{n_y \times 2n}$ gives the position of the measured nodes. Using accelerations measurements, gives the following output matrix,

$$\mathbf{C} = [-\mathbf{c}\mathbf{M}^{-1}\mathbf{K} \quad -\mathbf{c}\mathbf{M}^{-1}\mathbf{D_d}],$$

and feedthrough matrix on the form,

$$\mathbf{J} = \left[\mathbf{c}\mathbf{M}^{-1}\mathbf{b}\right]. \tag{3.91}$$

By inspecting the eigenvalues of the total assembled system the first four natural frequencies of the model was found as given in Table 3.1. In the frequency response plot shown in 3.18 one can see the spikes represents the first four natural frequencies of the system. From the figure it is clearly visible that it is the first bending mode which dominant the response of the structure, where the succesive modes have a smaller and smaller impact on the response.

	$1^{st} mode$	$2^{nd} mode$	$3^{rd} mode$	$4^{th} mode$
$f_n[Hz]$	0.23	1.34	3.86	6.86
$T_n[s]$	4.37	0.74	0.26	0.15

Table 3.1: Natural frequencies and periods of the first four bending modes

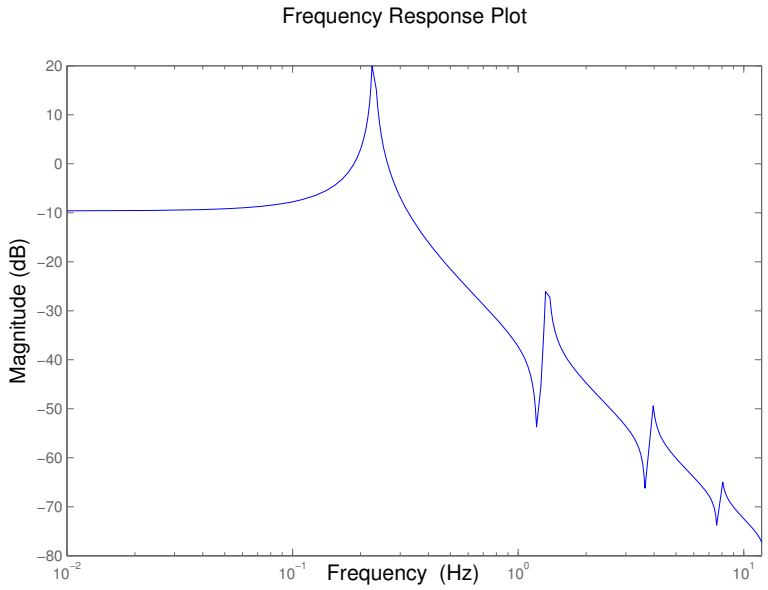

Figure 3.18: Frequency Response plot for the fully assembled model

Figure 3.19 gives an illustration of the frequency of loading from the different loading scenarios that the modeled structure can be subjected to. The figure also shows the location of the first and second bending mode of the structure. As can be seen, the first bending mode is located at a position which in case of modeling errors easily can fall into the regime of one of the loading conditions depicted in the figure. As the design of wind turbines turbines are getting larger and larger, it is seen as a possibility that the 2^{nd} bending mode of the structure can decrease, closing into the regime of the 3P loading cycles. This can be an important aspect to consider for future turbines.

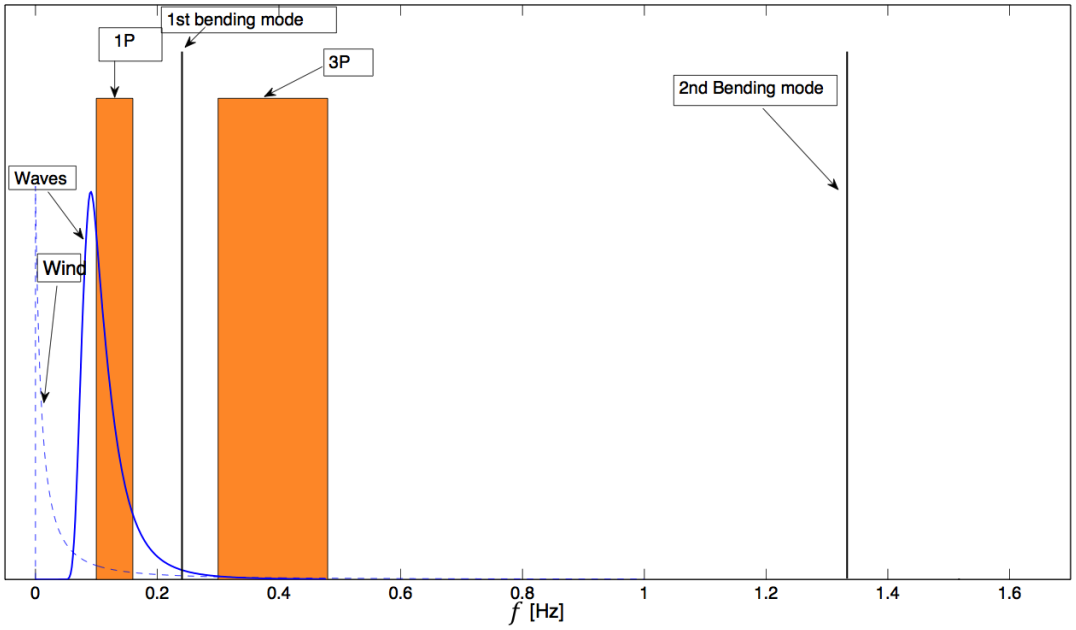

Figure 3.19: Frequencies of interest for the modeled wind turbine

3.9.2 Modal Representation

As shown in the frequency response plot given in Figure 3.18, the dominant response of the model constitutes from the first eigenmode of the system. To exploit this fact and reduce computational time, the governing system can be represented on modal form by introducing a coordinate transformation,

$$q(t) = \hat{\mathbf{V}}u(t), \tag{3.92}$$

where $\hat{\mathbf{V}}$ are the set of mass normalized eigenvectors obtained by solving the generalized eigenvalue problem given in (3.78) and $u(t)$ are the so-called modal displacements. Introducing the coordinate transformation to (3.86) and premultiplying with $\hat{\mathbf{V}}^T$ one obtains,

$$\hat{\mathbf{V}}^T\mathbf{M}\hat{\mathbf{V}}\ddot{u}(t) + \hat{\mathbf{V}}^T\mathbf{D_d}\hat{\mathbf{V}}\dot{u}(t) + \hat{\mathbf{V}}^T\mathbf{K}\hat{\mathbf{V}}u(t) = \hat{\mathbf{V}}^T\mathbf{b}\tau(t). \tag{3.93}$$

Due to the orthogonality conditions of the eigenvectors, the respective parts of (3.93) ends up as, $\hat{\mathbf{V}}^T\mathbf{M}\hat{\mathbf{V}} = \mathbf{I}$, $\hat{\mathbf{V}}^T\mathbf{K}\hat{\mathbf{V}} = \Omega^2$, $\hat{\mathbf{V}}^T\mathbf{D_d}\hat{\mathbf{V}} = \Lambda$, where Ω is a diagonal matrix containing the undamped natural frequencies of the system and Λ is a diagonal matrix with entries $2\xi_i\omega_i$. The resulting equation of motion then becomes

$$\mathbf{I}\ddot{u}(t) + \Lambda\dot{u}(t) + \Omega^2 u(t) = \hat{\mathbf{V}}^T\mathbf{b}\tau(t). \tag{3.94}$$

The modal displacements and velocities can be transformed back into the original coordinate vector $\mathbf{q}(t)$ through a linear superposition of the modal displacements. The response of the system will then be given as a linear combination of the eigenvectors $\hat{v}_i$, where the modal displacements $u(t) = \begin{bmatrix} u_1(t) & u_2(t) & \dots u_N(t) \end{bmatrix}^T$, weights the contribution each eigenvector gives to

the total displacement. The resulting transformation equation will then be written as,

$$\mathbf{q}(t) = \sum_{i=1}^{N} \hat{v}_i u_i(t), \tag{3.95}$$

where $\hat{v}_i$ is the i^{th} column eigenvector of the system given by the set $\hat{\mathbf{V}} = \begin{bmatrix} v_1 & v_2 & \cdots & v_N \end{bmatrix}$. The great strength of representing the system on modal form is the possibility to obtain a reduced order model which can approximate the true model with good accuracy. As not all eigenvectors are contributing significantly to the response, the less dominant eigenvectors can be neglected. The system is then approximated by an reduced number n_r of the eigenvectors, which gives the new coordinate transform,

$$q(t) = \hat{\mathbf{V}}_r u(t), \tag{3.96}$$

with $u(t) \in \mathbb{R}^{n_m}$ and $\hat{\mathbf{V}}_r \in \mathbb{R}^{2n \times n_m}$. Representing the model on a reduced order form is of great aid when performing numerical calculations of the FE model, as the number of equations needed to solve are greatly reduced. As was seen in Figure 3.18 it is only the first few eigenmodes which will be excited when subjected to loading. Thus, a good approximation of the response can be obtained by using the two first columns in the eigenvector set $\hat{\mathbf{V}}$ when transforming the model to a modal form.

Modal State Space Representation

As for the general system model, the modally reduced model can be represented on a state space form. By introducing a modal state vector $\eta(t) \in \mathbb{R}^{2n_m}$ as

$$\eta(t) = \begin{bmatrix} u(t) \\ \dot{u}(t) \end{bmatrix}, \tag{3.97}$$

the modal representation can be given on state space form as,

$$\dot{\eta}(t) = \mathbf{A}_m \eta + \mathbf{G}_m \tau(t), \tag{3.98}$$

$$y(t) = \mathbf{C}_m \eta(t) + \mathbf{J}_m \tau(t) + v(t), \tag{3.99}$$

where the matrices $\mathbf{A}_m \in \mathbb{R}^{2n_m \times 2n_m}$, $\mathbf{G}_m \in \mathbb{R}^{2n_m \times n_p}$, are given as;

$$\mathbf{A}_m = \begin{bmatrix} \mathbf{0}_{n\times n} & \mathbf{I}_{n\times n} \\ -\Omega^2 & -\Lambda \end{bmatrix}, \quad \mathbf{G}_m = \begin{bmatrix} \mathbf{0}_{n\times p} \\ \hat{\mathbf{V}}_r^T \mathbf{b} \end{bmatrix}.$$

For velocity or displacements measurements, the output matrix $\mathbf{C}_m \in \mathbb{R}^{n_y \times 2n_m}$ will have the following structure, respectively

$$\mathbf{C}_m = \begin{bmatrix} \mathbf{0}_{m\times n} & \mathbf{c}\hat{\mathbf{V}} \end{bmatrix},$$

$$\mathbf{C}_m = \begin{bmatrix} \mathbf{c}\hat{\mathbf{V}} & \mathbf{0}_{m\times n} \end{bmatrix}.$$

For acceleration measurements, the output will yield the following structure

$$\mathbf{C}_m = \begin{bmatrix} -\mathbf{c}\hat{\mathbf{V}}\Omega^2 & -\mathbf{c}\hat{\mathbf{V}}\Lambda \end{bmatrix}, \quad \mathbf{J}_m = \begin{bmatrix} \mathbf{c}\hat{\mathbf{V}}\hat{\mathbf{V}}^T\mathbf{b} \end{bmatrix}.$$

3.9.3 Model Discretization

To implement the model for Matlab simulations the continuous state space models given in (3.87) or (3.98) will be discretized with a zero order hold (ZOH) approximation. The method is valid for both the initial state space representation, and the modal representation. The discrete representation will be given on the form,

$$\mathbf{x}_{k+1} = \Phi \mathbf{x}_k + \Gamma \tau_k, , \tag{3.100}$$

$$\mathbf{y}_k = \mathbf{C}\mathbf{x}_k + v_k, \tag{3.101}$$

where Φ is the state transition matrix, calculated as the matrix exponential of the system matrix given by $\mathbf{A}$ or $\mathbf{A}_m$. Mathematically this is written as,

$$\Phi = e^{\mathbf{A}\Delta t}, \tag{3.102}$$

$$\Phi_m = e^{\mathbf{A}_m \Delta t} \tag{3.103}$$

where Φ is the state transition matrix for the original system, and Φ_m for the modal representation. Δt is the time step size. The input matrix $\mathbf{G}$ or $\mathbf{G}_m$ will be discretized using

$$\Gamma = \int_{\tau=0}^{\tau=dt} e^{\mathbf{A}\tau} d\tau \cdot \mathbf{G} = \mathbf{A}^{-1} (\Phi - \mathbf{I}) \mathbf{G}, \tag{3.104}$$

$$\Gamma_m = \int_{\tau=0}^{\tau=dt} e^{\mathbf{A}_m\tau} d\tau \cdot \mathbf{G}_m = \mathbf{A}_m^{-1} (\Phi_m - \mathbf{I}) \mathbf{G}_m, \tag{3.105}$$

where Γ, Γ_m is the original and modal representation respectively.

Chapter 4

Observer design

In this chapter two different observer designs will be presented with goal to obtain stable state estimates of the system. As both estimators assume a fully observable system, a method for checking observability of linear structural system as presented, based on transformation to a modal representation of the system. In Section 4.2 a dual input-state estimator is presented, where state estimates are obtained through estimating a corrective force for the unknown environmental input forces together with a Kalman-like filter. Section 4.3 presents a Kalman filter design where a state augmentation including a bias force is included.

4.1 Observability

A linear time invariant system is said to be observable if, for any possible sequence of state and control vectors, the current state vector can be determined in finite time using only output data and known input data. For a system written on state space one can check the observability of the system by constructing the well known observability matrix,

$$\mathbb{O} = \begin{bmatrix} \mathbf{C} \\ \mathbf{CA} \\ \mathbf{CA}^2 \\ \vdots \\ \mathbf{CA}^{2n-1} \end{bmatrix}, \tag{4.1}$$

where $\mathbf{C}$ is the output matrix and $\mathbf{A}$ is the system matrix on state space form. The system is said to be observable if and only if $rank(\mathbb{O}) = 2n$, (the total system is consisting of $2n$ states). For a FE model represented on state space form the dimensions of the system matrices tend to get very large, and the construction of the observability matrix can lead to numerical singularities (Paige, 1981). To omit the difficulties with numerical singularities, the use of the modal transformation representation given in (3.92) can be used for investigating observability. A modal transformation will not change the observability of the system (Maes et al., 2015, Appendix B).

Representing the system on a reduced modal form requires that every mode included in the model contribute to the measured output. By the definition of the observability matrix in (4.1)

and the modal output matrix given in (3.99) the test for observability can be reformulated, where the requirement for observability can be given as follows:

A system written on a reduced modal form as in (3.98) and (3.99) is observable if and only if

$$\mathbf{C}\begin{bmatrix}\hat{v}_1 & \hat{v}_2 & \cdots & \hat{v}_r\end{bmatrix} = \mathbf{C}\hat{\mathbf{V}}_r \tag{4.2}$$

do not contain any zero columns.
$\mathbf{C}$ is the system output matrix, and $\hat{\mathbf{V}}_r$ are the mass normalized eigenvectors of the reduced system.
Proof: A proof can be found in Maes et al. (2015, Appendix B).

4.2 Unbiased Force and State Estimation

Due to the unknown disturbance forces acting on the turbine, a dual state and input estimator is suggested. The proposed estimator was first addressed in Gillijns and De Moor (2007). They derived a linear recursive filter based on a minimum-variance unbiased input estimate, where the estimation of states and input is interconnected.

The filter is based on the assumption that no prior knowledge about the evolution of the unknown input is available. The resulting filter has the structure of a Kalman filter, except that the true value of the force input is replaced by an estimate. If the position of all input forces could be assumed known, the filter would act as an estimator where both states and true force input could be estimated without time delay. However, the distribution of the unknown ambient forces (wind, waves, current and 3P) will in reality not be assumed well known. In this case, the joint input-state-estimation can be applied to identify a set of forces, $\hat{\tau}$, acting at selected positions. These forces are then not the true forces acting on the structure, but equivalent corrective forces, which compensate for the unknown sources of disturbance. (Lourens, Papadimitriou, and Gillijns, 2012).

The proposed estimator will be designed by assumptions of a set of acceleration measurements and displacement/strain measurements at predefined nodes. In a practical sense acceleration measurements are heavily used in the industry due to their reasonable accuracy and low cost. Details on the need for displacement measurements will be addressed in Section 4.2.2.

The system considered is presented on a reduced modal form through the coordinate transformation given in Section 3.9.2. On state space form the system model is written as,

$$\begin{aligned} x_{k+1} &= \Phi x_k + \Gamma \tau_k, \\ y_k &= \mathbf{C}x_k + \mathbf{J}\tau_k + v_k, \end{aligned} \tag{4.3}$$

where $\Phi \in \mathbb{R}^{n_m \times n_m}$, $\Gamma \in \mathbb{R}^{n_m \times n_p}$ are the discrete transition and input matrices respectively. $\mathbf{C} \in \mathbb{R}^{n_y \times n_m}$ is the output matrix and $\mathbf{J} \in \mathbb{R}^{n_y \times n_p}$ is the output feedthrough matrix.

v_k is zero mean measurement noise with known covariance $\mathbf{R} = \mathbb{E}\left[v_k v_k^T\right] > 0$.

The considered filter is a three step recursive filter with following steps,

$$\hat{x}_{k|k-1} = \Phi \hat{x}_{k-1|k-1} + \Gamma \hat{\tau}_{k-1}, \tag{4.4}$$
$$\hat{\tau}_k = \mathbf{M}_k (y_k - \mathbf{C}\hat{x}_{k|k-1}), \tag{4.5}$$
$$\hat{x}_{k|k} = \hat{x}_{k|k-1} + \mathbf{L}_k (y_k - (\mathbf{C}\hat{x}_{k|k-1} + \mathbf{J}\hat{\tau})). \tag{4.6}$$

The first step given in (4.4) called the *time update* gives an estimate of x_k using measurements up to time $k-1$and an estimated input force $\hat{\tau}_{k-1} \in \mathbb{R}^{n_p}$. The second step given in (4.5) calculates an updated input force estimate through the gain matrix $\mathbf{M}_k$ and the measurement innovation. The last step given in (4.6) known as the *measurement update* calculates the corrected state estimate of x_k using a gain matrix $\mathbf{L}_k \in \mathbb{R}^{n_m \times n_y}$. $\mathbf{L}_k$ is derived in a similar manner as done in a Kalman filter. The matrices $\mathbf{M}_k$ and $\mathbf{L}_k$ are unknown and will be derived through the filter algorithm. It is assumed that an initial unbiased state estimate $\hat{x}_0$ and its corresponding state error covariance matrix $\mathbf{P}_0^x$ is known. The system is assumed observable. Finally it is assumed that $rank(\mathbf{J}) = n_p$. This is a necessary and sufficient condition for the existence of an unbiased input estimate. Details about this assumption is discussed later.

The resulting filter algorithm will be rendered in this thesis. For reading on the derivation of the filter dynamics, the reader is referred to Gillijns and De Moor (2007).

The filter is initialized by the known initial state estimate and covariance matrix,

$$\hat{x}_0 = \mathbb{E}[x_0], \tag{4.7}$$
$$\mathbf{P}_0^x = \mathbb{E}[(\hat{x}_0 - x_0)(\hat{x}_0 - x_0)^T]. \tag{4.8}$$

The measurement noise covariance matrix $\mathbf{R}$ and a suited process noise covariance matrix $\mathbf{Q}$ will have to be selected. The three step recursive filter has the structure similar to a Kalman filter, but where the true value of the input is replaced by an optimal estimate in a minimum variance based sense. The three steps are given as:

Input estimation:

$$\tilde{\mathbf{R}}_k = \mathbf{C}\mathbf{P}_{k|k-1}^x \mathbf{C}^T + \mathbf{R}, \tag{4.9}$$
$$\mathbf{M}_k = \left(\mathbf{J}^T \tilde{\mathbf{R}}_k \mathbf{J}\right)^{-1} \mathbf{J}^T \tilde{\mathbf{R}}_k^{-1}, \tag{4.10}$$
$$\hat{\tau}_k = \mathbf{M}_k \left(y_k - \mathbf{C}\hat{x}_{k|k-1}\right), \tag{4.11}$$
$$\mathbf{P}_k^\tau = \left(\mathbf{J}^T \tilde{\mathbf{R}}_k^{-1} \mathbf{J}\right)^{-1} \tag{4.12}$$
$$\tag{4.13}$$

Measurement update:

$$\mathbf{L}_k = \mathbf{P}^x_{k|k-1}\mathbf{C}^T\tilde{\mathbf{R}}_k^{-1} \tag{4.14}$$
$$\hat{x}_{k|k} = \hat{x}_{k|k-1} + \mathbf{L}_k\left(y_k - (\mathbf{C}\hat{x}_{k|k-1} + \mathbf{J}\hat{\tau}_k)\right) \tag{4.15}$$
$$\mathbf{P}^x_{k|k} = \mathbf{P}^x_{k|k-1} - \mathbf{L}_k\left(\tilde{\mathbf{R}}_k - \mathbf{J}\mathbf{P}^\tau_k\mathbf{J}^T\right)\mathbf{L}_k^T \tag{4.16}$$
$$\mathbf{P}^{x\tau}_k = \left(\mathbf{P}^{\tau x}_k\right)^T = -\mathbf{L}_k\mathbf{J}\mathbf{P}^\tau_k \tag{4.17}$$
$$\tag{4.18}$$

Time update:

$$\hat{x}_{k+1|k} = \Phi\hat{x}_{k|k} + \Gamma\hat{\tau}_k \tag{4.19}$$
$$\mathbf{P}^x_{k+1|k} = \begin{bmatrix}\Phi & \Gamma\end{bmatrix}\begin{bmatrix}\mathbf{P}^x_{k|k} & \mathbf{P}^{x\tau}_k \\ \mathbf{P}^{\tau x}_k & \mathbf{P}^\tau_k\end{bmatrix}\begin{bmatrix}\Phi^T \\ \Gamma^T\end{bmatrix} + \mathbf{Q} \tag{4.20}$$

In the input estimation, the goal is to derive a gain matrix $\mathbf{M}_k$ such that (4.11) yields an estimate of τ_k. In the *measurement update*, the gain matrix $\mathbf{L}_k$ is to be derived with goal to update the state estimates $\hat{x}_{k|k}$. In the last part of *time update*, the input estimate is finally added to (4.19), updating the state estimate.

4.2.1 Input and Measurement Restrictions

The necessary assumption of $rank(\mathbf{J}) = n_p$ stems from the invertibility requirement of $\tilde{\mathbf{R}}_k$ given in (4.9). Some restrictions on the number of measurements and the number of modes used when representing the model on modal form has to be made to avoid rank deficiency of $\tilde{\mathbf{R}}_k$. On modal form, the feedthrough matrix is written as $\mathbf{J} = \left[\mathbf{c}\hat{\mathbf{V}}_r\hat{\mathbf{V}}_r^T\mathbf{b}\right]$ and the assumption on $rank(\mathbf{J})$ can only be obtained if the following is satisfied:

$rank(\mathbf{J}) = n_p$, if and only if the number of eigenmodes n_m included and the number of measurements n_y are higher than the number of known force inputs n_p.

This requirement comes from the fact that $rank(\mathbf{J}) = min\{n_m, n_y, n_p\}$.
This can be shown by assuming $\mathbf{J}$ as the product of two matrices $\mathbf{S_1}$ and $\mathbf{S_2}$, where $\mathbf{S_1} = \mathbf{c}\hat{\mathbf{V}}_r \in \mathbb{R}^{n_y \times n_m}$ and $\mathbf{S_2} = \hat{\mathbf{V}}_r^T\mathbf{b} \in \mathbb{R}^{n_m \times n_p}$. The rank of $\mathbf{S_1}$ and $\mathbf{S_2}$ satisfies the following inequality (Bernstein, 2009),

$$rank(\mathbf{S_1}, \mathbf{S_2}) \leq min(rank(\mathbf{S_1}), rank(\mathbf{S_2})), \tag{4.21}$$

with

$$rank(\mathbf{S_1} \leq min(n_y, n_m),$$
$$rank(\mathbf{S_2} \leq min(n_m, n_p).$$

From this it follows that $rank(\mathbf{J}) = n_p$ if the following restrictions are satisfied,

1. $n_m \geq n_p$,
2. $n_y \geq n_p$.

This shows that the number of eigenmodes used in the reduced model and the number of measurements have to be equal to or greater than the number of corrective forces used in the estimator model. A detailed discussion on the topic can be found in Lourens et al. (2012). The paper also discuss an extension to the filter algorithm where rank deficiency can be avoided by a truncation method. For this work it was not deemed necessary to perform a truncation.

4.2.2 Uniqueness of State Estimates

The uniqueness of the estimated forces and states depends on the system's transmission zeros. Let

$$P_\Sigma = \begin{bmatrix} \Phi - \lambda_i \mathbf{I} & \Gamma \\ \mathbf{G} & \mathbf{J} \end{bmatrix}, \tag{4.22}$$

where the complex number λ_i given in P_Σ is a transmission zero of the system in (4.3) if

$$rank(P_\Sigma) \leq 2n + min(n_p, n_y). \tag{4.23}$$

If λ_i is a finite zero transmission zero of the system, then there exists an initial state vector $\mathbf{x}_0 \in \mathbb{C}^{2n}$ and force inputs $\tau_0 \in \mathbb{C}^{n_p}$ which will yield an output $y_k = \mathbf{0}, \forall k$. Taking only acceleration or velocity measurements of the structure will lead to at least one purely real transmission zero located at the unit disk ($\lambda_i = 1$) (Proof: Maes et al. (2015, Appendix D)). This is due to the fact that velocity and acceleration measurements are insensitive to excitation or state deflections which are constant in time. The static component of the states and/or force inputs will therefore not be possible to retrieve having only velocity or acceleration measurements. Unique estimation of states and force input can be obtained if the following assumption is fulfilled.

$$rank\left(\mathbf{J} - \mathbf{G}\left(\Phi - \mathbf{I}\right)^{-1}\Gamma\right) = min(n_p, n_y), \tag{4.24}$$

where n_y is the total number of measurements, consisting of acceleration and displacement measurements, and n_p is the number of applied input forces. The matrix given in (4.24) will have $rank = min(n_p, n_y)$ if and only if the number of displacement/strain measurements n_{yd} of the total number of measurements are larger than or equal to number of known force inputs n_p.
Transforming the system to a modal representation does not change the transmission zeros of the system or the requirement for uniqueness given in (4.24). Proof for the claim given in (4.24) and that the transmission zeros stays unchanged under transformation can be found in Maes et al. (2015, Appendix F) and Maes et al. (2015, Appendix D), respectively.

4.3 Bias Estimator

Another type of estimator can be designed by the classic Kalman filter where the system state will be augmented to include a bias term. By estimating a bias term accounting for unmodeled dynamics and slowly varying environmental forces, it is possible to obtain state estimates with out steady state error. The system will be represented on a reduced modal form consisting of the n_m first eigenmodes. The bias state vector $b \in \mathbb{R}^{n_b}$ can be represented by a first order $Markov$ model

$$\dot{b} = -\mathbf{T}_b^{-1} b + \mathbf{E}_b w_b, \tag{4.25}$$

where $w_b \in \mathbb{R}^{n_m}$ is a zero mean Gaussian white noise vector, $\mathbf{T}_b \in \mathbb{R}^{n_m \times n_m}$ is a diagonal matrix consisting of bias time constants and $\mathbf{E}_b$ is a diagonal scaling matrix. The bias vector is added to the observer dynamics, acting as a force, correcting for the unmodeled environmental forces. The observer system equation will be written as,

$$\dot{b} = -\mathbf{T}_b^{-1} b + \mathbf{E}_b w_b, \tag{4.26}$$

$$\mathbf{I}\ddot{\hat{u}} = -\Lambda \dot{\hat{u}} - \Omega \hat{u} + b, \tag{4.27}$$

which on state space form can be rewritten as

$$\dot{\hat{x}} = \hat{\mathbf{A}}\hat{x} + \mathbf{E}w, \tag{4.28}$$

$$\hat{y} = \mathbf{C}\hat{x} + v, \tag{4.29}$$

where $\hat{x}$ is the new augmented state vector, written as,

$$\hat{x} = \begin{bmatrix} \hat{u} \\ \dot{\hat{u}} \\ b \end{bmatrix}. \tag{4.30}$$

$\hat{u}$ and $\dot{\hat{u}}$ are the modal state estimates and b is the bias force vector. The observer system matrix $\hat{\mathbf{A}}$ will be represented as,

$$\hat{\mathbf{A}} = \begin{bmatrix} \mathbf{0}_{n\times n} & \mathbf{I}_{n\times n} & \mathbf{0}_{n_b\times n_b} \\ -\Omega & -\Lambda & \mathbf{I}_{n_b\times n_b} \\ \mathbf{0}_{n_b\times n} & \mathbf{0}_{n_b\times n} & -\mathbf{T}_b \end{bmatrix}, \tag{4.31}$$

and disturbance matrix $\mathbf{E}$ as,

$$\mathbf{E} = \begin{bmatrix} \mathbf{0}_{n\times n_b} \\ \mathbf{0}_{n\times n_b} \\ \mathbf{E}_b \end{bmatrix}. \tag{4.32}$$

The system equations will be discretized as presented in Section 3.9.3, which gives the discretized observer equations;

$$\hat{x}_{k+1} = \hat{\Phi}\hat{x}_k + \Gamma w_k \tag{4.33}$$

$$\hat{y}_k = \mathbf{C}\hat{x}_k + v_k. \tag{4.34}$$

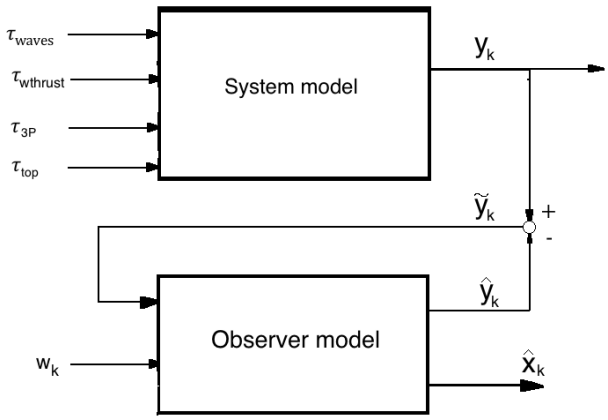

Figure 4.1: Illustration of observer model where the bias term is accounting for the unmodeld environmental forces

Where $\hat{\Phi} \in \mathbb{R}^{2n_m \times 2n_m}$, and $\Gamma \in \mathbb{R}^{2n_m \times n_b}$.
The bias term will consist of $n_b = n_m$ $force$ terms, where each term is driven by zero mean white noise, and will be used as a correcting term applied to each mode together with a Kalman filter, to obtain state estimates with out steady state error.

The Kalman filter is an efficient recursive filter that estimates the state of a linear or nonlinear dynamic system from a series of noisy measurements. It is widely used in sensor and navigation systems since it can reconstruct unmeasured states as well as remove white and colored noise from the state estimates (Fossen, 2011). The discrete Kalman-filter is a two step recursive algorithm with many similarities to the previously represented filter. The first step, called the $prediction$ step, produces estimates of the current state variables, after a next measurement update is available (polluted with measurement noise), the state estimates are updated using a weighted average matrix known as the Kalman gain. The gain relies more weight to estimates with higher certainty. As the filter is recursive, it can run in real time, using only the present measurements, previous state estimate and previously calculated state error covariance matrix.

The Kalman filter equations can be given as;

Predictor:

$$\hat{x}_{k|k-1} = \hat{\Phi}\hat{x}_{k-1|k-1}, \tag{4.35}$$

$$\mathbf{P}_{k|k-1} = \hat{\Phi}\mathbf{P}_{k-1|k-1}\hat{\Phi}^T + \Gamma\mathbf{Q}\Gamma^T. \tag{4.36}$$

Update:

$$\mathbf{L}_k = \bar{\mathbf{P}}_k\mathbf{C}^T\left(\mathbf{C}\bar{\mathbf{P}}_k\mathbf{C}^T + \mathbf{R}\right)^{-1}, \tag{4.37}$$

$$\mathbf{P}_{k|k} = (\mathbf{I} - \mathbf{L}_k\mathbf{C})\,\bar{\mathbf{P}}_k\,(\mathbf{I} - \mathbf{L}_k\mathbf{C})^T + \mathbf{L}_k\mathbf{R}\mathbf{L}_k^T, \tag{4.38}$$

$$\tilde{y}_k = \left(y_k - \mathbf{C}\hat{x}_{k|k-1}\right), \tag{4.39}$$

$$\hat{x}_{k|k} = \hat{x}_{k|k-1} + \mathbf{L}_k\tilde{y}_k. \tag{4.40}$$

4.4 Estimator Design With Modeling Errors

The estimator equations written in previous section assumed a perfect matching between the system model and the estimator model. It will be of interest to test the performance using an estimator model not matching the "true" system model. The erroneous model will be assumed as an additive matrix formulation having the same amount of elements as the system model, however with a difference in its inertia, stiffness and damping matrix. The new matrices can be constructed in the following way,

$$\bar{\mathbf{M}} = \mathbf{M} + \delta_1\mathbf{M},$$
$$\bar{\mathbf{K}} = \mathbf{K} + \delta_2\mathbf{K},$$
$$\bar{\mathbf{D}}_\mathbf{b} = \mathbf{D}_\mathbf{b} + \delta_3\mathbf{D}_\mathbf{b},$$

where $\bar{\mathbf{M}}$, $\bar{\mathbf{K}}$ and $\bar{\mathbf{D}}_\mathbf{b}$ are the new inertia, stiffness and damping matrices, respectively. The factors δ_1 , δ_2 and δ_3 are chosen such that the new model is stable, but with a noticeable difference in its response. The new model will be represented on state space form and reduced to modal form through the same procedure as done in section 3.9.2.

Chapter 5

Simulation Results

In this chapter the response of the resulting model when subjected to the various modeled environmental loads will be tested. An element sensitivity study is done to investigate the behavior of the structure with respect to the discretization of the model. The observer performance for the different disturbances will also be addressed and discussed.

5.1 Simulation Setup

The first simulation will examine the sensitivity on the number of elements included in the model. The setup will be based as a convergence study where the effect of increasing the number of elements will be examined. Simulations regarding the response of the structure when subjected to the environmental disturbances will be done by exposing the structure to each of the environmental forces independently, before a combined loading scenario will be simulated. The response study will be given in the following order,

- Regular and irregular waves
- Wind ramp and fluctuating wind thrust
- 3P Loading
- Water current
- Combined loading for a operating condition and a high wave condition

The modeled estimators will be exposed to the modeled environmental disturbances and compared to the true nodal displacements and velocities at predefined nodes. The intended simulation setup will be,

- Sinusoidal excitation
- Operating condition
- High wave condition
- Modeling error simulation

A discussion on the simulated results for both loading scenarios and estimator performance will be presented consecutively after each simulation.

5.2 Element Sensitivity Study

To investigate the sensitivity of the model to increased number of elements, simulations with varying amount of elements is performed. The transversal displacement between two nodes in the turbine section at height $z = 47m$ above sea level is compared. Since the FE model is a linear model it is expected that the element sensitivity with respect to displacements is equal over the whole turbine structure. The turbine model will be exposed to a sinusoidal load of amplitude 10^6 [N] and frequency $\frac{\pi}{5}$ [rad/s]. The load is applied as a transversal nodal force at the top node. An illustration of the simulation setup can be seen in Figure 5.1.

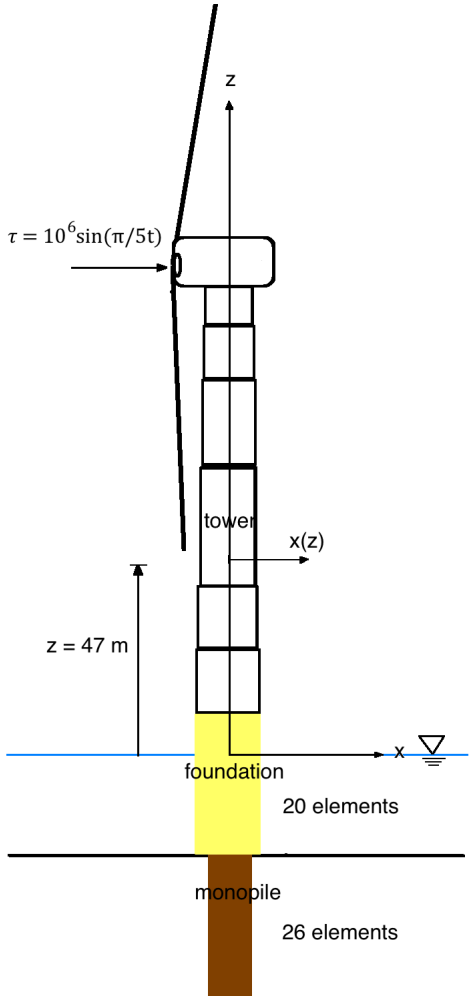

Figure 5.1: Simulation setup for element sensitivity study of the turbine structure with constant number of elements in foundation and monopile section and varying number of elements in tower section.

The response study is done by varying the amount of elements in the tower section for each simulation, but keeping the number of elements in the foundation and monopile section constant with 26 and 20 elements respectively. To compare the effect of increasing the number of elements, a root mean square deviation comparison with a more refined model will be done. The element distribution of the refined model can be seen in Table 5.1.

Sectional number of elements in refined model		
Model section	No. of elements	Element length [m]
Monopile	360	0.12
Foundation	200	0.20
Tower	250	0.46

Table 5.1: Number of elements in refined model

5.2.1 Results on Element Sensitivity Study

Figure 5.2 shows the transversal displacement of the turbine tower from the sinusoidal varying tower top load. As the figure shows, the response amplitude is varying with the amount of elements. As can be observed, the difference in response amplitude is getting less noticeable with increased number of elements. The response amplitude is as expected converging to a limit. Comparison of the first four natural frequencies showed that even for the lowest simulated number of elements, the deviation in natural frequencies was at the highest about 2% (second bending mode) compared to the refined model. Figure 5.3 shows the RMSD of the response amplitude for varying amount of elements compared to the refined model given in Table 5.1. The RMSD plot shows that increasing the amount of elements above 25 elements will give less and less difference in response, such that increasing the amount of elements in the tower section above 25 elements will give little new knowledge about the response amplitude.

As the element sensitivity study showed, the impact of increasing the number of elements has little effect after a certain amount of elements. Thus, in further simulations, a model with discretization as shown in Table 5.2 will be used.

Model discretization for loading simulations		
Model section	No. of elements	Element length [m]
Monopile	26	1.61
Foundation	20	2
Tower	25	4.6

Table 5.2: Number of elements for model used in simulations of environmental loads

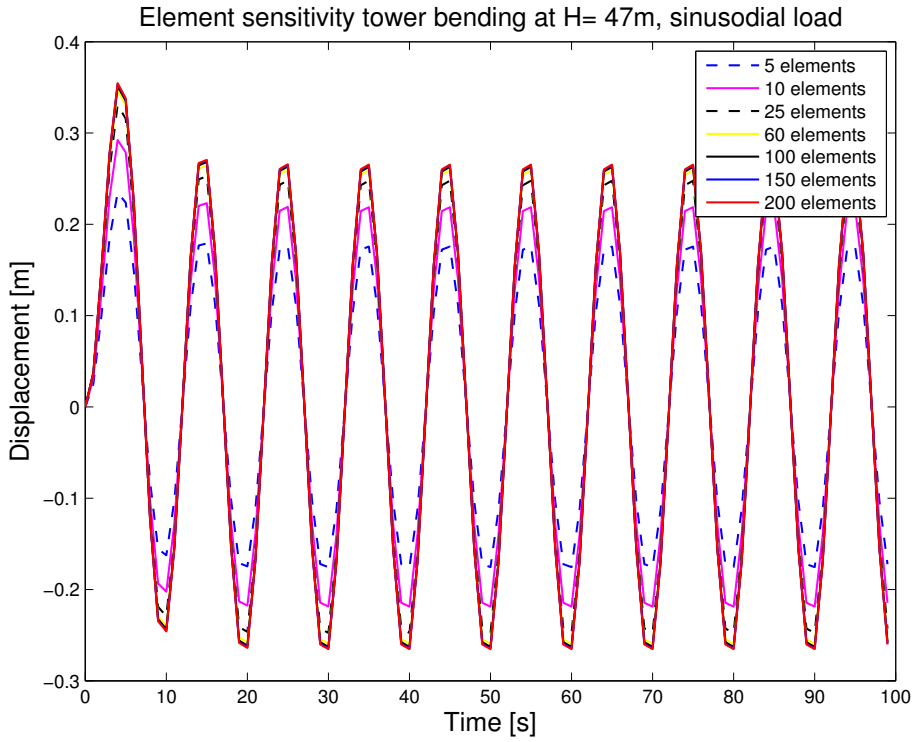

Figure 5.2: Tower top displacement response of turbine structure exposed to sinusoidal excitation for varying amount of tower section elements.

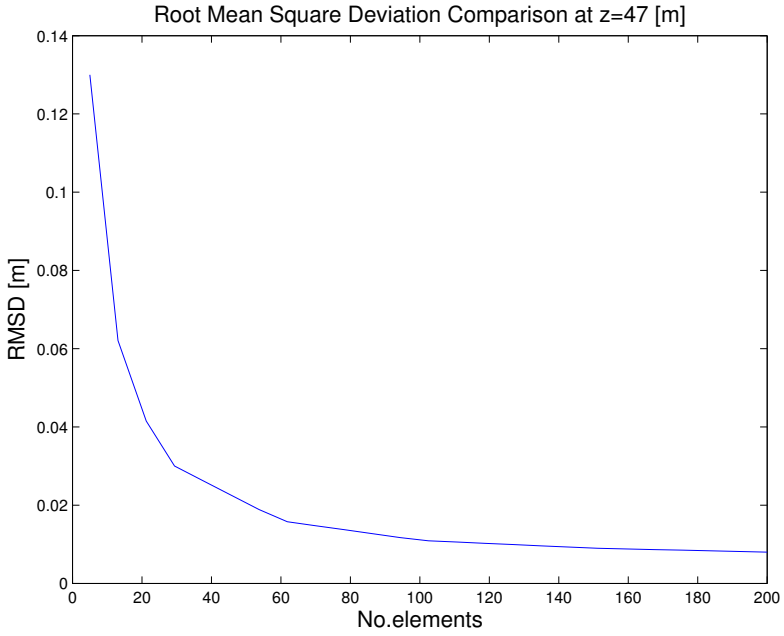

Figure 5.3: Comparison of RMSD in transversal displacement at the predefined height $z = 47$ m for increasing number of elements

5.3 Wave Loading Simulations

As a first simulation on the structure's response to loading, a single sinusoidal wave propagating with amplitude $\xi_A = 1$ [m] and circular frequency $\omega_w = 0.5[rad/s]$ in positive x direction is assumed. The regular wave simulation will be used for validating the response of the structure, with respect to response amplitude, frequency and phase shift.

The structure will also be exposed to two differenent irregular sea states based on the JONSWAP spectrum. Specifications of the specter parameters can be seen in Table 5.3. The first simulation is for a smaller sea state with significant wave height $H_{m0} = 1$ m. The second simulation is for a higher sea state with significant wave height $H_{m0} = 5$ m. It should be noted that since it is assumed that the turbine is operating in finite water depth, the specter should in reality be fitted for use in finite water. It is assumed that the difference in results between an adjusted and not adjusted JONSWAP specter will have little impact on the results, such that adjustments of the specter will not be made.
The wave specter is computed using the function $jonswap.m$ provided in the $WAFO\ toolbox$ (Brodtkorb et al., 2000). To capture a wide range of contributions to response, the maximum frequency f_w^{max} is chosen 3 times the peak frequency. Based on work done in Torsethaugen et al. (1985) $jonswap.m$ suggest that the choice of peakness factor γ is related to H_{m0} and set to,

$$\gamma = exp\left(3.484\left(\frac{1-0.1975QT_p{}^4}{H_{m0}{}^2}\right)\right), \tag{5.1}$$

where Q is given by

$$Q = 0.036 - 0.0056\frac{T_p}{\sqrt{H_{m0}}}. \tag{5.2}$$

The simulations will run for 300 seconds and with a time step of $\Delta t = 0.1$ [s].

Simulated sea state data			
Parameter	Variable	Run 1	Run 2
Significant wave height [m]	H_{m0}	1	5
Peak Period [s]	T_p	5	11
Peakness factor [-]	γ	1.05	10.18
Max frequency [1/s]	f_w^{max}	$\frac{3}{T_p}$	$\frac{3}{T_p}$
Frequency increment [1/s]	Δf_w	$\frac{3}{271}$	$\frac{3}{271}$

Table 5.3: Simulated sea states data

5.3.1 Results of Wave Simulations

Regular Wave Simulation

Figure 5.4 shows the transversal displacement of the turbine tower top and corresponding velocity when subjected to a sinusoidal wave component. The figure also shows the transversal nodal wave force on the element located at sea surface. As shown in Figure 5.5, the response of the structure is oscillating with the same frequency as the loading, but with a phase shift. This is as expected, as the frequency of response for a linear system exposed to a sinusoid with frequency ω_w will be a sinusoid with the same frequency, but with a phase shift ϕ.

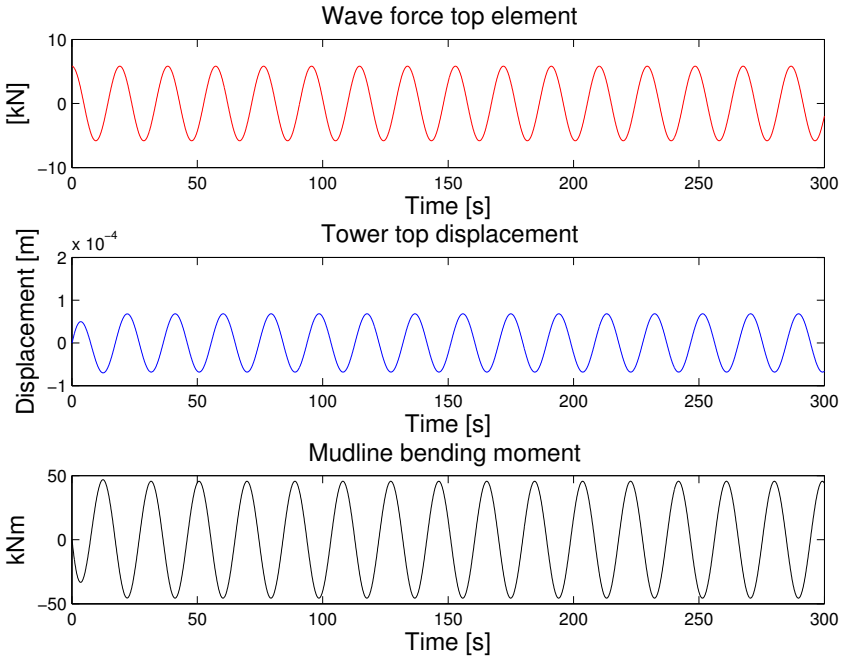

Figure 5.4: Towertop transversal displacement and velocity compared to loading for parameters; $H_{m0} = 1[m]$ $\omega = 0.5[rad/s]$

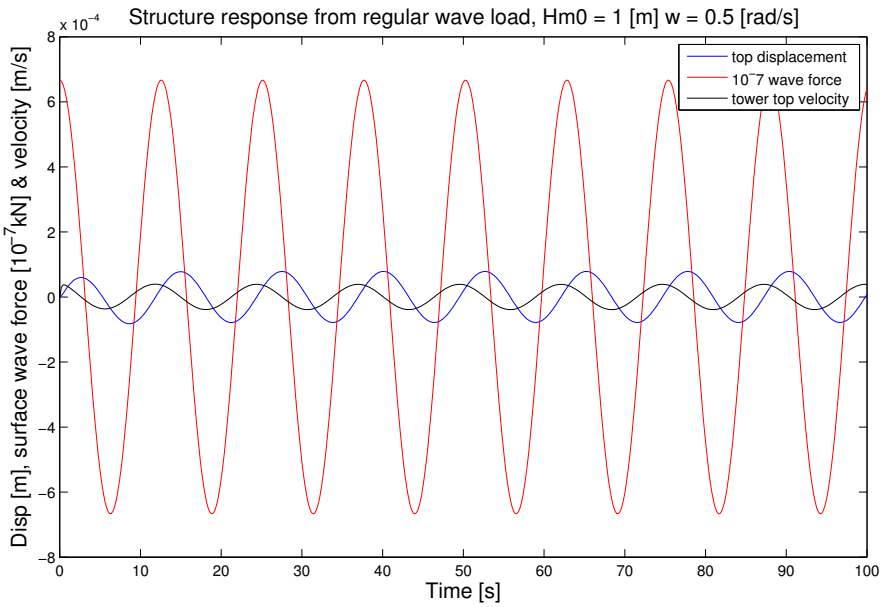

Figure 5.5: Comparison of response and wave load on turbine structure from a regular wave for parameters; $H_{m0} = 1[m]$ $\omega = 0.5[rad/s]$ (100 seconds simulation)

Irregular Waves Simulation

Run 1: Figure 5.6 show the response of the structure subjected to sea state $H_{m0} = 1$ [m] and peak period $Tp = 5$ [s]. As the figure show, the current sea state will not contribute to any significant displacement of the tower top. It does contribute to a cyclical bending moment which can play an import an role in the accumulated fatigue damage over the lifetime of an offshore turbine. The peak frequency of the simulated sea state is close to the first natural bending of the system, which will amplify the structure response. Fortunately, the amount of energy in the waves at this frequency is low, such that the amplification of the response is limited.

Run 2: Figure 5.7 show the response characteristics from the simulated sea state with $H_{m0} = 5$ [m] and peak period $T_p = 11$ [sec]. As can be seen, the response is larger than for the smaller sea state, but still the tower top deflection is limited. However, the total bending moment is indeed increased a significant amount, leading to higher amplitude in the fluctuated loading, and increased fatigue damage if subjected to this sea state over longer periods.

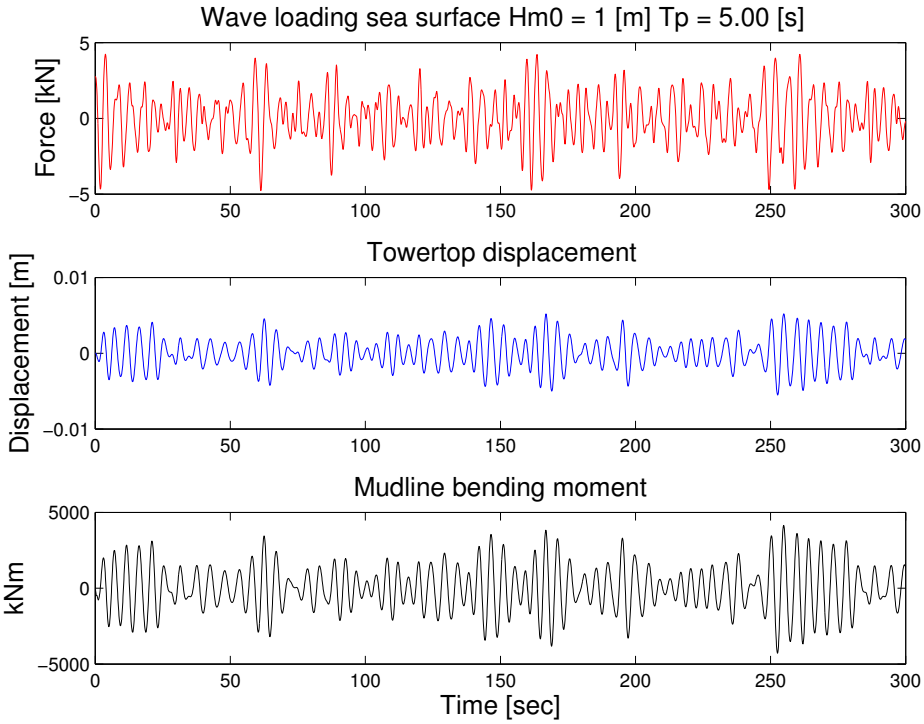

Figure 5.6: Results of Wave Load Simulation, $H_{m0} = 1m$ $T_p = 5s$

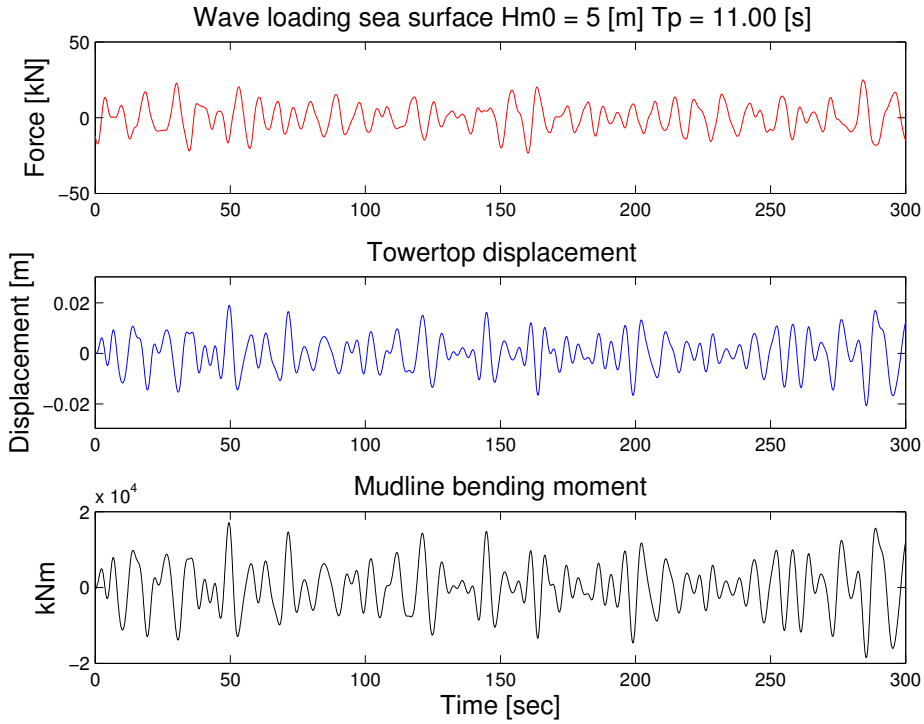

Figure 5.7: Results of Wave Load Simulation, $H_{m0} = 5m$ $T_p = 11s$

5.4 Wind Thrust Simulations

The wind speed acting over the turbine blades contributes to a large thrust force on the tower top. This thrust force is by far the most dominant force acting on the structure, and contribute to a significant bending moment on the structure due to the long moment arm. Simulations from a wind ramp scenario, and a turbulent wind field will be tested.

For the wind ramp scenario, a linearly increasing wind speed inflicted on the top transversal node is applied. The wind speed is assumed to increase from 0 [m/s] to 11 [m/s]. The total thrust force applied will then be given by (3.52). With increasing wind speed, a constant thrust coefficient $C_T = 0.5$ [-] will be assumed. The purpose of this simulation is to identify the behavior of the turbine, and investigate unphysical behavior.

In the simulation for a turbulent wind field, two simulations will be run. Properties for the simulated wind field can be seen in Table 5.4. The parameters used for calculating the wind thrust force can be seen in Table 5.5. To show the effect of turbulence intensity two simulations will be run with different intensity. The thrust force obtained from the turbulent wind field is modeled using (3.75). The simulated thrust force is assuming a constant thrust coefficient C_T. The drag force acting on the tower structure is neglected, as its contribution to response is limited compared to the thrust force generated from the turbine blades. Figure 5.8a and 5.8b shows the realization of the Kaimal spectra used in the two following simulations.

Wind simulation variables			
	Variable	Run 1	Run 2
Turbulence intensity [-]	$\frac{\sigma}{\bar{U}}$	0.01	0.02
Mean wind speed [m/s]	$\bar{U}$	11	11
Length scale [m]	l	600	600
Sample time [s]	Δt	0.1	0.1
Frequency increment [1/s]	Δf	0.001	0.001

Table 5.4: Wind field variables

Wind Thrust variables		
Length turbine blades [m]	R_b	89
Swept area turbine blades [m^2]	A_r	$2.5 \cdot 10^4$
Thrust coefficient [-]	C_T	0.63
Density air [kg/m^3]	ρ_a	1.225

Table 5.5: Wind thrust force variables

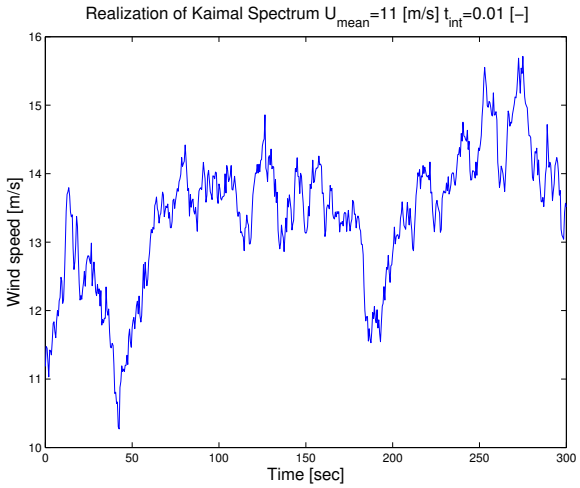

(a) Kaimal specter, Run 1, $\frac{\sigma}{\bar{U}} = 0.01$, $\bar{U} = 11[m/s]$

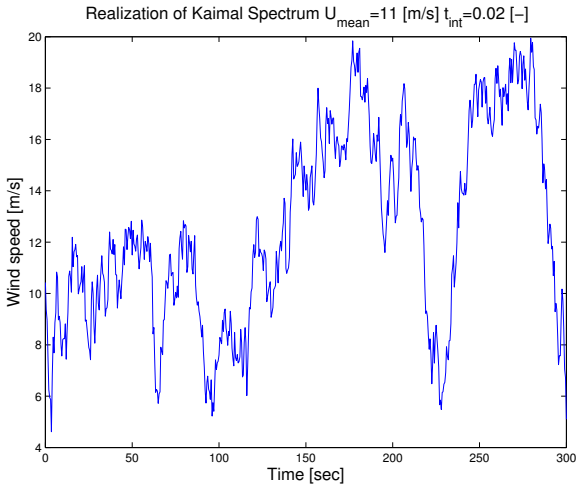

(b) Kaimal specter, Run 2, $\frac{\sigma}{\bar{U}} = 0.02$, $\bar{U} = 11[m/s]$

Figure 5.8: Realization of the Kaimal spectra used in the wind thrust simulation study

5.4.1 Results of Wind Thrust Simulations

Wind Ramp

Figure 5.9 shows the response of the structure when subjected to the wind ramp scenario. As the model is a linear model, one can expect the same response pattern but with different magnitude for the other nodes along the model. The steady state response of the structure and thrust force is plotted. As can be observed from the middle plot of Figure 5.9, the turbine is obtaining a static deflection at around 0.8 m. In the same plot, one can observe at around 60 seconds in the simulation, that the tower top displacement is overshooting the steady state response by a small fraction before returning to the steady state. By looking at the velocity plot at the bottom part of the figure, one will see that the tower top velocity will drop from an almost constant velocity, to zero as the tower top obtains its static deflection. The oscillations in the velocity is related to the overshoot of the tower top displacement, which causes the top to swing back and forth before settling at the static deflection.

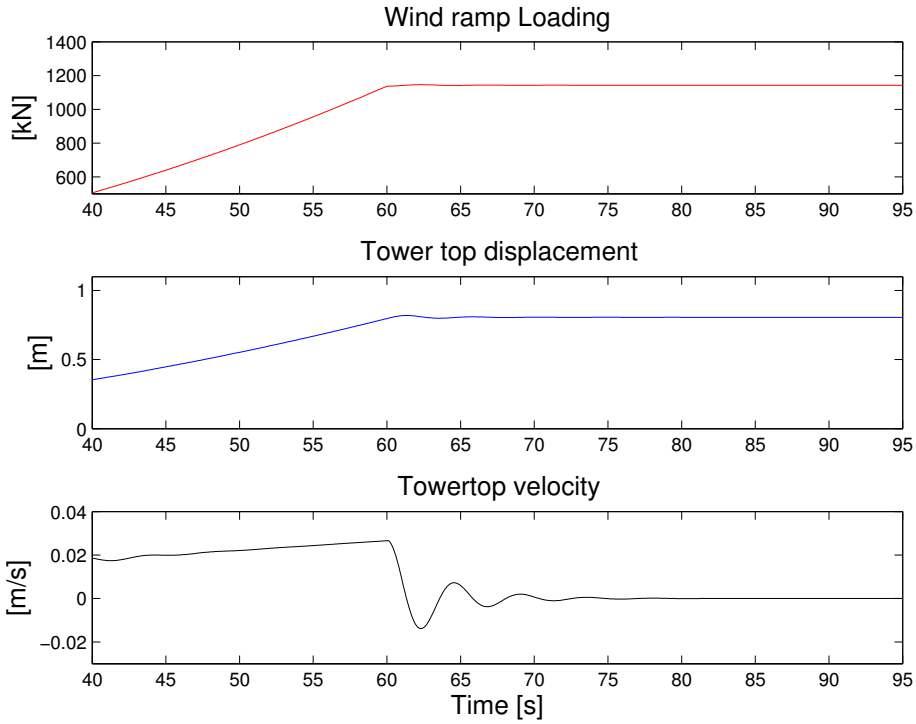

Figure 5.9: Tower top response to a linearly increasing wind thrust force

Fluctuating Wind

Run 1: Figure 5.10 shows the time series response of the structure for the turbulent wind field with turbulence intensity $\frac{\sigma}{\overline{U}} = 0.010$. As can be seen from the middle plot, the wind thrust force generated from the wind loads contribute to a higher deflection on the turbine than the other previously simulated forces, and thus a higher bending moment at the mudline. The maximum tower top displacement is seen to be around 0.9 m. The mudline bending moment in bottom part of the figure is showing same response pattern as the displacement, but with opposite sign. This is due to the definition of displacement in positive x-direction, will yield a negative bending moment.

Run 2: The higher amount of turbulence in the wind gives larger fluctuations in the response pattern, as can be seen from Figure 5.11. At around 220 seconds, a sudden drop in the wind speed coincide with a drop in response, and bending moment. As can be seen, the amplitude and amount of fluctuations are generally higher for the more turbulent wind field, which contributes to a higher amount of fatigue damage.

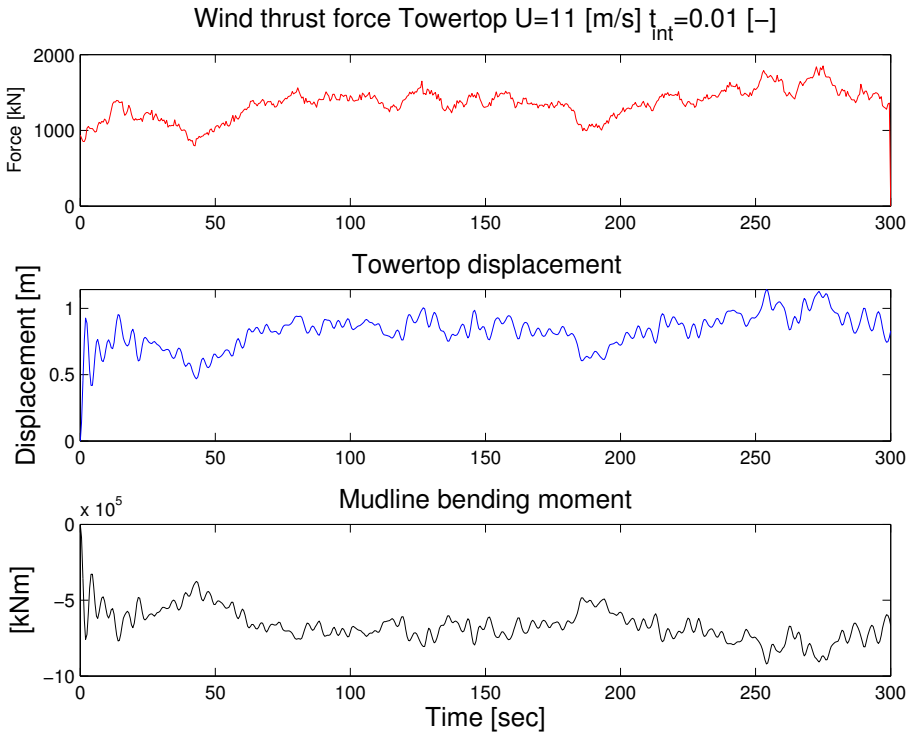

Figure 5.10: Results of wind thrust force simulations for $\bar{U} = 11[m/s]$, $\frac{\sigma}{I} = 0.01$

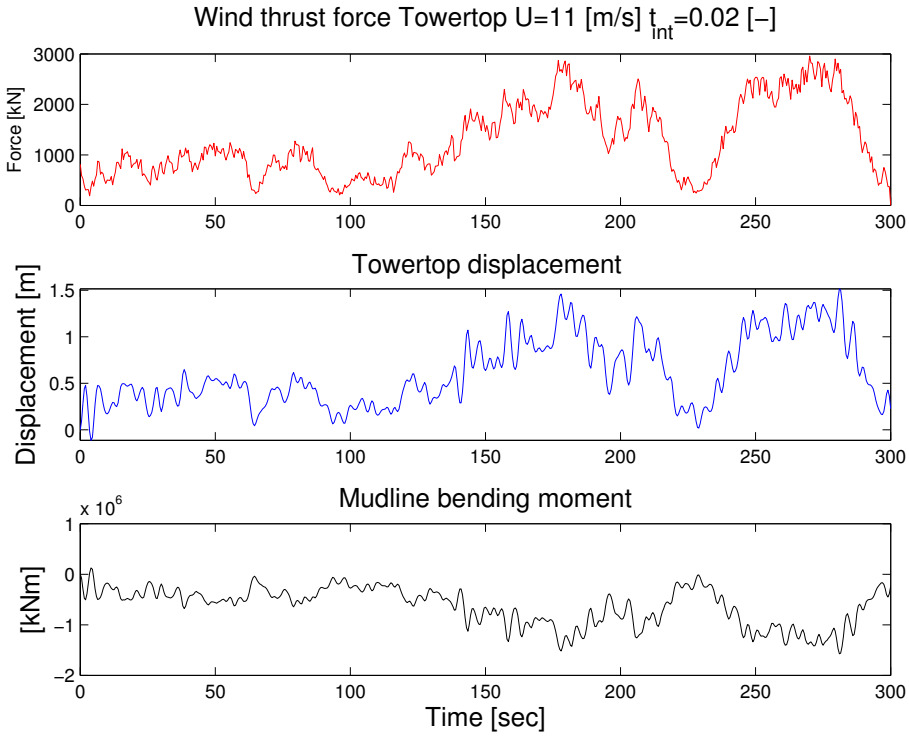

Figure 5.11: Results of wind thrust force simulations for $\bar{U} = 11[m/s]$, $\frac{\sigma}{I} = 0.02$

5.5 3P Loading Simulations

The oscillating drag force experienced by the turbine structure when subjected to a $3P$ load will be simulated. Two scenarios will be run. The first scenario investigate a constant wind field with no gust, where as the second simulation will have the effect of gust included. The wind speed acting along the turbine tower will be scaled with the wind speed power law given by (3.49) with scaling parameter $\mu = 0.27$ and mean wind speed at reference height $U(z_r) = 11$ [m/s] where $z_r = 100$ m. The turbine rotor is assumed to operate at a rotational frequency of $\omega_r = 9.6$ [rpm]. These rotational speed and wind speed are chosen with respect to being the optimal working condition for the 10 MW reference turbine, which this FE model is built on.

5.5.1 Results of 3P Loading Simulations

Run 1: Figure 5.12 show the response of the structure when subjected to the $3P$ loading for a constant wind and no turbulence. The response shows that the effect of the $3P$ loading in response of the structure is very limited. The total force variation it contributes with is not as large as initially anticipated.

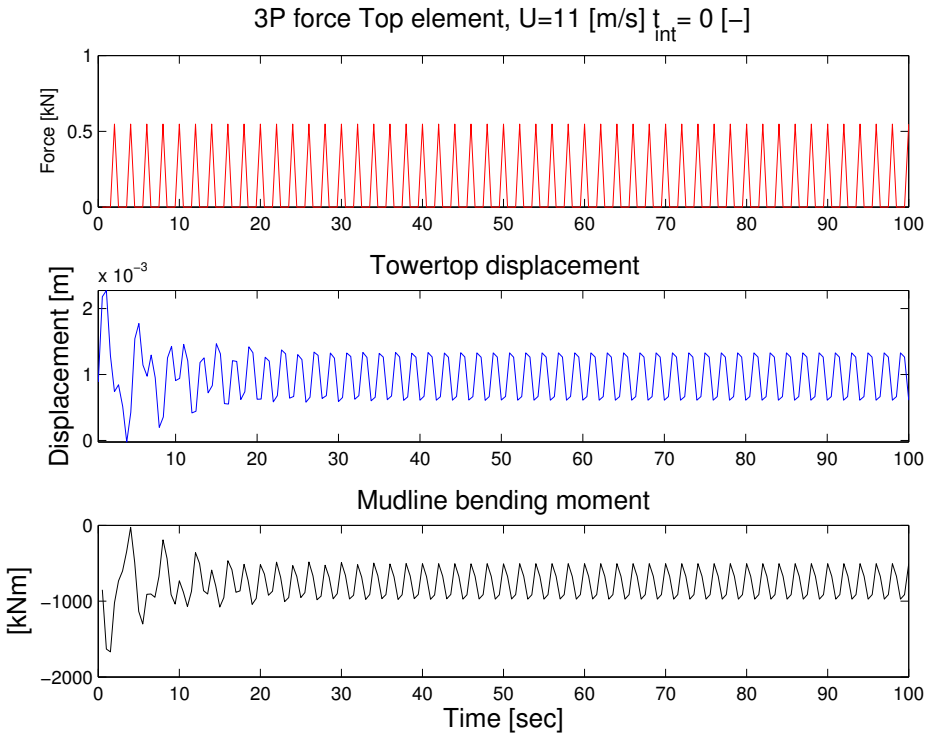

Figure 5.12: 3P loading response for constant wind with no gust $\bar{U} = 11[m/s]$, $\omega_r = 9.6$ [rpm]

Run 2: In Figure 5.13 one can see the response from $3P$ loading when turbulent wind is present. This figure does also suggest that the response of the structure is limited, and that it does not seem to give a response as first assumed. It should however be mentioned that as wind turbines tend to get larger, the natural frequencies of the structure tend to get lower. Awareness regarding the possibility that the second bending mode of the turbine could interact within the region for possible $3P$ loading frequencies could become more and more important in the future when designing larger wind turbines.

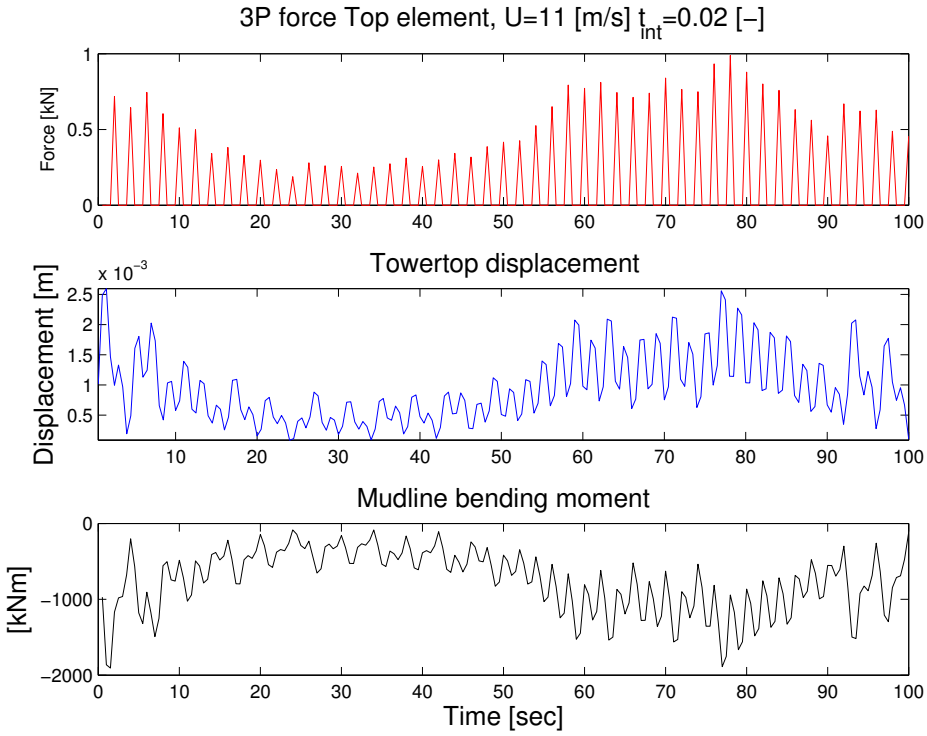

Figure 5.13: 3P loading response for constant wind with gust $\bar{U} = 11[m/s]$, $\omega_r = 9.6$ [rpm] $\frac{\sigma}{I} = 0.02$

5.6 Current Loading Simulation

In the following water current simulation, a uniform water current acting over the wetted section of the model with a constant current velocity of $V_c = 1$ [m/s] is assumed.
A drag coefficient of $C_d = 0.8$ is used, The current drag force is given by (3.71). Current forces is not necessarily the most significant or fatigue enhancing environmental loads an OWT is subjected to, but a simulation is included as a means to include as many forces as possible when in a later stage testing the designed estimators performance.

5.6.1 Results of Current Loading Simulation

As can be seen from Figure 5.14, the response of the structure when subjected to an uniform current field will at steady state behavior yield a static displacement of the tower top. The current field will induce a static bending moment at the seabed. The displacement of the tower top will induce an extra bending moment on the structure due to the large tower top weight as explained in Section 3.7.3. This is included into the mudline bending moment shown in the bottom part of the figure.

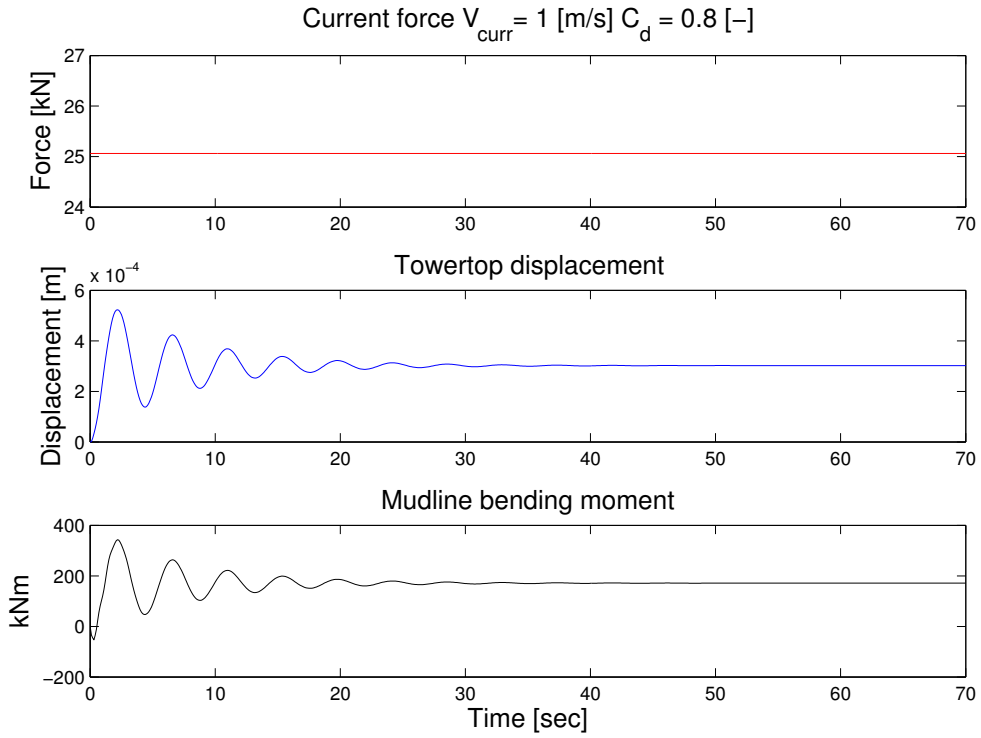

Figure 5.14: Current loading response for uniform current velocity $V_c = 1$ [m/s].

5.7 Combined Loading Simulations

In this section, the modeled structure will be exposed to all the previously modeled environmental forces. The total force vector will then consist of irregular waves, a turbulent wind field, water current and 3P rotor-tower interaction forces. Two different scenarios will be run, where the first will be considered as a normal operating condition for the turbine, operating at a rotational velocity of 9.6 [rpm] with mean wind speed $\bar{U} = 11$[m/s] and turbulence intensity $\frac{\sigma}{\bar{U}} = 0.01$ [-]. The sea state will have a significant wave height $H_{m0} = 1$ [m] and peak period $T_p = 5$[s]. In the second simulation a higher sea state with significant wave height $H_{m0} = 5$ [m] and peak period $T_p = 11$[s] is considered. The wind field will have a turbulence intensity of $\frac{\sigma}{\bar{U}} = 0.02$ [-] and same mean wind speed as for Run 1. Plots of the realization of the wind speed used for calculating the wind thrust force can be seen in Figure 5.15a and 5.15b. Table 5.6 gives a summary of the simulation variables used in the following two simulations.

Combined Loading Variables			
Parameter	Variable	Run1	Run 2
Mean wind speed [m/s]	$\bar{U}$	11	11
Turbulence intensity [-]	$\frac{\sigma}{I}$	0.01	0.02
Thrust coefficient [-]	C_T	0.63	0.63
Significant wave height [m]	H_{m0}	1	5
Peak period [s]	T_p	5	11
Current velocity [m/s]	V_c	1	1
Current drag coefficient [-]	C_d	0.8	0.8
Rotational velocity [rpm]	ω_r	9.6	9.6
Simulation time [s]	T	400	400
Time increment [s]	Δt	0.1	0.1

Table 5.6: Variables used in combined loading response simulations

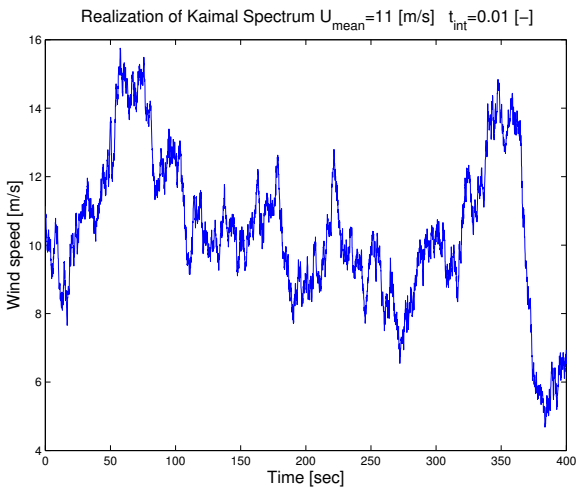

(a) Kaimal specter, Run 1, $\frac{\sigma}{\bar{U}} = 0.01$, $\bar{U} = 11[m/s]$

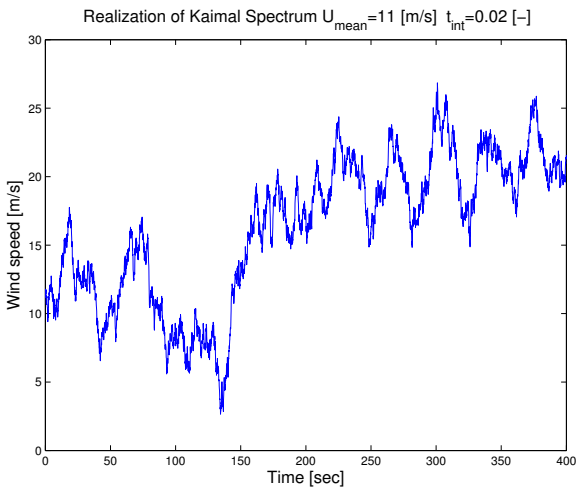

(b) Kaimal, Run 2, $\frac{\sigma}{\bar{U}} = 0.02$, $\bar{U} = 11[m/s]$

Figure 5.15: Realization of the Kaimal spectra used in the combined loading simulation study

5.7.1 Results of Combined Loading Simulations

Run 1: Figure 5.16 show the response plot for the combined loading of run 1. As with the other simulations, the figure show the response of the tower top transversal displacement and velocity as well as the mudline bending moment. The response show a similar response plot as for the turbulent wind simulation as shown in Figure 5.10. However, the response plot shows a more spikes throughout the simulation. As the response for 3P loading was very limited, it is believed that the jagged response comes from including the wave loading.

Run 2: Figure 5.17 show the response plot for the combined loading of run 2. As can be seen from the response plot, the increased amount of turbulence in the wind is contributing to larger fluctuations in the response. It can also be seen that a realization of a wind specter with a high degree of turbulence can give wind speeds of much larger magnitude than the mean wind speed, as can be seen in the large peaks of the tower top displacement, and mudline bending moment.

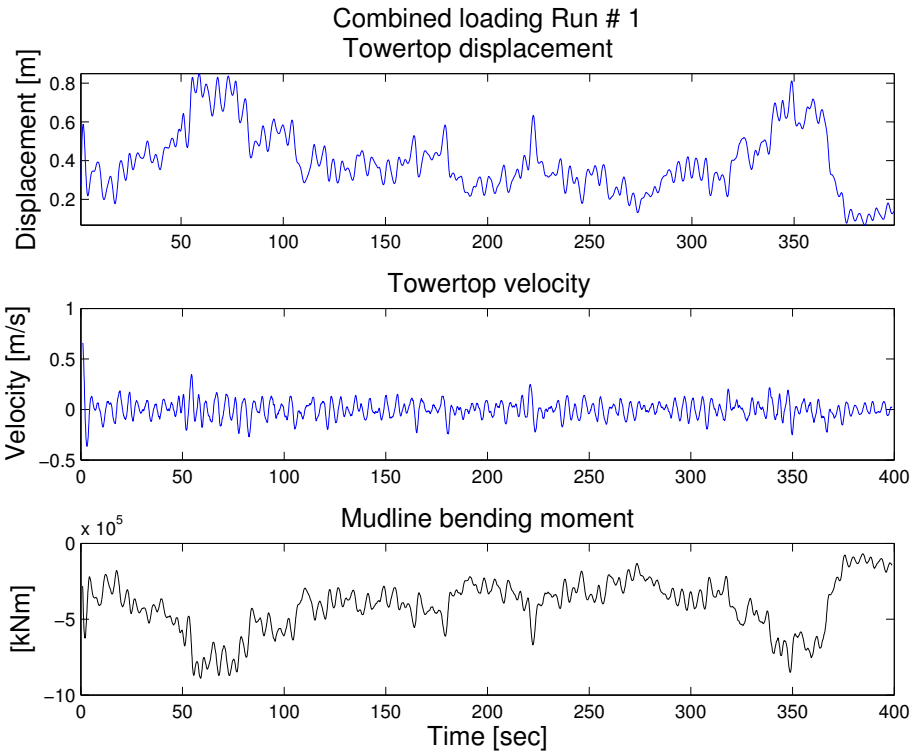

Figure 5.16: Run 1

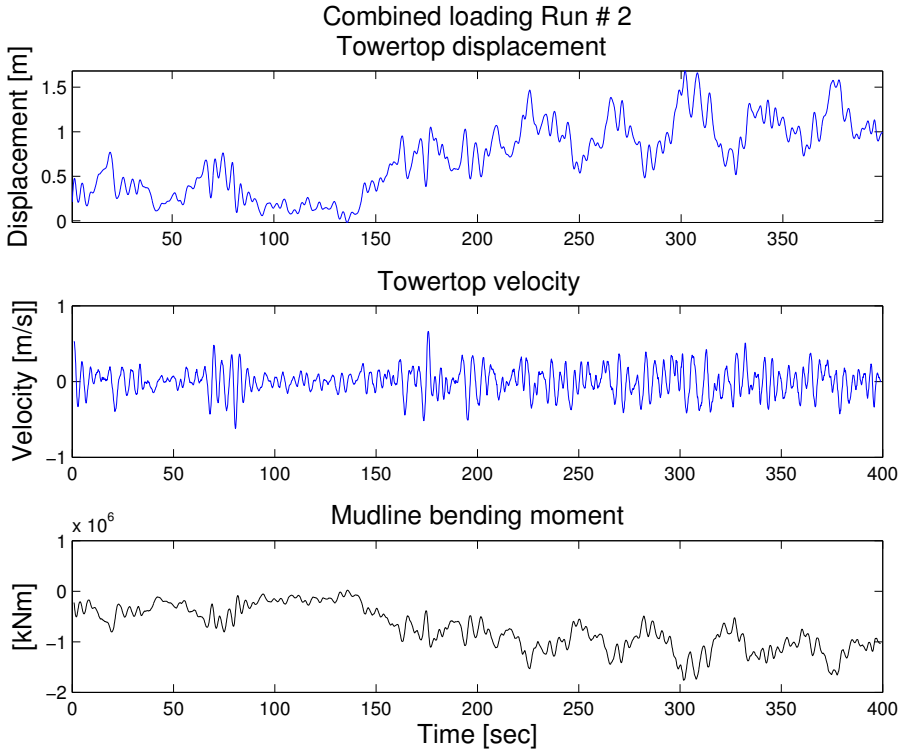

Figure 5.17: Run 2

5.8 Observer Simulations

The accuracy and quality of the designed estimators will be illustrated for various simulations, where the FE model is exposed to different environmental forces. Figure 5.18 give an illustration of the simulation setup. The *input-state* estimator designed in Section 4.2 will be assumed to have transversal acceleration measurements taken at node number 71, 65, 45 and 41, together with transversal displacement measurements at node 71 and 45. The $bias$-based estimator will assume displacement measurements at the same measured nodes as the *input-state* estimator. Node number 58, 26 and the bending moment midway between node 26 and 27 will be the nodal positions which will be attempted estimated. The output measurements are assumed polluted with gaussian white noise. This is modeled by adding noise to the original measurement y_k. The level of intensity will be related to the standard deviation γ of the measured time history multiplied by a intensity factor γ. The total measured signal will then be written as,

$$\bar{y}_k = y_k + \gamma\sigma\mathbf{r}, \tag{5.3}$$

where $\bar{y}_k$ is the polluted measurement signal, y_k is the original unpolluted measurement, and $\mathbf{r} \in \mathbb{R}^{n_y}$ is a random vector drawn from a normal distribution with zero mean and unit standard deviation. γ is chosen as 0.05, corresponding to 5% Gaussian white noise. For the input-state estimator the position of attack for the wind thrust force will be assumed known, and the requirement $rank(\mathbf{J}) = n_p$ is assured. The rest of the environmental forces (waves, current, 3P) will be assumed as process disturbances. For the bias based estimator, the knowledge of position of attack for the different forces is not necessary, as the estimator will not assume any force estimates. Both estimators are represented on reduced modal form using the first six eigenmodes. The simulations will be run for 300 seconds with time increment $\Delta t = 0.1$ [s].

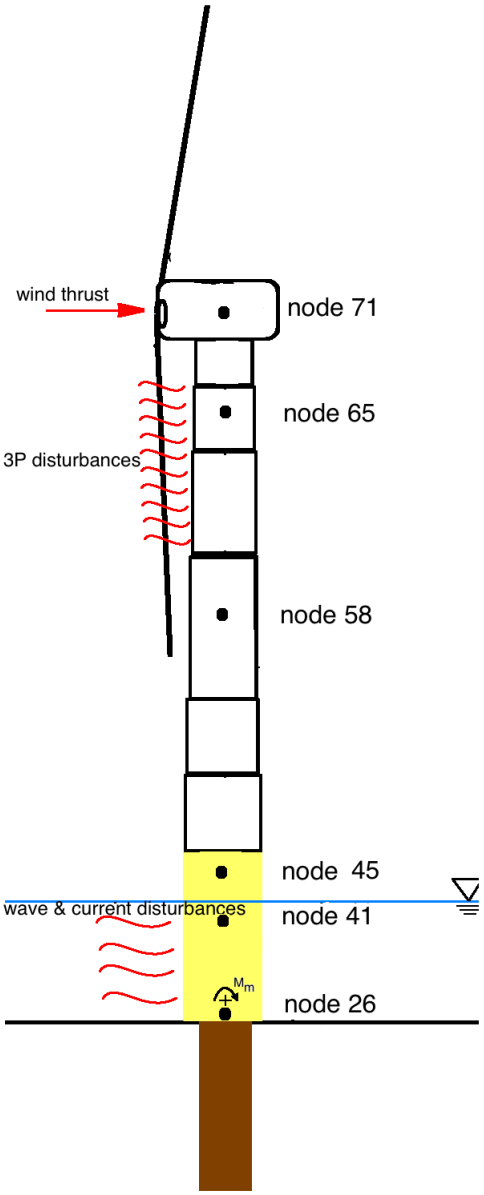

Figure 5.18: Simulation setup for testing estimator performance. Nodes used for measurements 71, 65, 45 & 41. Node number 26 and 58 will be estimated.

5.8.1 Sinusodial Excitation Force

To test the initial performance of the estimators, a simulation with a sinusoidal excitation force of magnitude 10^5 [N] and frequency $\omega = 0.5$ [rad/s] will be performed. The force will be applied at the transversal tower top. The position of the excitation force is assumed known for the $input-state$ estimator. The measurements are taken at the nodes as previously described (see Figure 5.18). The system model will be exposed to weighted gaussian white process noise. As the model is written on modal form, the process noise will be weighted with respect to the overall contribution to response each mode gives. For simplicity, the process noise weighting matrix $\mathbf{W} \in \mathbb{R}^{2n_m \times 2n_m}$ has been chosen as a diagonal matrix containing the entries from the modal input matrix $\Gamma \in \mathbb{R}^{2n_m}$ multiplied by a factor 10.The resulting system model will be,

$$x_{k+1} = \Phi x_k + \Gamma \tau_k + \mathbf{W} w_k, \tag{5.4}$$

$$y_k = \mathbf{C} x_k + v, \tag{5.5}$$

where $\tau_k = 10^5 sin(0.5 t_k)$ is the unknown excitation, and $w_k \in \mathbb{R}^{2n_m}$ is the zero mean gaussian process noise. Measurements and process noise covariance matrices for the $input\text{-}state$ estimator are given as,

$$\mathbf{R} = 10^{-3}\mathbf{I}_{n_y \times n_y},$$
$$\mathbf{Q} = 10^{4}\mathbf{I}_{2n \times 2n}.$$

And for the $bias$ based estimator given as,

$$\mathbf{R} = 10^{-3}\mathbf{I}_{n_y \times n_y},$$
$$\mathbf{Q} = 10^{5}\mathbf{I}_{2n \times 2n}.$$

Initial states and error covariance matrix for both estimators are set to,

$$\mathbf{P}_0^x = 10^{-5}\mathbf{I}_{2n \times 2n},$$
$$\hat{x}_0 = \begin{bmatrix} 0 \\ \vdots \\ 0 \end{bmatrix}.$$

5.8.2 Results from Sinuodial Excitation Force

The results of the state estimation is plotted in terms of total displacements and velocities which can be seen in Figure 5.19 and 5.20.

In top plot of Figure 5.19 one can observe the true time evolution of the transversal displacement of node 58, together with the two estimates. The bottom plot in Figure 5.19 show the transversal velocity of the node. From the top plot one can observe that both estimates are able to follow the true displacement with good precision. The $bias$-based estimator show some spiked behavior at the maxima and minima of the displacement, while the $input\text{-}state$ estimator is showing an almost perfect estimate compared to the true displacement. In the bottom plot of the figure, one can observe that both estimates able to follow the true velocity evolution but with jagged behavior. This suggests that it can be necessary with a velocity measurement to obtain better estimates on the velocity.

Figure 5.20 show the transversal displacement, velocity and bending moment for node 26. In the top plot of the figure showing displacements one can observe that the $input\text{-}state$ estimate is able to follow the true displacement with the same precision as for node 58. On the other hand, the $bias$-based estimate is not showing the same precision. This can also be seen in the bottom plot of the figure. The bottom plot show the interpolated bending moment between node number 26 and 27. In this plot the $input\text{-}state$ estimate is performing well, while the $bias$-estimate is not performing satisfactory. This suggests that the $bias$-estimator is not accurate when estimating nodal values for nodes located far away from nearest measured node. In the middle plot of Figure 5.20 one can observe that the velocity estimate for the $bias$-estimator is performing with approximately the same precision as for node 58. The velocity estimate of the $input\text{-}state$ estimate show a more jagged behavior than for node 58.

Figure 5.21 show the true applied sinusoidal force, and the estimated force. As can be seen, there is a good agreement between the two forces, with no time delay. The avoidance of time delay of the force estimate is due to the $rank(\mathbf{J}) = n_p$ assumption, which makes the estimate matrices directly invertible without a time delay (Maes et al., 2015). The spiked behavior in the force estimate is due to the corrective force it will have when process disturbances is present.

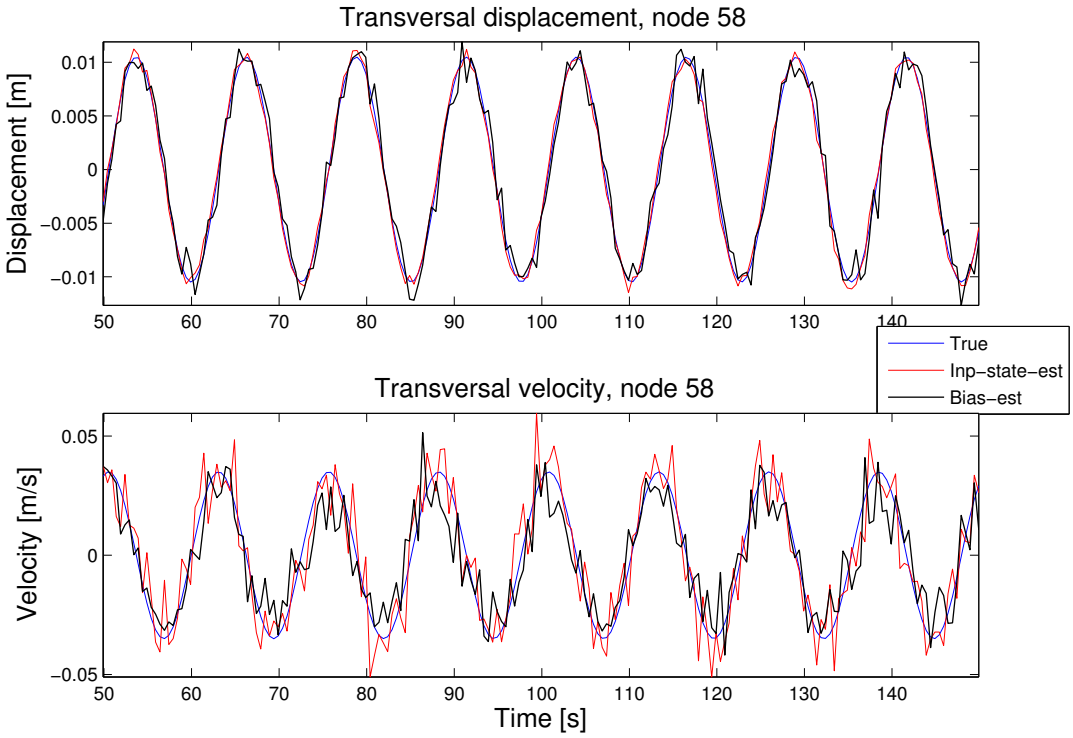

Figure 5.19: Transversal displacement and velocity estimate of node number 58 subjected to sinusoidal excitation

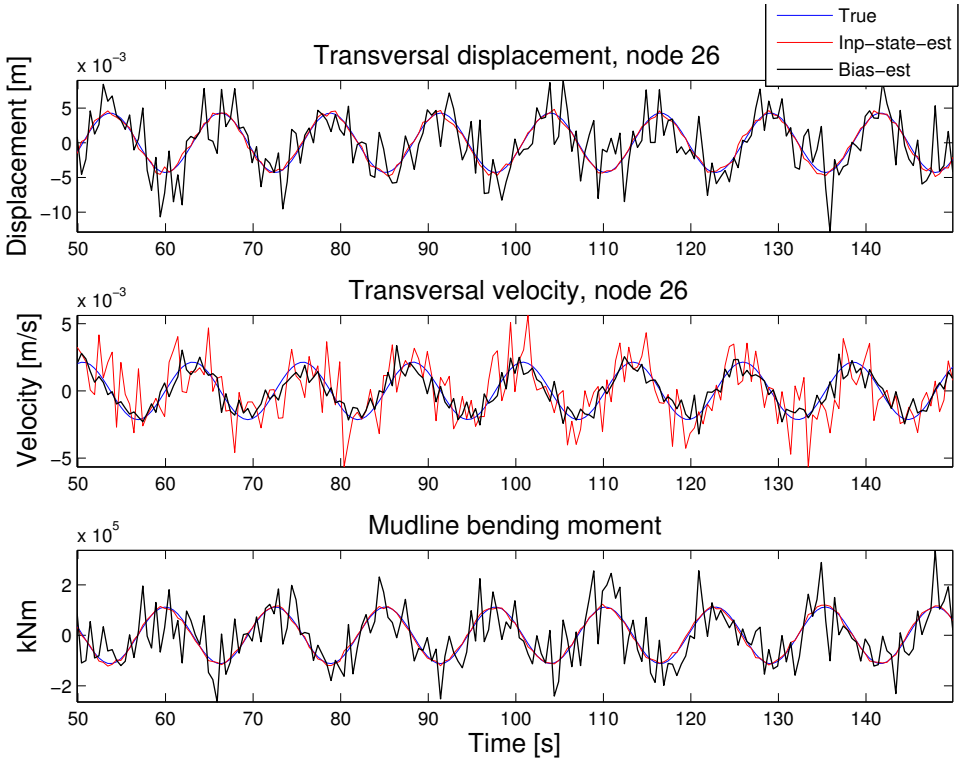

Figure 5.20: Transversal displacement, velocity and bending moment estimate of node number 26 subjected to sinusoidal excitation

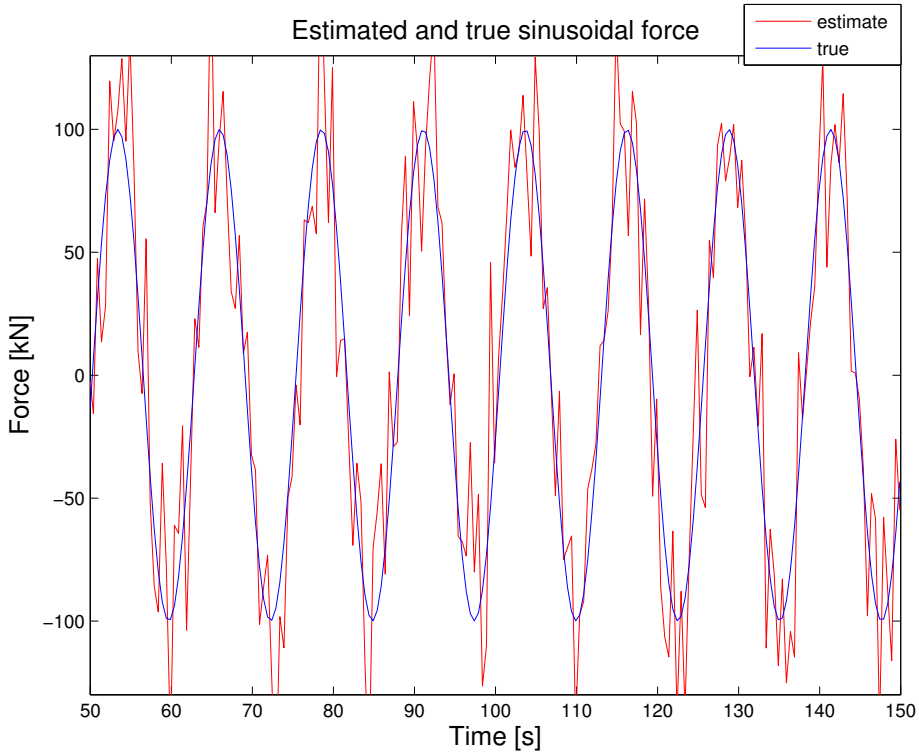

Figure 5.21: True and estimated sinusoidal excitation force

5.8.3 Operating Condition Simulation

As the estimators models showed relatively good results for the sinusoidal excitation force and weighted process noise, a scenario where the FE model is subjected to environmental forces from wind, waves, 3P and current will be tested. The environmental forces will be assumed as process disturbances. The point of attack for the wind thrust is assumed to be known to the $input\text{-}state$ estimator, such that a force estimate will be applied at the same position as the wind thrust force. To improve the state estimates compared to the previous sinusoidal excitation simulation, an additional displacement measurement at node 34 will be available for the $bias$-estimate. This additional measurement will be used for improving the estimated states of node 26. The rest of the simulation setup will be as presented in the introductory part. The simulated scenario can be viewed on as a "operating" condition environment, where the parameters deciding the loading conditions can be seen in Table 5.7.

Normal operating condition variables		
Mean wind speed [m/s]	$\bar{U}$	9
Turbulence intensity [-]	$\frac{\sigma}{\bar{U}}$	0.02
Thrust coefficient [-]	C_T	0.53
Significant wave height [m]	H_{m0}	1
Peak period [s]	T_p	5
Current velocity [m/s]	V_c	1
Current drag coefficient [-]	C_d	0.8
Rotational velocity [rpm]	ω_r	9.6
Simulation time [s]	T	300
Time step [s]	Δt	0.1

Table 5.7: Variables used in estimation simulation of a typical operating condition environment.

Initial measurements and process noise covariance matrices for the $input\text{-}state$ estimator are given as

$$\mathbf{R} = 10^{-3}\mathbf{I}_{n_y \times n_y},$$
$$\mathbf{Q} = 10^{4}\mathbf{I}_{2n \times 2n}.$$

And for the $bias$ based estimator given as,

$$\mathbf{R} = 10^{-3}\mathbf{I}_{n_y \times n_y},$$
$$\mathbf{Q} = 10^{5}\mathbf{I}_{2n \times 2n}.$$

Initial states and error covariance matrix for both estimators are set to,

$$\mathbf{P}_0^x = 10^{-5}\mathbf{I}_{2n \times 2n},$$
$$\hat{x}_0 = \begin{bmatrix} 0 \\ \vdots \\ 0 \end{bmatrix}.$$

5.8.4 Results of Operating Condition Simulation

The plotted results in the interval 50-150 seconds for the displacement and velocities of the unmeasured nodes 58 and 26 can be seen in Figure 5.22 and 5.23. In the top plot of Figure 5.22 one can observe that both estimators are able to estimate the displacement with very good precision throughout the simulation. The $bias$-based estimator show some jagged behavior at the local maxima and minima, as it did for the sinusoidal excitation simulation. In the bottom part of Figure 5.22 one can see the transversal velocity estimates of the of node 58. As for the displacement estimates, both estimates are able to follow the true velocity in a relatively good manner. The plot shows that the $bias$ based estimate is better at obtaining a less fluctuating estimate of the velocity of this node than the $input\text{-}state$ estimate.
In the top plot of Figure 5.23 one can see the estimated and true displacement of node 26. The plot shows that the added measurement for the $bias$-estimate is greatly improving the displacement estimate. The $input\text{-}state$ estimate is as for the displacement estimate for node 58 following the true displacement with great precision.
The estimated bending moment between node 26 and 27 shown in the bottom plot of Figure 5.23 show some improvement for the $bias$-estimate compared to the sinusoidal excitation simulation, however there are still room for improvement. The $input\text{-}state$ estimate is following the true bending moment with good precision. In the middle plot of Figure 5.23, the velocity estimates show that the $bias$-estimate is performing very well, as it did for node 58. On the other hand, the $input\text{-}state$ estimate show less precision than for node 58.

In Figure 5.24 one can observe the estimated forces applied to the $input\text{-}state$ estimator.The plot shows that the input estimate is able to estimate the wind thrust input with good accuracy. The jagged behavior is due to the corrective behavior the input estimate has to have.

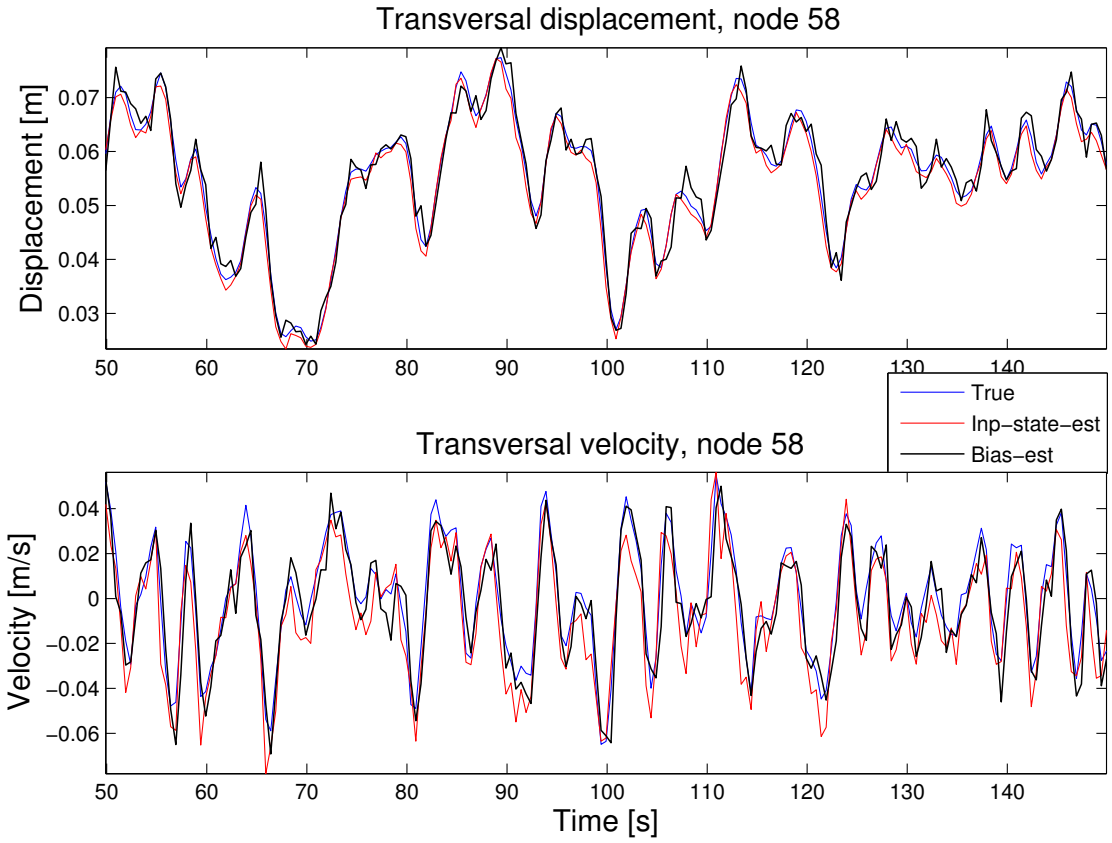

Figure 5.22: Estimated displacement and velocity response for node number 58 under operating condition.

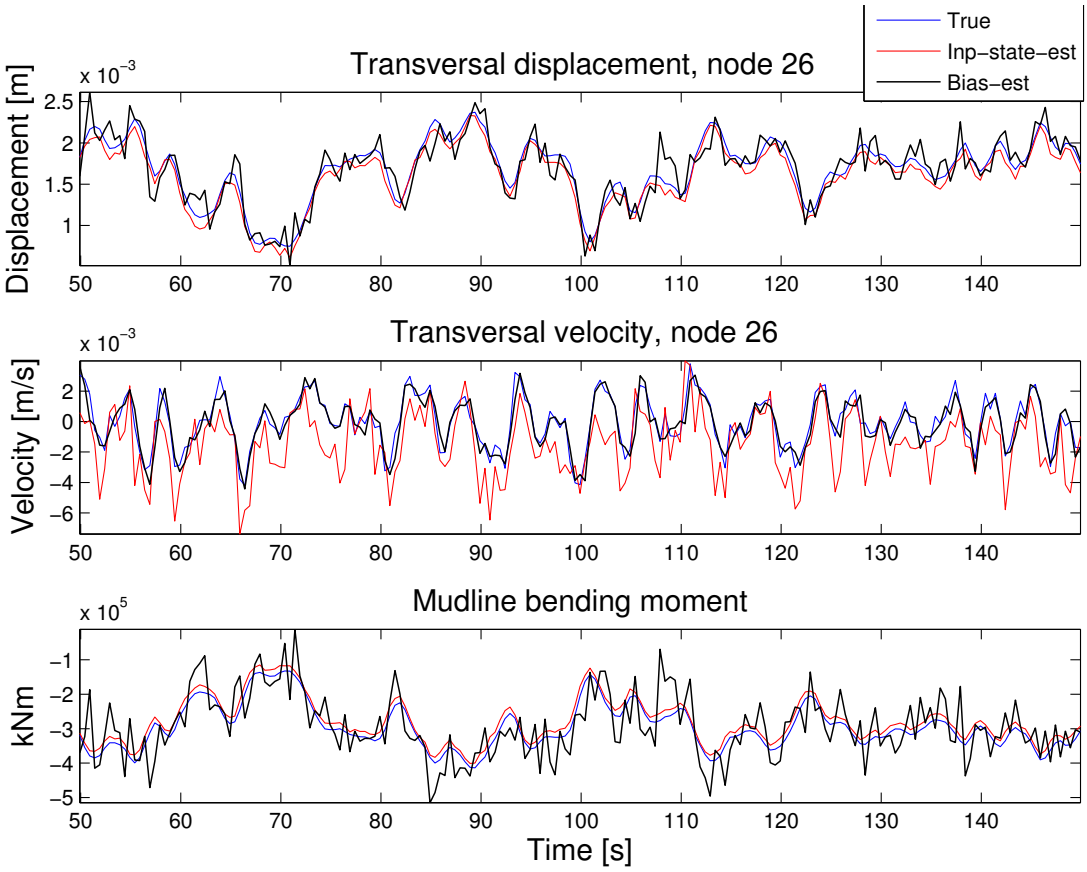

Figure 5.23: Estimated displacement, velocity and bending moment response for node number 26 under operating condition.

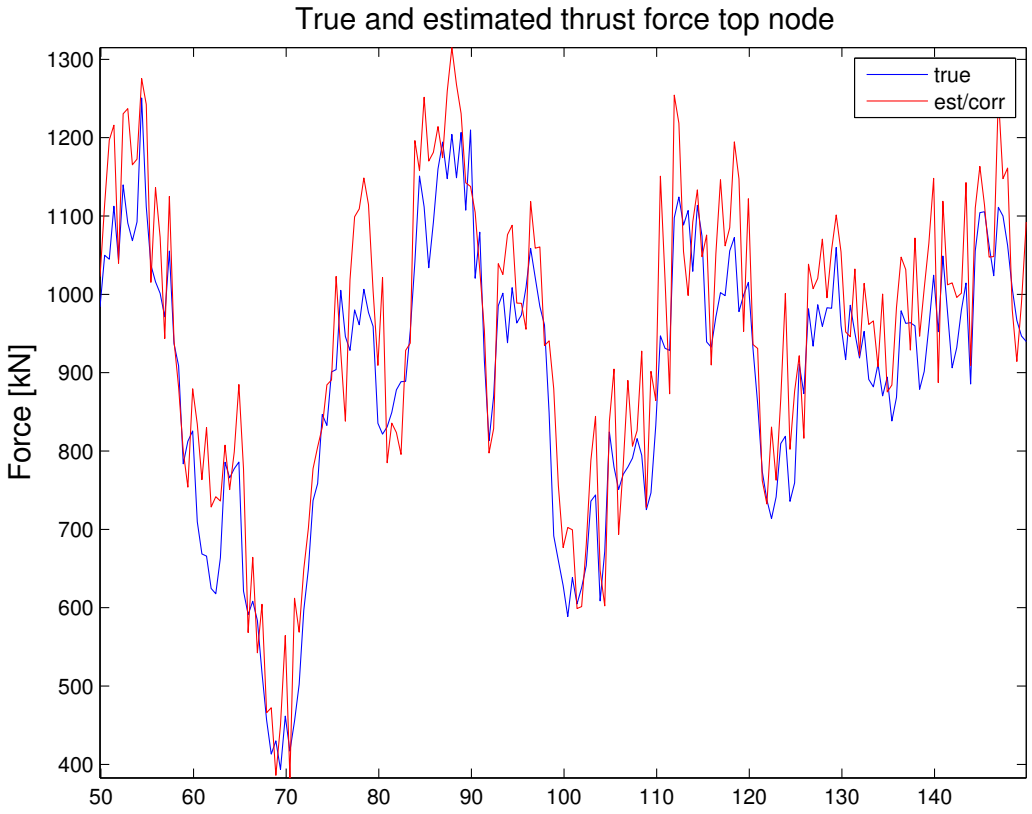

Figure 5.24: Comparison of true wind thrust force and corrective force applied to top node.

5.8.5 High Wave Condition Simulation

As the process disturbances can increase to a significant amount for sea states and wind with considerable amount of energy, it is of interest to test the estimator's performance in a scenario where the process disturbances are of a larger magnitude. In this scenario the wind speed will be at 13 m/s and at a higher turbulence rate. The sea state will have a significant wave height of $H_{m0} = 7$ m and peak period $T_p = 11$ sec. The measurement setup will be as given in the introductory section, where in addition a measurement at node 34 will available for the $bias$-estimate. Initial measurements and process noise covariance matrices for the $input\text{-}state$ estimator are given as,

$$\begin{aligned}\mathbf{R} &= 10^{-3}\mathbf{I}_{n_y \times n_y},\\ \mathbf{Q} &= 10^{4}\mathbf{I}_{2n \times 2n}.\end{aligned}$$

And for the $bias$ based estimator given as,

$$\begin{aligned}\mathbf{R} &= 10^{-3}\mathbf{I}_{n_y \times n_y},\\ \mathbf{Q} &= 10^{5}\mathbf{I}_{2n \times 2n}.\end{aligned}$$

Initial states and error covariance matrix for both estimators are set to,

$$\begin{aligned}\mathbf{P}_0^x &= 10^{-5}\mathbf{I}_{2n \times 2n},\\ \hat{x}_0 &= \begin{bmatrix} 0 \\ \vdots \\ 0 \end{bmatrix}.\end{aligned}$$

5.8.6 Results of High Wave Condition Simulation

Figure 5.25 and 5.26 show the simulation results for the estimated values of nodes 58 and 26 respectively. The plots show much of the same behavior as for the operating condition simulation. Top plot of Figure 5.25 and 5.26 both show that the two estimators are able to estimate the displacement in a good manner even when the effect of disturbances are higher. The $bias$-estimator do however show signs of more jagged behavior in its estimate for displacements than it did the operating condition. As before, one can observe from the middle plots of the respective figures that the $bias$-based estimator is outperforming the $input\text{-}state$ estimator in velocity estimates, while for the interpolated bending moment, one can see from the bottom plot of Figure 5.26 that the $input\text{-}state$ estimator is outperforming the $bias$-based estimator, which is following the trend of the bending moment but with a jagged behavior. Averaging the bending moment estimate might yield a better approximation to the true bending moment.

Figure 5.27 show the estimated input force used by the $input\text{-}state$ estimate. As for the operating condition simulation, the force estimate is able to follow the dominant wind thrust force in its estimation. Where the jagged behavior comes from the corrective force behavior due to

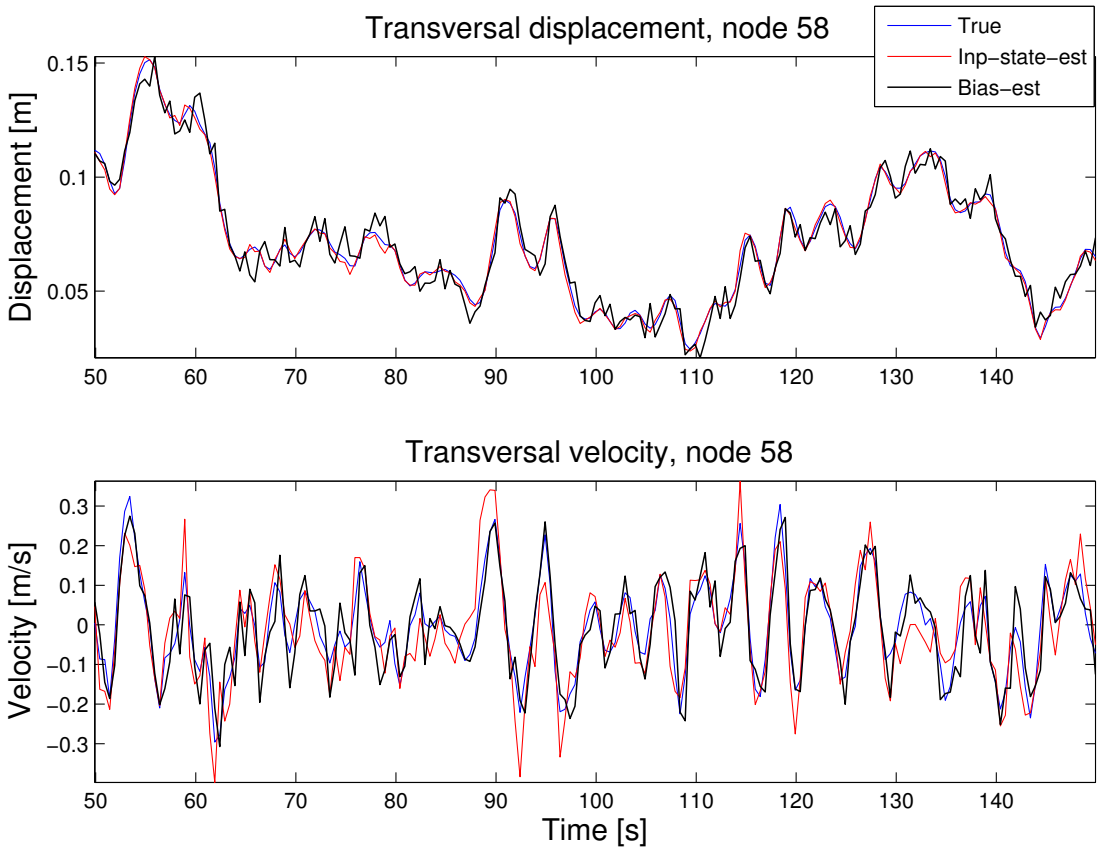

Figure 5.25: True and estimated nodal displacements and velocity at node 58 for a high wave condition.

the unmodeled dynamics.

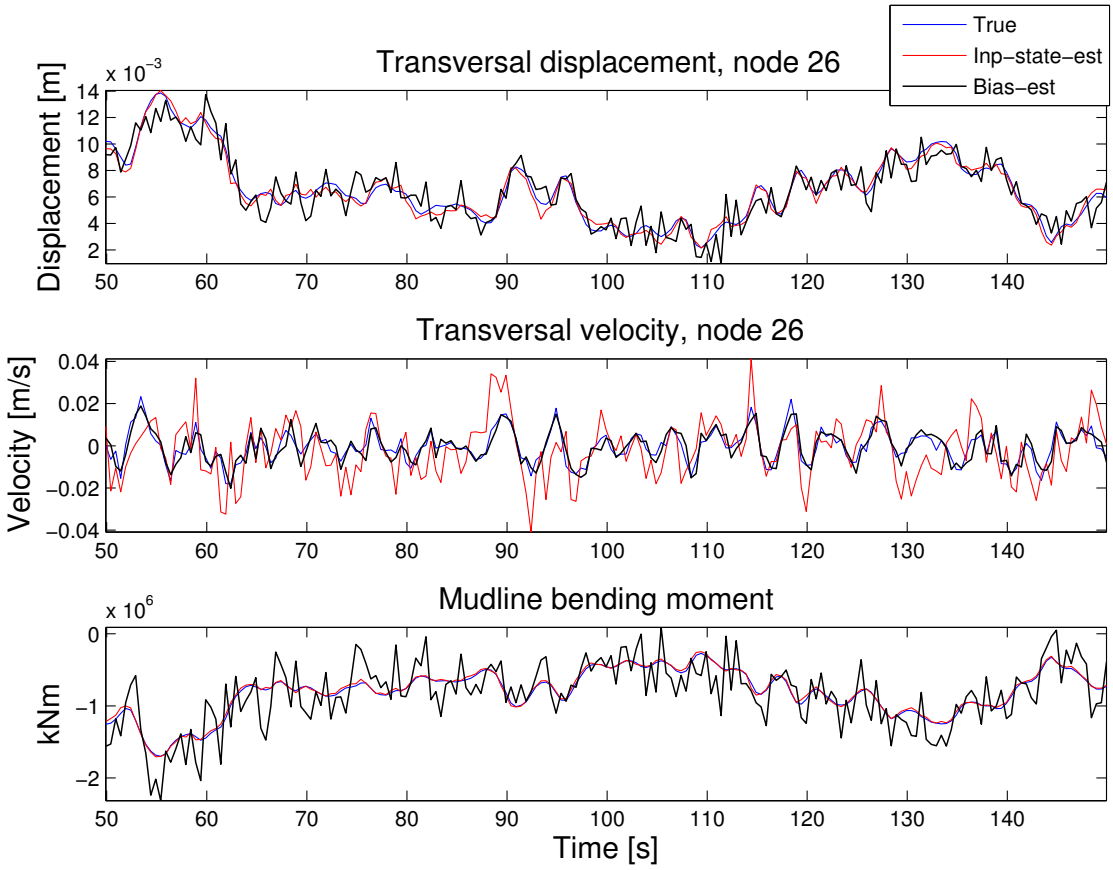

Figure 5.26: True and estimated nodal displacements and velocity at node 26 for a high wave condition.

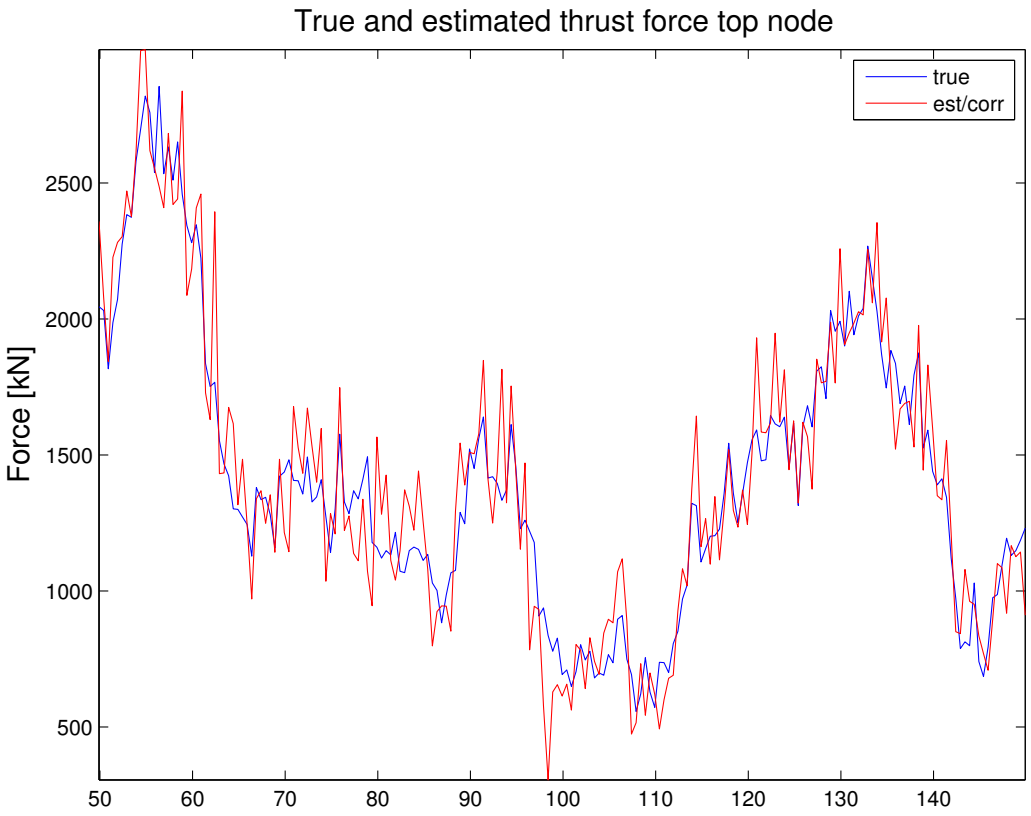

Figure 5.27: True wind thrust force and corrective force estimate applied at node 71.

5.8.7 Modeling Error Simulation

Simulations until now have only considered a perfect matching between the estimator models and the system model, where the discrepancies between estimator states and system states stem from the process disturbances, and measurement error. To check the robustness of the estimators beyond process disturbances, the following simulation will consider an estimator model with discrepancies between the system model and the estimator model. The amount of elements between the estimator and system models will be maintained, but with a change in the inertia, stiffness and damping matrices. The new inertia $\bar{\mathbf{M}}$, stiffness $\bar{\mathbf{K}}$ and damping matrices $\bar{\mathbf{D}}_\mathbf{b}$ are chose based on section 4.4, where chosing $\delta_1 = 0.11$, $\delta_2 = -0.15$ and $\delta_3 = 0.04$ yields the new matrices

$$\begin{aligned}\bar{\mathbf{M}} &= \mathbf{M} + \delta_1 \mathbf{M},\\ \bar{\mathbf{K}} &= \mathbf{K} + \delta_2 \mathbf{K},\\ \bar{\mathbf{D}}_\mathbf{b} &= \mathbf{D}_\mathbf{b} + \delta_3 \mathbf{D}_\mathbf{b}.\end{aligned}$$

The new estimator model will then have a 14.3% reduction in natural frequencies for all modes compared to the system model. The simulation parameters will be as in Table 5.7 which are the same parameters used in the simulation for the normal operating condition simulation. As before the measurements are corrupted with 5% gaussian white measurement noise. Initial measurements and process noise covariance matrices for the $input\text{-}state$ estimator are given as,

$$\begin{aligned}\mathbf{R} &= 10^{-3}\mathbf{I}_{n_y \times n_y},\\ \mathbf{Q} &= 10^{4}\mathbf{I}_{2n \times 2n}.\end{aligned}$$

And for the $bias$ based estimator given as,

$$\begin{aligned}\mathbf{R} &= 10^{-3}\mathbf{I}_{n_y \times n_y},\\ \mathbf{Q} &= 10^{5}\mathbf{I}_{2n \times 2n}.\end{aligned}$$

Initial states and error covariance matrix for both estimators are set to,

$$\begin{aligned}\mathbf{P}_0^x &= 10^{-5}\mathbf{I}_{2n \times 2n},\\ \hat{x}_0 &= \begin{bmatrix} 0 \\ \vdots \\ 0 \end{bmatrix}.\end{aligned}$$

5.8.8 Results of Modeling Error Simulation

Figure 5.28 and 5.29 show the results of the true and estimated transversal displacement and velocities for node 58 and 26 respectively, when being subjected to modeling errors.
From the top plot of Figure 5.28 one can observe that the state estimates are still able to follow the true displacement of node 58 with good precision. The $input\text{-}state$ estimator is showing almost as good precision as done for the estimates with out modeling errors. The $bias$-based estimate show a more fluctuating estimate, but is still able to follow the trends of the displacement. For the velocity estimate in the bottom part of Figure 5.28 one can observe that the $bias$-based estimate is obtaining a relatively accurate estimate of the velocity, as in the simulations with out modeling error. The $input\text{-}state$ estimate however is showing more fluctuations than with out modeling errors, but have an overall satisfactory behavior.

In the top plot of Figure 5.29 one can observe much of the same pattern for the displacements of node 26 as for node 58, where the $input\text{-}state$ estimate is showing an excellent behavior, and the $bias$-based estimate follow the trend, but with more fluctuations than previous simulations. In the middle plot the difference in the estimates for transversal velocity of node 26 is more visible. Here the $input\text{-}state$ estimate is fluctuating even more than for node 58, while the $bias$-based estimate is showing much the same behavior as for node 58. The interpolated bending moment shown in bottom plot of Figure 5.29 show a very good agreement between the $input\text{-}state$ estimate and the true model. This is as expected, as the plots for displacement showed a good agreement on displacement estimates.
For the $bias$-based estimate, the performance is as for the high sea state simulation not satisfactory, as the fluctuations in the bending moment estimate are quite large. If the estimate was used for fatigue estimation, the $bias$-based estimate would have shown too large fluctuations in the bending moment, leading to overestimating an eventual fatigue damage estimation.

Figure 5.30 show that the force estimate at the top node is no longer at the same magnitude as the wind thrust force. One can also observe larger fluctuations in the estimate. The difference in magnitude between them is linked to the decreased overall stiffness in the estimator model of the structure, leading to a smaller force magnitude needed to obtain the same measured response as the true measurements.

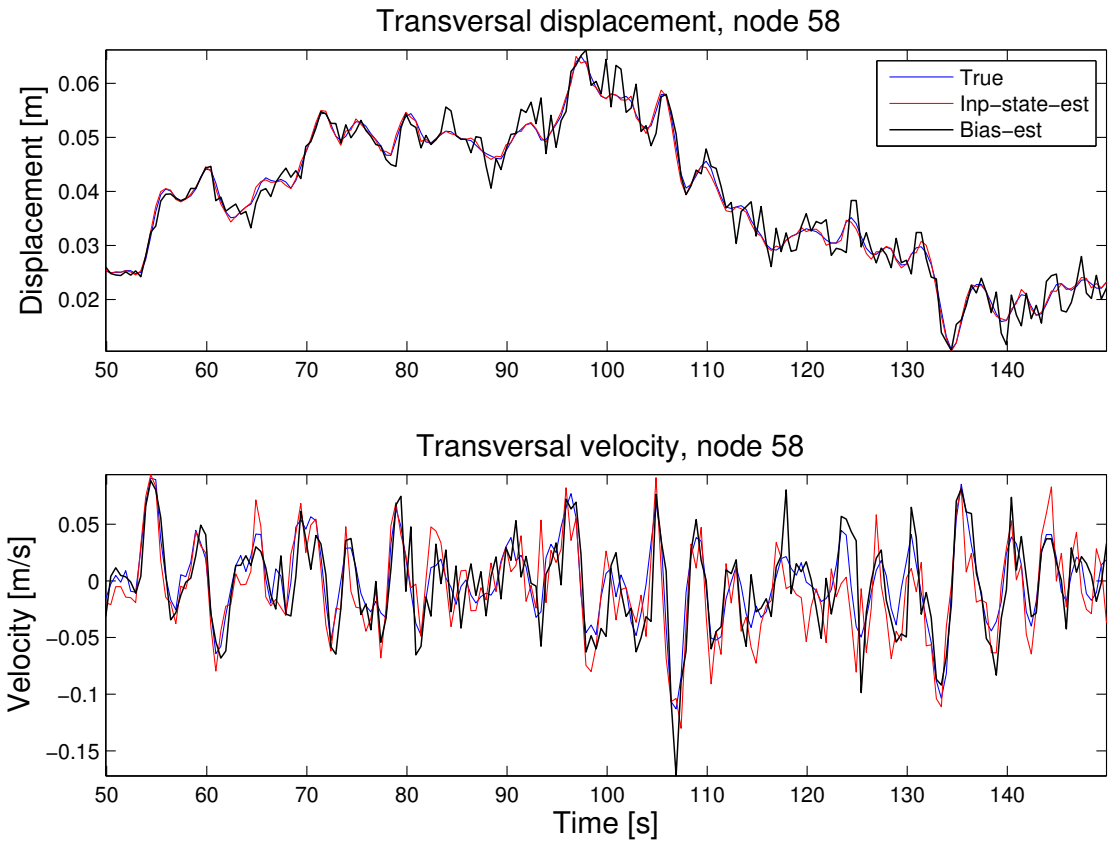

Figure 5.28: True and estimated states displacements for node 58 with modeling errors

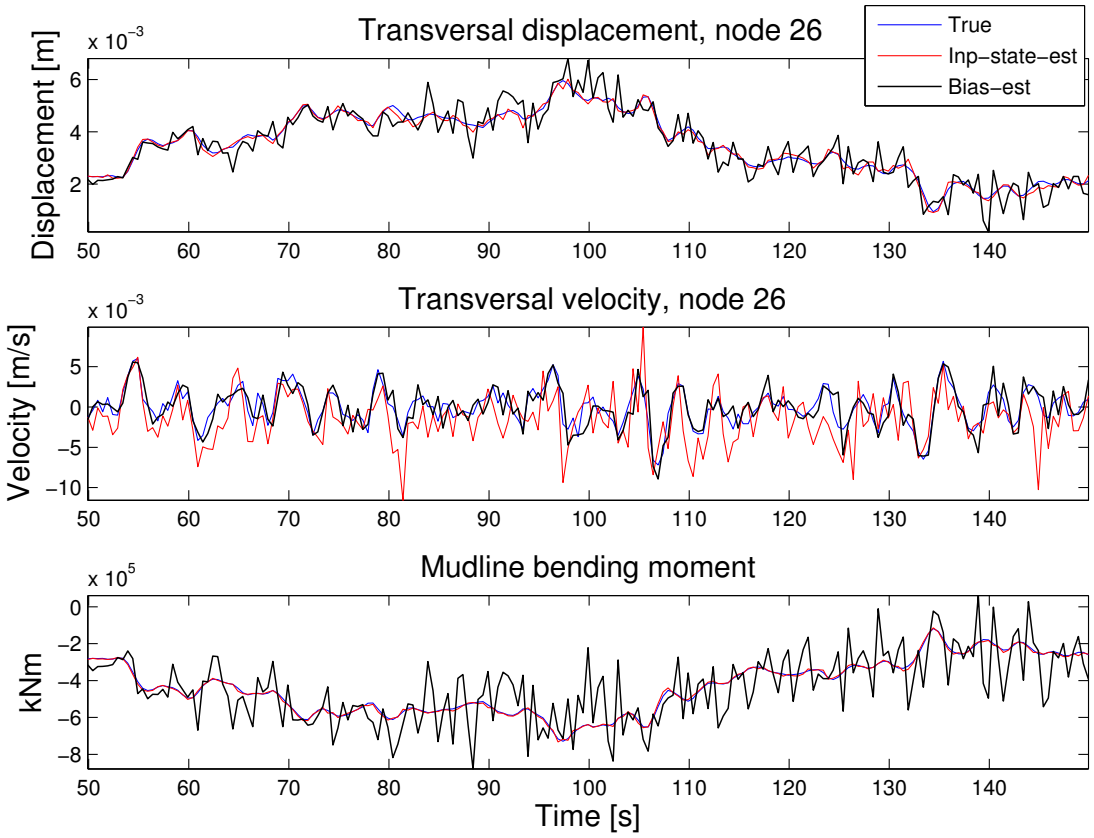

Figure 5.29: True and estimated states displacements for node 26 with modeling errors

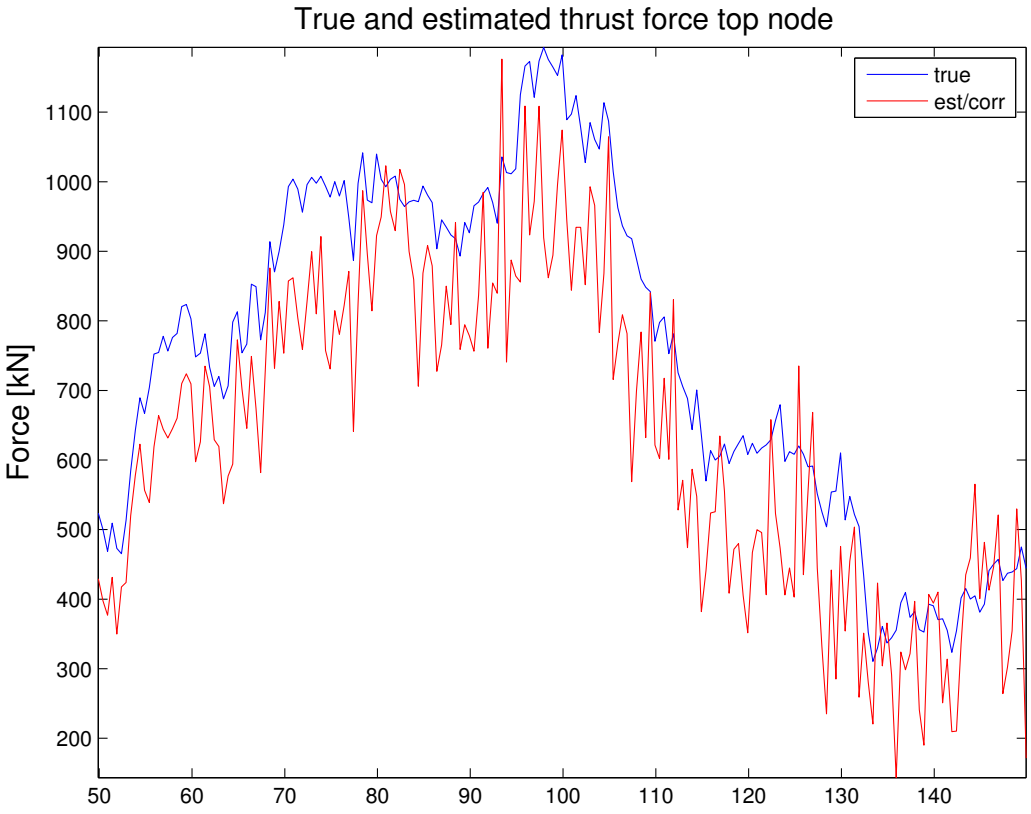

Figure 5.30: True wind thrust force and corrective force estimate applied at node 71 for simulation with modeling errors

5.9 Summarizing Discussion

Through out this chapter different simulations have been run, with aim to get a better understanding on the response picture for the modeled structure and the behavior of the modeled estimator models. In the structure response simulations it was seen that the wind thrust force was by far the most dominant force contribution, and that force from current and rotor-tower interaction was not profound. The wave loading did not give large effects on the displacement, but did give the cyclical loading pattern which is important for fatigue considerations. Both estimator models showed a satisfactory behavior in estimating the unmeasured nodal values, even in the presence of relatively large modeling errors. The $bias$-based estimator did show signs of large fluctuations in the estimated bending moment in presence of modeling errors. It is suggested that this could be improved by either proper tuning of bias variables and the process noise covariance matrix, or by increasing the number of measurements. When it comes to extending the model to include additional degrees of freedom, it is seen as possible to maintain the design of the estimator's, but expanding them to eventually include mode shapes for additional DOFs. Including more DOFs will enable to get a better picture of the true nature of the response a OWT will experience. Especially including a rotational degree of freedom about the longitudinal $z-axis$ can be important, as the effect of imbalanced loading on the turbine blades can lead to significant torsion on the structure.

The designed model and environmental forces modeled in this thesis does have limitations on its validity, which should be addressed. First and foremost, it has been assumed a fully linear relationship between response and loading. This is a well known simplification of the true nature, as both the structure and the environmental forces does experience many coupled and nonlinear phenomena. For instance, the wave loading scenarios will certainly have nonlinear wave forces from e.g. sum frequency and mean wave drift forces which will contribute to a loading, on the structure. The assumption on linear behavior in displacements, and strain will restrict the applied forces to be within a certain range such that the obtained displacements obey the assumption of linear elastic behavior and the other assumptions which need to be valid when applying Euler Bernoulli beam theory.

Chapter 6

Concluding Remarks

In the concluding remarks a conclusion on the findings and work done in this thesis is presented. Proposals for further work on improving and validating the designed systems is also addressed.

6.1 Conclusion

This thesis has designed a simplified low fidelity FE model of the 10MW DTU reference turbine structure, and modeled the most dominant environmental forces acting on the structure. The simulations of the model exposed to the different forces have given a good insight into the response picture of the structure. Simulations showed that the wind thrust force was dominating the overall response of the structure, and that the effect of rotor-tower interaction forces on response was not as large as first anticipated. It can however be an import contributor to fatigue damage due to its cyclical loading pattern and for future turbines of larger design, where the second bending mode will tend to get lower and possibly interact with the rotational frequency of the rotor. The designed model with the corresponding structural state estimators has given a good foundation for further work on designing a turbine control system where the structural response can be taken into account or to design a fatigue damage estimator.

The two designed estimators showed good performance in estimating the unmeasured nodal states when subjected to the unmeasured environmental forces from wind, waves, 3P loading and current. From the simulations it was shown that both estimators performed well when the estimator system dynamics matched the system model, and when discrepancies was introduced to the estimator models in form of changing their inertia, stiffness and damping matrix. Comparing the two estimators, simulations showed that the $bias$-based estimator was outperforming the $input\text{-}state$ estimator in velocity estimates. On the other hand it did show a more fluctuating behavior on the displacement estimates. In addition, it was shown that in case for the $bias$-estimator to perform satisfactory it was necessary to have measurements at nodes located relatively close by to the estimated nodes. On the estimation of bending moment, the $bias$-estimator showed a fluctuating behavior which is assumed to be due to the interpolation of two unmeasured nodes, which both combined increase the level of fluctuations. The $input\text{-}state$ estimator did an excellent job on estimating both displacements and bending moment.

Comparing the complexity of the two designs together one can conclude that the $bias$-based estimator is a simpler design which performed satisfactory if having enough measurements. The simplicity comes from the fact that very little knowledge about the unmeasured environmental loadings are necessary for the estimator to perform on a satisfactory level. The $input\text{-}state$ estimator though more complex showed outstanding results in estimating the displacements and bending moment. It was also able to give a good estimate on the wind thrust force, as it was the dominant environmental force.

6.2 Proposal on Further Work

In further work it will be of interest to test the model against a more refined FE model designed in a commercially available finite element program. By using that model as a process plant model one will be able to verify the findings of this work, and outline improvements that can be made. Another point which will be of interest is to expand the state estimator to calculate accumulated fatigue damage over a long period when being run in parallel with a process plant model from a state of the art simulation program. Implementing the state estimates in a turbine control system is also of interest, as this can possibly give valuable information for more advanced control system, prolonging the lifetime of an OWT, by reducing the inflicted fatigue damage.

Bibliography

László Arany, Subhamoy Bhattacharya, John Macdonald, and S John Hogan. Simplified critical mudline bending moment spectra of offshore wind turbine support structures. *Wind Energy*, 2014.

C Bak, R Bitsche F Zahle, and P B Andersen T Kim. Design and performance of a 10 mw wind turbine. *J. Wind*, November 2014. URL http://dtu-10mw-rwt.vindenergi.dtu.dk/.

Hyung-joon Bang, Suk-whan Ko, Moon-seok Jang, and Hong-il Kim. Shape estimation and health monitoring of wind turbine tower using a fbg sensor array. In *Instrumentation and Measurement Technology Conference (I2MTC), 2012 IEEE International*, pages 496–500. IEEE, 2012.

Dennis S Bernstein. *Matrix mathematics: theory, facts, and formulas*. Princeton University Press, 2009.

P.A. Brodtkorb, P. Johannesson, G. Lindgren, I. Rychlik, J. Rydén, and E. Sjö. WAFO - a Matlab toolbox for the analysis of random waves and loads. In *Proc. 10'th Int. Offshore and Polar Eng. Conf., ISOPE, Seattle, USA*, volume 3, pages 343–350, 2000.

CP Butterfield, W Musial, and J Jonkman. Overview of offshore wind technology. In *Presentation at the Chinese Renewable Energy Industry Association WindPower Conference, Shanghai, China*, 2007.

Marloes Caduff, Mark AJ Huijbregts, Hans-Joerg Althaus, Annette Koehler, and Stefanie Hellweg. Wind power electricity: the bigger the turbine, the greener the electricity? *Environmental science & technology*, 46(9):4725–4733, 2012.

Aron Caselunghe and Jonas Eriksson. Structural element approaches for soil-structure interaction. 2012.

Climate Change. Mitigation of climate change. *Summary for Policymakers. IPCC*, 2007.

Chia Chen Ciang, Jung-Ryul Lee, and Hyung-Joon Bang. Structural health monitoring for a wind turbine system: a review of damage detection methods. *Measurement Science and Technology*, 19(12):122001, 2008.

Robert D Cook et al. *Concepts and applications of finite element analysis*. John Wiley & Sons, 2007.

Mads Damgaard, Jacob KF Andersen, Lars Bo Ibsen, and Lars V Andersen. Natural frequency and damping estimation of an offshore wind turbine structure. In *Proceedings of the 22nd international offshore and polar engineering conference, Rhodes, Greece*, 2012.

Odd Faltinsen. *Sea loads on ships and offshore structures*, volume 1. Cambridge university press, 1993.

Jacob Fish and Ted Belytschko. *A first course in finite elements*. John Wiley & Sons, 2007.

Thor I Fossen. *Handbook of marine craft hydrodynamics and motion control*. John Wiley & Sons, 2011.

Claus-Peter Fritzen, Peter Kraemer, and Maksim Klinkov. An integrated shm approach for offshore wind energy plants. In *Structural Dynamics, Volume 3*, pages 727–740. Springer, 2011.

Peter Frohboese, Christian Schmuck, and GL Garrad Hassan. Thrust coefficients used for estimation of wake effects for fatigue load calculation. In *European Wind Energy Conference*, pages 1–10, 2010.

Steven Gillijns and Bart De Moor. Unbiased minimum-variance input and state estimation for linear discrete-time systems. *Automatica*, 43(1):111–116, 2007.

Martin OL Hansen. *Aerodynamics of wind turbines*. Routledge, 2013.

GL Garrad Hassan. A guide to uk offshore wind operations and maintenance. *Scottish Enterprise and the Crown Estate*, 2013.

Melanie Hau. Promising load estimation methodologies for wind turbine components. Technical report, Institut für Solare Energieversorgungstechnik (ISET), 2006.

PA Joosse, MJ Blanch, AG Dutton, DA Kouroussis, TP Philippidis, and PS Vionis. Acoustic emission monitoring of small wind turbine blades. *Journal of solar energy engineering*, 124(4): 446–454, 2002.

Christoph Kost and JN Mayer. Levelized cost of electricity renewable energy technologies. *Fraunhofer Institute for Solar Energy Systems ISE*, 2013.

Germanischer Lloyd. Overall damping for piled offshore support structures,guideline for the certification of offshore wind turbines. *WindEnergie*, 2005.

E Lourens, Costas Papadimitriou, and Steven Gillijns. Joint input-response estimation for structural systems based on reduced-order models and vibration data from a limited number of sensors. *Mechanical Systems and Signal Processing*, 29:310–327, 2012.

Kristof Maes, E Lourens, Katrien Van Nimmen, Edwin Reynders, Guido De Roeck, and Geert Lombaert. Design of sensor networks for instantaneous inversion of modally reduced order models in structural dynamics. *Mechanical Systems and Signal Processing*, 52:628–644, 2015.

J.K Vandiver M.F Cook. Measured and predicted dynamic response of a single pile platform to random wave excitation. *Offshore Technology Conference report*, 4285, 1982.

Chris Paige. Properties of numerical algorithms related to computing controllability. *Automatic Control, IEEE Transactions on*, 26(1):130–138, 1981.

Costas Papadimitriou, Claus-Peter Fritzen, Peter Kraemer, and Evangelos Ntotsios. Fatigue predictions in entire body of metallic structures from a limited number of vibration sensors using kalman filtering. *Structural Control and Health Monitoring*, 18(5):554–573, 2011.

Trevor J Price. James blyth–britain's first modern wind power pioneer. *Wind engineering*, 29(3): 191–200, 2005.

Craig M Risien and Dudley B Chelton. A global climatology of surface wind and wind stress fields from eight years of quikscat scatterometer data. *Journal of Physical Oceanography*, 38 (11):2379–2413, 2008.

Niels Jacob Tarp-Johansen, Lars Andersen, Erik Damgaard Christensen, Christian Mørch, B Kallesøe, and Sten Frandsen. Comparing sources of damping of cross-wind motion. *European Offshore Wind*, 2009.

Knut Torsethaugen, Turid Faanes, and Sverre Haver. Characteristics for extreme sea states on the norwegian continental shelf. Technical report, 1985.

P Van der Male and E Lourens. Operational vibration-based response estimation for offshore wind lattice structures. In *Structural Health Monitoring and Damage Detection, Volume 7*, pages 83–96. Springer, 2015.

J Van der Tempel, MB Zaaijer, and H Subroto. The effects of scour on the design of offshore wind turbines. In *Proceedings of the 3rd International conference on marine renewable energy Marec*, pages 27–35, 2004.

WG Versteijlen, A Metrikine, JS Hoving, EH Smidt, and WE De Vries. Estimation of the vibration decrement of an offshore wind turbine support structure caused by its interaction with soil. In *Proceedings of the EWEA Offshore 2011 Conference, Amsterdam, The Netherlands, 29 November-1 December 2011*. European Wind Energy Association, 2011.

WG Versteijlen, KN Van Dalen, AV Metrikine, and L Hamre. Assessing the small-strain soil stiffness for offshore wind turbines based on in situ seismic measurements. In *Journal of Physics: Conference Series*, volume 524, page 012088. IOP Publishing, 2014.

WWEA. 2014 half year report. Technical report, World Wind Energy Association, 2014.

Appendices

Appendix A

Model Structure Parameters

The model parameters for the structure used in this thesis was provided by post doc. Lene Eliassen, lene.eliassen@ntnu.no. The model assumes constant properties for the monopile section, while foundation and tower section has varying properties. The model is assuming a steel density of $\rho_s = 7780$ $[kg/m^3]$ and young's modulus $E = 10^9$ [GPa] The original data provided below is interpolated when the number of elements in the model is changed

Monopile

fractional length [-]	mass [kg/m]	moment of inertia [m^4]	element length [m]
0,00	24116	3,04E+01	2
0,03	24116	3,04E+01	2
0,06	24116	3,04E+01	2
0,09	24116	3,04E+01	2
0,12	24116	3,04E+01	2
0,15	24116	3,04E+01	2
0,18	24116	3,04E+01	2
0,21	24116	3,04E+01	2
0,24	24116	3,04E+01	2
0,26	24116	3,04E+01	2
0,29	24116	3,04E+01	2
0,32	24116	3,04E+01	2
0,35	24116	3,04E+01	2
0,38	24116	3,04E+01	2
0,41	24116	3,04E+01	2
0,44	24116	3,04E+01	2
0,47	24116	3,04E+01	2
0,50	24116	3,04E+01	1
0,53	24116	3,04E+01	1
0,56	24116	3,04E+01	1
0,59	24116	3,04E+01	1
0,62	24116	3,04E+01	1
0,65	24116	3,04E+01	1
0,68	24116	3,04E+01	1
0,71	24116	3,04E+01	1
0,74	24116	3,04E+01	1
0,76	24116	3,04E+01	1
0,79	24116	3,04E+01	1
0,82	24116	3,04E+01	1
0,85	24116	3,04E+01	1
0,88	24116	3,04E+01	1
0,91	24116	3,04E+01	1
0,94	24116	3,04E+01	1
0,97	24116	3,04E+01	1
1,00	24116	3,04E+01	1

Foundation

fractional length [-]	mass [kg/m]	moment of inertia [m^4]	element length [m]
0,00	34743	3,10E+01	0,5
0,06	34605	3,14E+01	0,5
0,11	34467	3,16E+01	0,5
0,17	34329	3,13E+01	0,5
0,22	34191	3,11E+01	0,5

0,28	34053	3,08E+01	0,5
0,33	33914	2,99E+01	0,5
0,39	33776	2,94E+01	0,5
0,44	33638	2,89E+01	0,5
0,50	33500	2,85E+01	0,5
0,56	33362	2,80E+01	0,5
0,61	33224	2,75E+01	0,5
0,67	33086	2,71E+01	0,5
0,72	32948	2,66E+01	0,5
0,78	32810	2,61E+01	0,5
0,83	32672	2,57E+01	0,5
0,89	32533	2,52E+01	0,5
0,94	32395	2,48E+01	0,5
1,00	25000	2,43E+01	0,5

Tower

fractional length [-]	kg/m	moment of inertia [m^4]	element length [m]
0,00	14207	24,00	11,5
0,11	12791	2,34E+01	11,5
0,22	11439	2,38E+01	11,5
0,33	10153	2,37E+01	11,5
0,44	8931	2,36E+01	11,5
0,56	7775	2,35E+01	11,5
0,67	6684	2,34E+01	11,5
0,78	5658	2,34E+01	11,5
0,89	4698	2,34E+01	11,5
1,00	3802	2,34E+01	11,5

Appendix B

Soil Data

The soil data used in the determination of the $p-y$ curves are given below. The provided table is given as force per meter length per meter displacement $[N/m \cdot m]$ for each of the 26 given soil levels. The data was provided by post doc. Lene Eliassen, lene.eliassen@ntnu.no. The original data provided below is interpolated when the number of elements in the model is changed

P-Y CURVE DATA

Soil Level #	1	2	3	4	5	6	7	8	9	10	11	12	13	14	15
Displacement [m]															
0	0,00E+00	0,00E+00	0,00E+00	0,00E+00	0,00E+00	0,00E+00	0,00E+00	0,00E+00	0,00E+00	0,00E+00	0,00E+00	0,00E+00	0,00E+00	0,00E+00	0,00E+00
0,005	5,83E+05	9,41E+04	1,07E+05	1,20E+05	1,34E+05	1,40E+05	1,46E+05	1,52E+05	1,58E+05	1,64E+05	1,86E+05	2,21E+05	2,46E+05	2,72E+05	2,98E+05
0,01	1,07E+06	1,88E+05	2,14E+05	2,41E+05	2,68E+05	2,80E+05	2,92E+05	3,04E+05	3,16E+05	3,28E+05	3,72E+05	4,43E+05	4,93E+05	5,44E+05	5,96E+05
0,015	1,41E+06	2,82E+05	3,21E+05	3,61E+05	4,01E+05	4,20E+05	4,38E+05	4,56E+05	4,74E+05	4,92E+05	5,58E+05	6,64E+05	7,39E+05	8,16E+05	8,95E+05
0,02	1,62E+06	3,77E+05	4,28E+05	4,81E+05	5,35E+05	5,59E+05	5,84E+05	6,08E+05	6,32E+05	6,56E+05	7,44E+05	8,86E+05	9,86E+05	1,09E+06	1,19E+06
0,025	1,74E+06	4,34E+05	4,94E+05	5,54E+05	6,17E+05	6,44E+05	6,72E+05	7,00E+05	7,28E+05	7,56E+05	8,57E+05	1,02E+06	1,14E+06	1,25E+06	1,37E+06
0,03	1,81E+06	4,54E+05	5,17E+05	5,81E+05	6,46E+05	6,75E+05	7,04E+05	7,33E+05	7,63E+05	7,92E+05	8,98E+05	1,07E+06	1,19E+06	1,31E+06	1,44E+06
0,035	1,85E+06	4,75E+05	5,40E+05	6,07E+05	6,75E+05	7,05E+05	7,36E+05	7,66E+05	7,97E+05	8,27E+05	9,38E+05	1,12E+06	1,24E+06	1,37E+06	1,50E+06
0,04	1,87E+06	4,95E+05	5,63E+05	6,33E+05	7,04E+05	7,36E+05	7,68E+05	7,99E+05	8,31E+05	8,63E+05	9,79E+05	1,17E+06	1,30E+06	1,43E+06	1,57E+06
0,045	1,88E+06	5,16E+05	5,87E+05	6,59E+05	7,33E+05	7,66E+05	7,99E+05	8,32E+05	8,66E+05	8,99E+05	1,02E+06	1,21E+06	1,35E+06	1,49E+06	1,63E+06
0,05	1,89E+06	5,36E+05	6,10E+05	6,85E+05	7,62E+05	7,96E+05	8,31E+05	8,65E+05	9,00E+05	9,34E+05	1,06E+06	1,26E+06	1,40E+06	1,55E+06	1,70E+06
0,055	1,89E+06	5,57E+05	6,33E+05	7,11E+05	7,91E+05	8,27E+05	8,63E+05	8,99E+05	9,34E+05	9,70E+05	1,10E+06	1,31E+06	1,46E+06	1,61E+06	1,76E+06
0,06	1,89E+06	5,77E+05	6,57E+05	7,38E+05	8,20E+05	8,57E+05	8,94E+05	9,32E+05	9,69E+05	1,01E+06	1,14E+06	1,36E+06	1,51E+06	1,67E+06	1,83E+06
0,065	1,90E+06	5,98E+05	6,80E+05	7,64E+05	8,49E+05	8,88E+05	9,26E+05	9,65E+05	1,00E+06	1,04E+06	1,18E+06	1,41E+06	1,56E+06	1,73E+06	1,89E+06
0,07	1,90E+06	6,13E+05	6,97E+05	7,83E+05	8,71E+05	9,10E+05	9,50E+05	9,89E+05	1,03E+06	1,07E+06	1,21E+06	1,44E+06	1,60E+06	1,77E+06	1,94E+06
0,075	1,90E+06	6,23E+05	7,08E+05	7,96E+05	8,85E+05	9,25E+05	9,65E+05	1,01E+06	1,05E+06	1,09E+06	1,23E+06	1,46E+06	1,63E+06	1,80E+06	1,97E+06
0,08	1,90E+06	6,33E+05	7,20E+05	8,09E+05	8,99E+05	9,40E+05	9,80E+05	1,02E+06	1,06E+06	1,10E+06	1,25E+06	1,49E+06	1,66E+06	1,83E+06	2,00E+06
0,085	1,90E+06	6,43E+05	7,31E+05	8,21E+05	9,13E+05	9,55E+05	9,96E+05	1,04E+06	1,08E+06	1,12E+06	1,27E+06	1,51E+06	1,68E+06	1,86E+06	2,04E+06
0,09	1,90E+06	6,53E+05	7,42E+05	8,34E+05	9,27E+05	9,69E+05	1,01E+06	1,05E+06	1,10E+06	1,14E+06	1,29E+06	1,54E+06	1,71E+06	1,89E+06	2,07E+06
0,095	1,90E+06	6,63E+05	7,54E+05	8,47E+05	9,41E+05	9,84E+05	1,03E+06	1,07E+06	1,11E+06	1,15E+06	1,31E+06	1,56E+06	1,73E+06	1,91E+06	2,10E+06
0,1	1,90E+06	6,72E+05	7,65E+05	8,59E+05	9,56E+05	9,99E+05	1,04E+06	1,09E+06	1,13E+06	1,17E+06	1,33E+06	1,58E+06	1,76E+06	1,94E+06	2,13E+06
0,105	1,90E+06	6,82E+05	7,76E+05	8,72E+05	9,70E+05	1,01E+06	1,06E+06	1,10E+06	1,15E+06	1,19E+06	1,35E+06	1,61E+06	1,79E+06	1,97E+06	2,16E+06
0,11	1,90E+06	6,92E+05	7,88E+05	8,85E+05	9,84E+05	1,03E+06	1,07E+06	1,12E+06	1,16E+06	1,21E+06	1,37E+06	1,63E+06	1,81E+06	2,00E+06	2,19E+06
0,115	1,90E+06	7,02E+05	7,99E+05	8,98E+05	9,98E+05	1,04E+06	1,09E+06	1,13E+06	1,18E+06	1,22E+06	1,39E+06	1,65E+06	1,84E+06	2,03E+06	2,22E+06
0,12	1,90E+06	7,12E+05	8,10E+05	9,10E+05	1,01E+06	1,06E+06	1,10E+06	1,15E+06	1,20E+06	1,24E+06	1,41E+06	1,68E+06	1,86E+06	2,06E+06	2,26E+06
0,125	1,90E+06	7,22E+05	8,22E+05	9,23E+05	1,03E+06	1,07E+06	1,12E+06	1,17E+06	1,21E+06	1,26E+06	1,43E+06	1,70E+06	1,89E+06	2,09E+06	2,29E+06
0,13	1,90E+06	7,32E+05	8,33E+05	9,36E+05	1,04E+06	1,09E+06	1,13E+06	1,18E+06	1,23E+06	1,28E+06	1,45E+06	1,72E+06	1,92E+06	2,12E+06	2,32E+06
0,135	1,90E+06	7,42E+05	8,44E+05	9,48E+05	1,05E+06	1,10E+06	1,15E+06	1,20E+06	1,25E+06	1,29E+06	1,47E+06	1,75E+06	1,94E+06	2,14E+06	2,35E+06
0,14	1,90E+06	7,52E+05	8,55E+05	9,61E+05	1,07E+06	1,12E+06	1,17E+06	1,21E+06	1,26E+06	1,31E+06	1,49E+06	1,77E+06	1,97E+06	2,17E+06	2,38E+06
0,145	1,90E+06	7,62E+05	8,67E+05	9,74E+05	1,08E+06	1,13E+06	1,18E+06	1,23E+06	1,28E+06	1,33E+06	1,51E+06	1,79E+06	1,99E+06	2,20E+06	2,41E+06
0,15	1,90E+06	7,72E+05	8,78E+05	9,86E+05	1,10E+06	1,15E+06	1,20E+06	1,25E+06	1,30E+06	1,35E+06	1,53E+06	1,82E+06	2,02E+06	2,23E+06	2,44E+06
0,155	1,90E+06	7,82E+05	8,89E+05	9,99E+05	1,11E+06	1,16E+06	1,21E+06	1,26E+06	1,31E+06	1,36E+06	1,54E+06	1,84E+06	2,05E+06	2,26E+06	2,48E+06
0,16	1,90E+06	7,92E+05	9,01E+05	1,01E+06	1,13E+06	1,18E+06	1,23E+06	1,28E+06	1,33E+06	1,38E+06	1,56E+06	1,86E+06	2,07E+06	2,29E+06	2,51E+06
0,165	1,90E+06	8,02E+05	9,12E+05	1,02E+06	1,14E+06	1,19E+06	1,24E+06	1,29E+06	1,35E+06	1,40E+06	1,58E+06	1,89E+06	2,10E+06	2,32E+06	2,54E+06
0,17	1,90E+06	8,12E+05	9,23E+05	1,04E+06	1,15E+06	1,21E+06	1,26E+06	1,31E+06	1,36E+06	1,41E+06	1,60E+06	1,91E+06	2,12E+06	2,35E+06	2,57E+06
0,175	1,90E+06	8,22E+05	9,35E+05	1,05E+06	1,17E+06	1,22E+06	1,27E+06	1,33E+06	1,38E+06	1,43E+06	1,62E+06	1,93E+06	2,15E+06	2,37E+06	2,60E+06
0,18	1,90E+06	8,32E+05	9,46E+05	1,06E+06	1,18E+06	1,24E+06	1,29E+06	1,34E+06	1,40E+06	1,45E+06	1,64E+06	1,96E+06	2,18E+06	2,40E+06	2,63E+06
0,185	1,90E+06	8,41E+05	9,57E+05	1,08E+06	1,20E+06	1,25E+06	1,30E+06	1,36E+06	1,41E+06	1,47E+06	1,66E+06	1,98E+06	2,20E+06	2,43E+06	2,67E+06
0,19	1,90E+06	8,51E+05	9,69E+05	1,09E+06	1,21E+06	1,26E+06	1,32E+06	1,37E+06	1,43E+06	1,48E+06	1,68E+06	2,00E+06	2,23E+06	2,46E+06	2,70E+06
0,195	1,90E+06	8,61E+05	9,80E+05	1,10E+06	1,22E+06	1,28E+06	1,33E+06	1,39E+06	1,45E+06	1,50E+06	1,70E+06	2,03E+06	2,25E+06	2,49E+06	2,73E+06
0,2	1,90E+06	8,71E+05	9,91E+05	1,11E+06	1,24E+06	1,29E+06	1,35E+06	1,41E+06	1,46E+06	1,52E+06	1,72E+06	2,05E+06	2,28E+06	2,52E+06	2,76E+06
0,205		8,81E+05	1,00E+06	1,13E+06	1,25E+06	1,31E+06	1,37E+06	1,42E+06	1,48E+06	1,54E+06	1,74E+06	2,07E+06	2,31E+06	2,55E+06	2,79E+06
0,21		8,91E+05	1,01E+06	1,14E+06	1,27E+06	1,32E+06	1,38E+06	1,44E+06	1,50E+06	1,55E+06	1,76E+06	2,10E+06	2,33E+06	2,57E+06	2,82E+06
0,215		9,01E+05	1,03E+06	1,15E+06	1,28E+06	1,34E+06	1,40E+06	1,45E+06	1,51E+06	1,57E+06	1,78E+06	2,12E+06	2,36E+06	2,60E+06	2,85E+06
0,22		9,11E+05	1,04E+06	1,16E+06	1,29E+06	1,35E+06	1,41E+06	1,47E+06	1,53E+06	1,59E+06	1,80E+06	2,14E+06	2,38E+06	2,63E+06	2,89E+06
0,225		9,21E+05	1,05E+06	1,18E+06	1,31E+06	1,37E+06	1,43E+06	1,49E+06	1,55E+06	1,61E+06	1,82E+06	2,17E+06	2,41E+06	2,66E+06	2,92E+06
0,23		9,26E+05	1,05E+06	1,18E+06	1,32E+06	1,37E+06	1,43E+06	1,49E+06	1,55E+06	1,61E+06	1,83E+06	2,18E+06	2,42E+06	2,67E+06	2,93E+06
0,235		9,30E+05	1,06E+06	1,19E+06	1,32E+06	1,38E+06	1,44E+06	1,50E+06	1,56E+06	1,62E+06	1,84E+06	2,19E+06	2,43E+06	2,69E+06	2,95E+06
0,24		9,35E+05	1,06E+06	1,19E+06	1,33E+06	1,39E+06	1,45E+06	1,51E+06	1,57E+06	1,63E+06	1,85E+06	2,20E+06	2,45E+06	2,70E+06	2,96E+06
0,245		9,39E+05	1,07E+06	1,20E+06	1,33E+06	1,39E+06	1,46E+06	1,52E+06	1,58E+06	1,64E+06	1,86E+06	2,21E+06	2,46E+06	2,71E+06	2,97E+06
0,25		9,44E+05	1,07E+06	1,21E+06	1,34E+06	1,40E+06	1,46E+06	1,52E+06	1,58E+06	1,64E+06	1,86E+06	2,22E+06	2,47E+06	2,73E+06	2,99E+06
0,255		9,48E+05	1,08E+06	1,21E+06	1,35E+06	1,41E+06	1,47E+06	1,53E+06	1,59E+06	1,65E+06	1,87E+06	2,23E+06	2,48E+06	2,74E+06	3,00E+06
0,26		9,53E+05	1,08E+06	1,22E+06	1,35E+06	1,41E+06	1,48E+06	1,54E+06	1,60E+06	1,66E+06	1,88E+06	2,24E+06	2,49E+06	2,75E+06	3,02E+06
0,265		9,57E+05	1,09E+06	1,22E+06	1,36E+06	1,42E+06	1,48E+06	1,54E+06	1,61E+06	1,67E+06	1,89E+06	2,25E+06	2,51E+06	2,77E+06	3,03E+06
0,27		9,62E+05	1,09E+06	1,23E+06	1,37E+06	1,43E+06	1,49E+06	1,55E+06	1,61E+06	1,68E+06	1,90E+06	2,26E+06	2,52E+06	2,78E+06	3,05E+06
0,275		9,66E+05	1,10E+06	1,23E+06	1,37E+06	1,43E+06	1,50E+06	1,56E+06	1,62E+06	1,68E+06	1,91E+06	2,27E+06	2,53E+06	2,79E+06	3,06E+06
0,28		9,71E+05	1,10E+06	1,24E+06	1,38E+06	1,44E+06	1,50E+06	1,57E+06	1,63E+06	1,69E+06	1,92E+06	2,28E+06	2,54E+06	2,80E+06	3,07E+06
0,285		9,75E+05	1,11E+06	1,25E+06	1,39E+06	1,45E+06	1,51E+06	1,57E+06	1,64E+06	1,70E+06	1,93E+06	2,29E+06	2,55E+06	2,82E+06	3,09E+06
0,29		9,80E+05	1,11E+06	1,25E+06	1,39E+06	1,45E+06	1,52E+06	1,58E+06	1,64E+06	1,71E+06	1,94E+06	2,30E+06	2,56E+06	2,83E+06	3,10E+06
0,295		9,84E+05	1,12E+06	1,26E+06	1,40E+06	1,46E+06	1,52E+06	1,59E+06	1,65E+06	1,71E+06	1,94E+06	2,31E+06	2,58E+06	2,84E+06	3,12E+06
0,3		9,89E+05	1,12E+06	1,26E+06	1,40E+06	1,47E+06	1,53E+06	1,60E+06	1,66E+06	1,72E+06	1,95E+06	2,33E+06	2,59E+06	2,86E+06	3,13E+06
0,305		9,93E+05	1,13E+06	1,27E+06	1,41E+06	1,48E+06	1,54E+06	1,60E+06	1,67E+06	1,73E+06	1,96E+06	2,34E+06	2,60E+06	2,87E+06	3,15E+06
0,31		9,98E+05	1,13E+06	1,27E+06	1,42E+06	1,48E+06	1,55E+06	1,61E+06	1,67E+06	1,74E+06	1,97E+06	2,35E+06	2,61E+06	2,88E+06	3,16E+06
0,315		1,00E+06	1,14E+06	1,28E+06	1,42E+06	1,49E+06	1,55E+06	1,62E+06	1,68E+06	1,75E+06	1,98E+06	2,36E+06	2,62E+06	2,90E+06	3,17E+06
0,32		1,01E+06	1,15E+06	1,29E+06	1,43E+06	1,50E+06	1,56E+06	1,62E+06	1,69E+06	1,75E+06	1,99E+06	2,37E+06	2,63E+06	2,91E+06	3,19E+06
0,325		1,01E+06	1,15E+06	1,29E+06	1,44E+06	1,50E+06	1,57E+06	1,63E+06	1,70E+06	1,76E+06	2,00E+06	2,38E+06	2,65E+06	2,92E+06	3,20E+06
0,33		1,02E+06	1,16E+06	1,30E+06	1,44E+06	1,51E+06	1,57E+06	1,64E+06	1,70E+06	1,77E+06	2,01E+06	2,39E+06	2,66E+06	2,93E+06	3,22E+06
0,335		1,02E+06	1,16E+06	1,30E+06	1,45E+06	1,52E+06	1,58E+06	1,65E+06	1,71E+06	1,78E+06	2,02E+06	2,40E+06	2,67E+06	2,95E+06	3,23E+06
0,34		1,02E+06	1,17E+06	1,31E+06	1,46E+06	1,52E+06	1,59E+06	1,65E+06	1,72E+06	1,79E+06	2,02E+06	2,41E+06	2,68E+06	2,96E+06	3,25E+06
0,345		1,03E+06	1,17E+06	1,32E+06	1,46E+06	1,53E+06	1,59E+06	1,66E+06	1,73E+06	1,79E+06	2,03E+06	2,42E+06	2,69E+06	2,97E+06	3,26E+06
0,35		1,03E+06	1,18E+06	1,32E+06	1,47E+06	1,54E+06	1,60E+06	1,67E+06	1,73E+06	1,80E+06	2,04E+06	2,43E+06	2,71E+06	2,99E+06	3,27E+06
0,355		1,04E+06	1,18E+06	1,33E+06	1,48E+06	1,54E+06	1,61E+06	1,68E+06	1,74E+06	1,81E+06	2,05E+06	2,44E+06	2,72E+06	3,00E+06	3,29E+06
0,36		1,04E+06	1,19E+06	1,33E+06	1,48E+06	1,55E+06	1,62E+06	1,68E+06	1,75E+06	1,82E+06	2,06E+06	2,45E+06	2,73E+06	3,01E+06	3,30E+06
0,365		1,05E+06	1,19E+06	1,34E+06	1,49E+06	1,56E+06	1,62E+06	1,69E+06	1,76E+06	1,82E+06	2,07E+06	2,46E+06	2,74E+06	3,03E+06	3,32E+06
0,37		1,05E+06	1,20E+06	1,34E+06	1,49E+06	1,56E+06	1,63E+06	1,70E+06	1,76E+06	1,83E+06	2,08E+06	2,47E+06	2,75E+06	3,04E+06	3,33E+06
0,375		1,06E+06	1,20E+06	1,35E+06	1,50E+06	1,57E+06	1,64E+06	1,70E+06	1,77E+06	1,84E+06	2,09E+06	2,48E+06	2,76E+06	3,05E+06	3,34E+06
0,38		1,06E+06	1,21E+06	1,36E+06	1,51E+06	1,58E+06	1,64E+06	1,71E+06	1,78E+06	1,85E+06	2,10E+06	2,49E+06	2,78E+06	3,06E+06	3,36E+06
0,385		1,07E+06	1,21E+06	1,36E+06	1,51E+06	1,58E+06	1,65E+06	1,72E+06	1,79E+06	1,86E+06	2,10E+06	2,51E+06	2,79E+06	3,08E+06	3,37E+06
0,39		1,07E+06	1,22E+06	1,37E+06	1,52E+06	1,59E+06	1,66E+06	1,73E+06	1,80E+06	1,86E+06	2,11E+06	2,52E+06	2,80E+06	3,09E+06	3,39E+06
0,395		1,07E+06	1,22E+06	1,37E+06	1,53E+06	1,60E+06	1,66E+06	1,73E+06	1,80E+06	1,87E+06	2,12E+06	2,53E+06	2,81E+06	3,10E+06	3,40E+06
0,4		1,08E+06	1,23E+06	1,38E+06	1,53E+06	1,60E+06	1,67E+06	1,74E+06	1,81E+06	1,88E+06	2,13E+06	2,54E+06	2,82E+06	3,12E+06	3,42E+06
0,405		1,08E+06	1,23E+06	1,38E+06	1,54E+06	1,61E+06	1,68E+06	1,75E+06	1,82E+06	1,89E+06	2,14E+06	2,55E+06	2,84E+06	3,13E+06	3,43E+06
0,41		1,09E+06	1,24E+06	1,39E+06	1,55E+06	1,62E+06	1,69E+06	1,76E+06	1,83E+06	1,90E+06	2,15E+06	2,56E+06	2,85E+06	3,14E+06	3,44E+06
0,415		1,09E+06	1,24E+06	1,40E+06	1,55E+06	1,62E+06	1,69E+06	1,76E+06	1,83E+06	1,90E+06	2,16E+06	2,57E+06	2,86E+06	3,16E+06	3,46E+06
0,42		1,10E+06	1,25E+06	1,40E+06	1,56E+06	1,63E+06	1,70E+06	1,77E+06	1,84E+06	1,91E+06	2,17E+06	2,58E+06	2,87E+06	3,17E+06	3,47E+06
0,425		1,10E+06	1,25E+06	1,41E+06	1,56E+06	1,64E+06	1,71E+06	1,78E+06	1,85E+06	1,92E+06	2,18E+06	2,59E+06	2,88E+06	3,18E+06	3,49E+06
0,43		1,11E+06	1,26E+06	1,41E+06	1,57E+06	1,64E+06	1,71E+06	1,78E+06	1,86E+06	1,93E+06	2,18E+06	2,60E+06	2,89E+06	3,19E+06	3,50E+06
0,435		1,11E+06	1,26E+06	1,42E+06	1,58E+06	1,65E+06	1,72E+06	1,79E+06	1,86E+06	1,93E+06	2,19E+06	2,61E+06	2,91E+06	3,21E+06	3,52E+06
0,44		1,11E+06	1,27E+06	1,42E+06	1,58E+06	1,66E+06	1,73E+06	1,80E+06	1,87E+06	1,94E+06	2,20E+06	2,62E+06	2,92E+06	3,22E+06	3,53E+06
0,445		1,12E+06	1,27E+06	1,43E+06	1,59E+06	1,66E+06	1,73E+06	1,81E+06	1,88E+06	1,95E+06	2,21E+06	2,63E+06	2,93E+06	3,23E+06	3,54E+06
0,45		1,12E+06	1,28E+06	1,44E+06	1,60E+06	1,67E+06	1,74E+06	1,81E+06	1,89E+06	1,96E+06	2,22E+06	2,64E+06	2,94E+06	3,25E+06	3,56E+06
0,455		1,13E+06	1,28E+06	1,44E+06	1,60E+06	1,68E+06	1,75E+06	1,82E+06	1,89E+06	1,97E+06	2,23E+06	2,65E+06	2,95E+06	3,26E+06	3,57E+06
0,46		1,13E+06	1,29E+06	1,45E+06	1,61E+06	1,68E+06	1,76E+06	1,83E+06	1,90E+06	1,97E+06	2,24E+06	2,66E+06	2,96E+06	3,27E+06	3,59E+06
0,465		1,14E+06	1,29E+06	1,45E+06	1,62E+06	1,69E+06	1,76E+06	1,84E+06	1,91E+06	1,98E+06	2,25E+06	2,67E+06	2,98E+06	3,29E+06	3,60E+06
0,47		1,14E+06	1,30E+06	1,46E+06	1,62E+06	1,70E+06	1,77E+06	1,84E+06	1,92E+06	1,99E+06	2,26E+06	2,69E+06	2,99E+06	3,30E+06	3,62E+06
0,475		1,15E+06	1,30E+06	1,46E+06	1,63E+06	1,70E+06	1,78E+06	1,85E+06	1,92E+06	2,00E+06	2,26E+06	2,70E+06	3,00E+06	3,31E+06	3,63E+06
0,48		1,15E+06	1,31E+06	1,47E+06	1,64E+06	1,71E+06	1,78E+06	1,86E+06	1,93E+06	2,01E+06	2,27E+06	2,71E+06	3,01E+06	3,32E+06	3,64E+06
0,485		1,16E+06	1,31E+06	1,48E+06	1,64E+06	1,72E+06	1,79E+06	1,86E+06	1,94E+06	2,01E+06	2,28E+06	2,72E+06	3,02E+06	3,34E+06	3,66E+06
0,49		1,16E+06	1,32E+06	1,48E+06	1,65E+06	1,72E+06	1,80E+06	1,87E+06	1,95E+06	2,02E+06	2,29E+06	2,73E+06	3,04E+06	3,35E+06	3,67E+06
0,495		1,16E+06	1,32E+06	1,49E+06	1,65E+06	1,73E+06	1,80E+06	1,88E+06	1,95E+06	2,03E+06	2,30E+06	2,74E+06	3,05E+06	3,36E+06	3,69E+06
0,5		1,17E+06	1,33E+06	1,49E+06	1,66E+06	1,74E+06	1,81E+06	1,89E+06	1,96E+06	2,04E+06	2,31E+06	2,75E+06	3,06E+06	3,38E+06	3,70E+06

16	17	18	19	20	21	22	23	24	25	26
0,00E+00	0,00E+00	0,00E+00	0,00E+00	0,00E+00	0,00E+00	0,00E+00	0,00E+00	0,00E+00	0,00E+00	0,00E+00
3,25E+05	3,47E+05	3,69E+05	3,92E+05	4,15E+05	4,49E+05	4,79E+05	5,26E+05	5,33E+05	5,55E+05	5,75E+05
6,50E+05	6,94E+05	7,39E+05	7,84E+05	8,30E+05	8,98E+05	9,58E+05	1,05E+06	1,07E+06	1,11E+06	1,15E+06
9,75E+05	1,04E+06	1,11E+06	1,18E+06	1,25E+06	1,35E+06	1,44E+06	1,58E+06	1,60E+06	1,67E+06	1,72E+06
1,30E+06	1,39E+06	1,48E+06	1,57E+06	1,66E+06	1,80E+06	1,92E+06	2,10E+06	2,13E+06	2,22E+06	2,30E+06
1,50E+06	1,60E+06	1,70E+06	1,81E+06	1,91E+06	2,07E+06	2,21E+06	2,42E+06	2,46E+06	2,56E+06	2,65E+06
1,57E+06	1,67E+06	1,78E+06	1,89E+06	2,00E+06	2,17E+06	2,31E+06	2,54E+06	2,57E+06	2,68E+06	2,77E+06
1,64E+06	1,75E+06	1,86E+06	1,98E+06	2,09E+06	2,26E+06	2,42E+06	2,65E+06	2,69E+06	2,80E+06	2,90E+06
1,71E+06	1,83E+06	1,94E+06	2,06E+06	2,18E+06	2,36E+06	2,52E+06	2,77E+06	2,81E+06	2,92E+06	3,02E+06
1,78E+06	1,90E+06	2,02E+06	2,15E+06	2,27E+06	2,46E+06	2,62E+06	2,88E+06	2,92E+06	3,04E+06	3,15E+06
1,85E+06	1,98E+06	2,10E+06	2,23E+06	2,36E+06	2,56E+06	2,73E+06	3,00E+06	3,04E+06	3,16E+06	3,27E+06
1,92E+06	2,05E+06	2,18E+06	2,32E+06	2,45E+06	2,66E+06	2,83E+06	3,11E+06	3,15E+06	3,28E+06	3,40E+06
1,99E+06	2,13E+06	2,26E+06	2,40E+06	2,54E+06	2,75E+06	2,94E+06	3,23E+06	3,27E+06	3,40E+06	3,52E+06
2,06E+06	2,20E+06	2,34E+06	2,49E+06	2,63E+06	2,85E+06	3,04E+06	3,34E+06	3,39E+06	3,52E+06	3,65E+06
2,12E+06	2,26E+06	2,40E+06	2,55E+06	2,70E+06	2,92E+06	3,12E+06	3,42E+06	3,47E+06	3,61E+06	3,74E+06
2,15E+06	2,30E+06	2,44E+06	2,59E+06	2,75E+06	2,97E+06	3,17E+06	3,48E+06	3,53E+06	3,67E+06	3,80E+06
2,18E+06	2,33E+06	2,48E+06	2,63E+06	2,79E+06	3,02E+06	3,22E+06	3,54E+06	3,59E+06	3,73E+06	3,86E+06
2,22E+06	2,37E+06	2,52E+06	2,68E+06	2,83E+06	3,07E+06	3,27E+06	3,59E+06	3,64E+06	3,79E+06	3,92E+06
2,25E+06	2,41E+06	2,56E+06	2,72E+06	2,88E+06	3,11E+06	3,32E+06	3,65E+06	3,70E+06	3,85E+06	3,98E+06
2,29E+06	2,44E+06	2,60E+06	2,76E+06	2,92E+06	3,16E+06	3,37E+06	3,70E+06	3,75E+06	3,91E+06	4,05E+06
2,32E+06	2,48E+06	2,64E+06	2,80E+06	2,96E+06	3,21E+06	3,42E+06	3,76E+06	3,81E+06	3,97E+06	4,11E+06
2,36E+06	2,52E+06	2,68E+06	2,84E+06	3,01E+06	3,25E+06	3,47E+06	3,81E+06	3,87E+06	4,03E+06	4,17E+06
2,39E+06	2,55E+06	2,72E+06	2,88E+06	3,05E+06	3,30E+06	3,52E+06	3,87E+06	3,92E+06	4,08E+06	4,23E+06
2,42E+06	2,59E+06	2,76E+06	2,92E+06	3,10E+06	3,35E+06	3,57E+06	3,92E+06	3,98E+06	4,14E+06	4,29E+06
2,46E+06	2,63E+06	2,79E+06	2,97E+06	3,14E+06	3,40E+06	3,62E+06	3,98E+06	4,04E+06	4,20E+06	4,35E+06
2,49E+06	2,66E+06	2,83E+06	3,01E+06	3,18E+06	3,44E+06	3,67E+06	4,04E+06	4,09E+06	4,26E+06	4,41E+06
2,53E+06	2,70E+06	2,87E+06	3,05E+06	3,23E+06	3,49E+06	3,73E+06	4,09E+06	4,15E+06	4,32E+06	4,47E+06
2,56E+06	2,74E+06	2,91E+06	3,09E+06	3,27E+06	3,54E+06	3,78E+06	4,15E+06	4,20E+06	4,38E+06	4,53E+06
2,60E+06	2,77E+06	2,95E+06	3,13E+06	3,32E+06	3,59E+06	3,83E+06	4,20E+06	4,26E+06	4,44E+06	4,59E+06
2,63E+06	2,81E+06	2,99E+06	3,17E+06	3,36E+06	3,63E+06	3,88E+06	4,26E+06	4,32E+06	4,49E+06	4,65E+06
2,66E+06	2,84E+06	3,03E+06	3,21E+06	3,40E+06	3,68E+06	3,93E+06	4,31E+06	4,37E+06	4,55E+06	4,71E+06
2,70E+06	2,88E+06	3,07E+06	3,26E+06	3,45E+06	3,73E+06	3,98E+06	4,37E+06	4,43E+06	4,61E+06	4,77E+06
2,73E+06	2,92E+06	3,11E+06	3,30E+06	3,49E+06	3,78E+06	4,03E+06	4,42E+06	4,49E+06	4,67E+06	4,83E+06
2,77E+06	2,95E+06	3,15E+06	3,34E+06	3,53E+06	3,82E+06	4,08E+06	4,48E+06	4,54E+06	4,73E+06	4,90E+06
2,80E+06	2,99E+06	3,18E+06	3,38E+06	3,58E+06	3,87E+06	4,13E+06	4,54E+06	4,60E+06	4,79E+06	4,96E+06
2,84E+06	3,03E+06	3,22E+06	3,42E+06	3,62E+06	3,92E+06	4,18E+06	4,59E+06	4,66E+06	4,85E+06	5,02E+06
2,87E+06	3,06E+06	3,26E+06	3,46E+06	3,67E+06	3,97E+06	4,23E+06	4,65E+06	4,71E+06	4,90E+06	5,08E+06
2,90E+06	3,10E+06	3,30E+06	3,50E+06	3,71E+06	4,01E+06	4,28E+06	4,70E+06	4,77E+06	4,96E+06	5,14E+06
2,94E+06	3,14E+06	3,34E+06	3,55E+06	3,75E+06	4,06E+06	4,33E+06	4,76E+06	4,82E+06	5,02E+06	5,20E+06
2,97E+06	3,17E+06	3,38E+06	3,59E+06	3,80E+06	4,11E+06	4,38E+06	4,81E+06	4,88E+06	5,08E+06	5,26E+06
3,01E+06	3,21E+06	3,42E+06	3,63E+06	3,84E+06	4,16E+06	4,43E+06	4,87E+06	4,94E+06	5,14E+06	5,32E+06
3,04E+06	3,25E+06	3,46E+06	3,67E+06	3,88E+06	4,20E+06	4,48E+06	4,92E+06	4,99E+06	5,20E+06	5,38E+06
3,08E+06	3,28E+06	3,50E+06	3,71E+06	3,93E+06	4,25E+06	4,53E+06	4,98E+06	5,05E+06	5,26E+06	5,44E+06
3,11E+06	3,32E+06	3,54E+06	3,75E+06	3,97E+06	4,30E+06	4,59E+06	5,04E+06	5,11E+06	5,31E+06	5,50E+06
3,14E+06	3,36E+06	3,57E+06	3,79E+06	4,02E+06	4,35E+06	4,64E+06	5,09E+06	5,16E+06	5,37E+06	5,56E+06
3,18E+06	3,39E+06	3,61E+06	3,84E+06	4,06E+06	4,39E+06	4,69E+06	5,15E+06	5,22E+06	5,43E+06	5,62E+06
3,19E+06	3,41E+06	3,63E+06	3,85E+06	4,08E+06	4,41E+06	4,71E+06	5,17E+06	5,24E+06	5,46E+06	5,65E+06
3,21E+06	3,43E+06	3,65E+06	3,87E+06	4,10E+06	4,44E+06	4,73E+06	5,20E+06	5,27E+06	5,49E+06	5,68E+06
3,23E+06	3,44E+06	3,67E+06	3,89E+06	4,12E+06	4,46E+06	4,76E+06	5,22E+06	5,30E+06	5,51E+06	5,71E+06
3,24E+06	3,46E+06	3,68E+06	3,91E+06	4,14E+06	4,48E+06	4,78E+06	5,25E+06	5,32E+06	5,54E+06	5,73E+06
3,26E+06	3,48E+06	3,70E+06	3,93E+06	4,16E+06	4,50E+06	4,80E+06	5,27E+06	5,35E+06	5,57E+06	5,76E+06
3,27E+06	3,49E+06	3,72E+06	3,95E+06	4,18E+06	4,52E+06	4,82E+06	5,30E+06	5,37E+06	5,59E+06	5,79E+06
3,29E+06	3,51E+06	3,74E+06	3,97E+06	4,20E+06	4,54E+06	4,85E+06	5,32E+06	5,40E+06	5,62E+06	5,82E+06
3,30E+06	3,53E+06	3,75E+06	3,99E+06	4,22E+06	4,56E+06	4,87E+06	5,35E+06	5,42E+06	5,64E+06	5,84E+06
3,32E+06	3,54E+06	3,77E+06	4,00E+06	4,24E+06	4,59E+06	4,89E+06	5,37E+06	5,45E+06	5,67E+06	5,87E+06
3,33E+06	3,56E+06	3,79E+06	4,02E+06	4,26E+06	4,61E+06	4,92E+06	5,40E+06	5,47E+06	5,70E+06	5,90E+06
3,35E+06	3,58E+06	3,81E+06	4,04E+06	4,28E+06	4,63E+06	4,94E+06	5,42E+06	5,50E+06	5,72E+06	5,93E+06
3,37E+06	3,59E+06	3,83E+06	4,06E+06	4,30E+06	4,65E+06	4,96E+06	5,45E+06	5,53E+06	5,75E+06	5,95E+06
3,38E+06	3,61E+06	3,84E+06	4,08E+06	4,32E+06	4,67E+06	4,98E+06	5,47E+06	5,55E+06	5,78E+06	5,98E+06
3,40E+06	3,63E+06	3,86E+06	4,10E+06	4,34E+06	4,69E+06	5,01E+06	5,50E+06	5,58E+06	5,80E+06	6,01E+06
3,41E+06	3,64E+06	3,88E+06	4,12E+06	4,36E+06	4,71E+06	5,03E+06	5,52E+06	5,60E+06	5,83E+06	6,04E+06
3,43E+06	3,66E+06	3,90E+06	4,14E+06	4,38E+06	4,74E+06	5,05E+06	5,55E+06	5,63E+06	5,86E+06	6,06E+06
3,44E+06	3,68E+06	3,91E+06	4,15E+06	4,40E+06	4,76E+06	5,08E+06	5,57E+06	5,65E+06	5,88E+06	6,09E+06
3,46E+06	3,69E+06	3,93E+06	4,17E+06	4,42E+06	4,78E+06	5,10E+06	5,60E+06	5,68E+06	5,91E+06	6,12E+06
3,47E+06	3,71E+06	3,95E+06	4,19E+06	4,44E+06	4,80E+06	5,12E+06	5,63E+06	5,70E+06	5,94E+06	6,15E+06
3,49E+06	3,73E+06	3,97E+06	4,21E+06	4,46E+06	4,82E+06	5,14E+06	5,65E+06	5,73E+06	5,96E+06	6,17E+06
3,51E+06	3,74E+06	3,98E+06	4,23E+06	4,48E+06	4,84E+06	5,17E+06	5,68E+06	5,75E+06	5,99E+06	6,20E+06
3,52E+06	3,76E+06	4,00E+06	4,25E+06	4,50E+06	4,86E+06	5,19E+06	5,70E+06	5,78E+06	6,02E+06	6,23E+06
3,54E+06	3,78E+06	4,02E+06	4,27E+06	4,52E+06	4,89E+06	5,21E+06	5,73E+06	5,81E+06	6,04E+06	6,26E+06
3,55E+06	3,79E+06	4,04E+06	4,29E+06	4,54E+06	4,91E+06	5,24E+06	5,75E+06	5,83E+06	6,07E+06	6,28E+06
3,57E+06	3,81E+06	4,05E+06	4,30E+06	4,56E+06	4,93E+06	5,26E+06	5,78E+06	5,86E+06	6,10E+06	6,31E+06
3,58E+06	3,83E+06	4,07E+06	4,32E+06	4,58E+06	4,95E+06	5,28E+06	5,80E+06	5,88E+06	6,12E+06	6,34E+06
3,60E+06	3,84E+06	4,09E+06	4,34E+06	4,60E+06	4,97E+06	5,31E+06	5,83E+06	5,91E+06	6,15E+06	6,37E+06
3,61E+06	3,86E+06	4,11E+06	4,36E+06	4,62E+06	4,99E+06	5,33E+06	5,85E+06	5,93E+06	6,18E+06	6,39E+06
3,63E+06	3,88E+06	4,13E+06	4,38E+06	4,64E+06	5,02E+06	5,35E+06	5,88E+06	5,96E+06	6,20E+06	6,42E+06
3,65E+06	3,89E+06	4,14E+06	4,40E+06	4,66E+06	5,04E+06	5,37E+06	5,90E+06	5,98E+06	6,23E+06	6,45E+06
3,66E+06	3,91E+06	4,16E+06	4,42E+06	4,68E+06	5,06E+06	5,40E+06	5,93E+06	6,01E+06	6,26E+06	6,48E+06
3,68E+06	3,93E+06	4,18E+06	4,44E+06	4,70E+06	5,08E+06	5,42E+06	5,95E+06	6,04E+06	6,28E+06	6,50E+06
3,69E+06	3,94E+06	4,20E+06	4,45E+06	4,72E+06	5,10E+06	5,44E+06	5,98E+06	6,06E+06	6,31E+06	6,53E+06
3,71E+06	3,96E+06	4,21E+06	4,47E+06	4,74E+06	5,12E+06	5,47E+06	6,00E+06	6,09E+06	6,34E+06	6,56E+06
3,72E+06	3,98E+06	4,23E+06	4,49E+06	4,75E+06	5,14E+06	5,49E+06	6,03E+06	6,11E+06	6,36E+06	6,59E+06
3,74E+06	3,99E+06	4,25E+06	4,51E+06	4,77E+06	5,17E+06	5,51E+06	6,05E+06	6,14E+06	6,39E+06	6,61E+06
3,75E+06	4,01E+06	4,27E+06	4,53E+06	4,79E+06	5,19E+06	5,53E+06	6,08E+06	6,16E+06	6,41E+06	6,64E+06
3,77E+06	4,03E+06	4,28E+06	4,55E+06	4,81E+06	5,21E+06	5,56E+06	6,10E+06	6,19E+06	6,44E+06	6,67E+06
3,79E+06	4,04E+06	4,30E+06	4,57E+06	4,83E+06	5,23E+06	5,58E+06	6,13E+06	6,21E+06	6,47E+06	6,70E+06
3,80E+06	4,06E+06	4,32E+06	4,59E+06	4,85E+06	5,25E+06	5,60E+06	6,15E+06	6,24E+06	6,49E+06	6,72E+06
3,82E+06	4,07E+06	4,34E+06	4,60E+06	4,87E+06	5,27E+06	5,63E+06	6,18E+06	6,27E+06	6,52E+06	6,75E+06
3,83E+06	4,09E+06	4,36E+06	4,62E+06	4,89E+06	5,29E+06	5,65E+06	6,20E+06	6,29E+06	6,55E+06	6,78E+06
3,85E+06	4,11E+06	4,37E+06	4,64E+06	4,91E+06	5,32E+06	5,67E+06	6,23E+06	6,32E+06	6,57E+06	6,81E+06
3,86E+06	4,12E+06	4,39E+06	4,66E+06	4,93E+06	5,34E+06	5,69E+06	6,25E+06	6,34E+06	6,60E+06	6,83E+06
3,88E+06	4,14E+06	4,41E+06	4,68E+06	4,95E+06	5,36E+06	5,72E+06	6,28E+06	6,37E+06	6,63E+06	6,86E+06
3,89E+06	4,16E+06	4,43E+06	4,70E+06	4,97E+06	5,38E+06	5,74E+06	6,30E+06	6,39E+06	6,65E+06	6,89E+06
3,91E+06	4,17E+06	4,44E+06	4,72E+06	4,99E+06	5,40E+06	5,76E+06	6,33E+06	6,42E+06	6,68E+06	6,92E+06
3,92E+06	4,19E+06	4,46E+06	4,74E+06	5,01E+06	5,42E+06	5,79E+06	6,36E+06	6,44E+06	6,71E+06	6,94E+06
3,94E+06	4,21E+06	4,48E+06	4,75E+06	5,03E+06	5,44E+06	5,81E+06	6,38E+06	6,47E+06	6,73E+06	6,97E+06
3,96E+06	4,22E+06	4,50E+06	4,77E+06	5,05E+06	5,47E+06	5,83E+06	6,41E+06	6,49E+06	6,76E+06	7,00E+06
3,97E+06	4,24E+06	4,51E+06	4,79E+06	5,07E+06	5,49E+06	5,85E+06	6,43E+06	6,52E+06	6,79E+06	7,03E+06
3,99E+06	4,26E+06	4,53E+06	4,81E+06	5,09E+06	5,51E+06	5,88E+06	6,46E+06	6,55E+06	6,81E+06	7,05E+06
4,00E+06	4,27E+06	4,55E+06	4,83E+06	5,11E+06	5,53E+06	5,90E+06	6,48E+06	6,57E+06	6,84E+06	7,08E+06
4,02E+06	4,29E+06	4,57E+06	4,85E+06	5,13E+06	5,55E+06	5,92E+06	6,51E+06	6,60E+06	6,87E+06	7,11E+06
4,03E+06	4,31E+06	4,58E+06	4,87E+06	5,15E+06	5,57E+06	5,95E+06	6,53E+06	6,62E+06	6,89E+06	7,14E+06

Appendix C

Turbine Parameters

The following Table outlines general parameters for the 10 MW DTU reference turbine. The total report on the development of the turbine can be found in Bak et al. (2014).

Parameter	**DTU 10MW RWT**
Wind Regime	IEC Class 1A
Rotor Orientation	Clockwise rotation - Upwind
Control	Variable Speed Collective Pitch
Cut in wind speed	4 m/s
Cut out wind speed	25 m/s
Rated wind speed	11.4 m/s
Rated power	10 MW
Number of blades	3
Rotor Diameter	178.3 m
Hub Diameter	5.6 m
Hub Height	119.0 m
Drivetrain	Medium Speed, Multiple-Stage Gearbox
Minimum Rotor Speed	6.0 rpm
Maximum Rotor Speed	9.6 rpm
Maximum Generator Speed	480.0 rpm
Gearbox Ratio	50
Maximum Tip Speed	90.0 m/s
Hub Overhang	7.1 m
Shaft Tilt Angle	5.0 deg.
Rotor Precone Angle	-2.5 deg.
Blade Prebend	3.332 m
Rotor Mass	227,962 kg
Nacelle Mass	446,036 kg
Tower Mass	628,442 kg